Decoding of Facial Strains via Conformable Piezoelectric Interfaces and Three-Dimensional Digital Image Correlation

by

Farita Tasnim

B.Sc., Massachusetts Institute of Technology (2019)

Submitted to the Program in Media Arts and Sciences, School of Architecture and Planning, in partial fulfillment of the requirements for the degree of

Master of Science

at the
Massachusetts Institute of Technology
June 2021

Author
……
Program in Media Arts and Sciences
March 8, 2021

Certified by
……
Canan Dagdeviren
Assistant Professor of Media Arts and Sciences

Accepted by
……
Tod Machover
Academic Head, Program in Media Arts and Sciences

Decoding of Facial Strains via Conformable Piezoelectric Interfaces and Three-Dimensional Digital Image Correlation

by

Farita Tasnim

Submitted to the Program in Media Arts and Sciences, School of Architecture and Planning, on March 8, 2021 in partial fulfillment of the requirements for the degree of

Master of Science

Abstract

Devices that facilitate nonverbal communication typically require high computational loads or have rigid and bulky form factors that are unsuitable for use on the face or on other curvilinear body surfaces. This work reports the design and pilot testing of an integrated system for decoding facial strains and for predicting facial kinematics. The system consists of mass-manufacturable, conformable piezoelectric thin films for strain mapping; multiphysics modelling for analysing the nonlinear mechanical interactions between the conformable device and the epidermis; and three-dimensional digital image correlation (3D-DIC) for reconstructing soft-tissue surfaces under dynamic deformations as well as for informing device design and placement. Most biomedical sensor designs lack an in-depth study of the target soft tissue before the design and fabrication of the sensor meant to couple to that tissue. This work demonstrates the use of 3D-DIC as a method for in-depth biokinematic study of the target region upon which a sensor with mechanically-active functional material, such as piezoelectrics, will be placed. Similar to how chemical assays of a body part would be conducted before designing medication for disorders of that body part, so too does 3D-DIC allow for the mechanical study of biological soft tissue before designing the mechanically-active functional materials on mechanically-adaptive substrates that are meant to intimately integrate with that soft tissue. Thus, the 3D-DIC allowed for the design of a conformable piezoelectric device that mimics the properties of skin and that can interpret and distinguish facial strains in real-time and with low computational load, i.e. with reduced data streaming bandwidth. Finally, pilot studies on healthy individuals and on individuals with amyotrophic lateral sclerosis show that these conformable piezoelectric devices, coupled with algorithms for the real-time detection and classification of distinct skin-deformation signatures, enable the reliable decoding of facial movements. The integrated system could be adapted for use in clinical settings as a nonverbal communication technology or for use in the monitoring of neuromuscular conditions.

Thesis advisor:
Canan Dagdeviren
Assistant Professor of Media Arts and Sciences

Decoding of Facial Strains via Conformable Piezoelectric Interfaces and Three-Dimensional Digital Image Correlation

by

Farita Tasnim

This thesis has been reviewed and approved by the following committee members:

Canan Dagdeviren

……

Assistant Professor of Media Arts and Sciences
Massachusetts Institute of Technology

Polina Anikeeva

……

Associate Professor in Materials Science and Engineering
Associate Professor in Brain and Cognitive Sciences, McGovern Institute for Brain Research
Associate Director, Research Laboratory of Electronics
Massachusetts Institute of Technology

Joseph M. Jacobson

……

Associate Professor of Media Arts and Sciences
Massachusetts Institute of Technology

Acknowledgements

The results and writeup of this thesis have been previously published in a journal article co-first authored by myself and Dr. Tao Sun and jointly written with Rachel T. McIntosh, Nikta Amiri, Dana Solav, Mostafa Tavakkoli Anbarani, David Sadat, Lin Zhang, Yuandong Gu, M. Amin Karami, and Canan Dagdeviren. The article was published in Nature Biomedical Engineering on October 22, 2020, and can be accessed at the following DOI: https://doi.org/10.1038/s41551-020-00612-w . Firstly, I would like to thank my thesis advisor, Dr. Canan Dagdeviren, for her guidance and support throughout this project. I would also like to thank Dr. Tao Sun as my principal collaborator on the work presented in this thesis; he conducted the main sensor fabrication steps and ran the mechanical testing experiments. I also thank Rachel McIntosh and Dana Solav for their help in designing and constructing 3D-DIC setups, as well as processing the DIC data. I also thank Nikta Amiri, Mostafa T. Anbarani, and Dr. M. Amin Karami for their valuable help in analytical and finite element modeling of thin film piezoelectrics on soft substrates. I also thank David Sadat for his help in taking the photographs and constructing the movies for this work, as well as for leading the important next project of developing dynamic 3D-DIC setups that can track and follow natural human movements such as walking and running as I change fields entirely to the theoretical physics of living systems for my PhD.

I thank all the members of the microfabrication facility/cleanroom (YellowBox) and more broadly of the entire Conformable Decoders research group at the MIT Media Lab for helpful advice and discussions. Additionally, I'd like to thank Dr. Deb Roy and Doug Beeferman for initial discussions concerning kNN–DTW algorithms for classifying temporal waveforms. I also thank Keith Warren for discussions on sensor characterization, and Ron Wiken for discussions on the design and fabrication of 3D-DIC set-ups. I would also like to thank Dr. Yuangdong Gu and associated staff at the Institute of Microelectronics (IME), A*STAR, Singapore for collaboration on initial sensor fabrication and materials. I thank Dr. Robert Brown of the University of Massachusetts Medical School for helping to recruit the patients with ALS and for discussion on cFaCES application on the patients with ALS. I also thank the members of the Instron Laboratory of the Koch Institute For Integrative Cancer Research at MIT. This work was performed in part at the Center for Nanoscale Systems (CNS), a member of the National Nanotechnology Coordinated Infrastructure Network (NNCI), which was supported by the National Science Foundation under NSF award no. 1541959. CNS is part of Harvard University.

I sincerely thank our ALS friends, Phyl Gerber and Dennis Ceruti, who became an important part of our work and helped us tremendously with human trials; and their families for their generous help and profound dedication during the ALS patient trials. Unfortunately, Dennis and Phyl passed away in June of 2020, but their contribution to our work will always be remembered and they will be eternal in our scientific article.

Finally, I deeply thank my parents, Mallik Rafat Ahmed and Fatema Sultana, as well as my siblings, Noor Tanzeela Ahmed and Rafin Mallik Ahmed, for their constant love and support throughout my ventures, academic or otherwise.

Contents

Chapter 1: Background and Contributions

1.1 Introduction

Human skin allows for an abundance of fine muscular movements that form the ability to communicate in daily life, whether through shaping vocal sounds into recognizable speech or forming facial expressions for nonverbal communication [1–3]. Despite the importance of facial movements, much is still unknown about the quantifiable patterns of mechanical deformation that occur on the skin as a result of the contraction and relaxation of muscles. Precise measurements of soft tissue biokinematics, such as skin strain during facial deformations, can be used to computationally recognize distinct facial motions, and thus facilitate nonverbal communication for patients who lack the ability to speak or interact with traditional electronic communication interfaces.

Many neuromuscular disorders, such as amyotrophic lateral sclerosis (ALS), are caused by peripheral nerve degeneration, interruptions in the signaling and response pathways between motor neurons and muscles, and eventual muscular atrophy [4]. Although these diseases have low prevalence and incidence, they induce severe disability and high fatality rates, with 50% of ALS patients dying within 15–20 months after diagnosis [5]. Such disorders often manifest themselves through physiological changes in a person's hands, feet, and other body parts, including gradual loss of their ability to exercise fine motor skills and to vocalize intelligible speech [6]. As a result, patients with ALS or related disorders experience barriers to tasks requiring finger dexterity and sustained speech, but often retain the ability to form facial motions [7]. Predictable methods for continuous tracking of dynamic skin strain on the face, therefore, can enable new forms of communication for individuals with such disorders.

At present, methods for *in vivo* characterization of facial deformations often involve electromyography (EMG) [8,9] or camera tracking [10–17]. While these systems provide valuable insights into the characterization of facial motions, capturing such measurements typically result in cumbersome computational load or have rigid, bulky structures with highly visible interfaces to soft skin, presenting difficulty for continuous use in daily life, especially for individuals with neuromuscular disorders (Table S1). As such, present technologies are often unsuitable for continuous, portable monitoring or for use on highly curvilinear regions of the body, such as the face. An alternative strategy involves the use of thin film piezoelectric materials, such as lead zirconate titanate (PZT) [18–20], $BaTiO_3$ [21], and zinc oxide (ZnO) [22], or fiber forms of polyvinylidene fluoride (PVDF)'s copolymer with trifluoroethylene (PVDF-TrFE) [23,24], to convert changes in soft tissue strain to measurable changes in electrical voltage and current. Such piezoelectric thin film devices have been increasingly explored for biomedical sensors, transducers, and energy harvesters [25,26] because they can be tailored to offer (i) high dynamic sensitivity across a wide pressure regime (0~100kPa), (ii) simplicity in device structure, (iii) reliability, and (iv) stability under cyclic loading conditions [18,27,28]. A widely deployable system for real-time detection of facial motions, however, would further necessitate the use of low-cost materials, easily manufacturable processes, and a seamless pipeline for fabrication, testing, and validation.

This work introduces a set of materials, device designs, fabrication steps, theoretical calculations, simulations, and validation protocols that realize robust, mechanically-adaptive, predictable, and visually-invisible (Movie S1) *in vivo* monitoring of spatiotemporal epidermal strains and decoding of distinct facial deformation signatures through the use of conformable devices comprised of aluminum nitride (AlN) piezoelectric thin films on compliant polydimethylsiloxane (PDMS) substrates. The use of a substrate with an elastic modulus comparable to that of the human epidermis enables soft, reversible lamination of the conformable Facial Code Extrapolation Sensor (cFaCES) onto any area of skin, which permits

rapid, repeatable measurements of skin strain during facial motions, without causing any inflammation and/or allergic reactions while remaining stable across a range of temperatures and humidities on the human skin [18,29–32] (Fig. S1). Furthermore, a methodology is presented that enables voltage-strain correlation in mechanically adaptive, piezoelectric devices and informs their placement by quantitative study of dynamic soft tissue biokinematics using stereophotogrammetry (PG) and subsequent three-dimensional digital image correlation (3D-DIC). This methodology generates accurate, repeatable spatiotemporal maps of full-field facial skin strains and device-on-skin strains during facial movements. Comprehensive theoretical and *in vitro* experimental studies establish that these systems can provide accurate and reproducible measurements of strain during compression, stretching, and bending in quasi-static regimes. Similar characterization of the sensor on a mock skin suggest enhanced sensor sensitivity when coupled with soft, elastomeric targets. Preliminary *in vivo* experiments on healthy and ALS subjects coupled with further theoretical studies and 3D-DIC assessment demonstrate that the predictability, reproducibility, and sensitivity of skin strain measurements from a cFaCES allow for real-time decoding and classification of an individual's facial motions, potentially enabling an alternative method of nonverbal communication for individuals with neuromuscular disorders, such as ALS.

1.2 Sensor development

Figures 1a and 1b provide images and schematic diagrams of a cFaCES. Fabrication of the cFaCES (Fig. S2) followed by an electrical anodization process (Fig. S3) achieves the sensor's conformable structure, which yields seamless integration with facial skin (Fig. S4). The ultrathin architecture of the active piezoelectric elements, along with the serpentine metal electrodes that establish their electrical connections, result in low elastic modulus, conformable structures when supported by a thin elastomer (PDMS, 40 μm-thick) substrate. The lateral configuration of a cFaCES consists of an array of AlN thin films, which demonstrate anisotropic growth (0002) of

wurtzite crystal structure (Fig. S5), patterned in circular shapes, which allow for localized spatiotemporal measurements of strain without directional bias. The circular structures are capacitor-type elements, each of which incorporates a layer of AlN (1.5 μm-thick, 0.48 cm diameter) sandwiched between two Molybdenum (Mo) electrodes (200 nm) and encapsulated with a 1 μm-thick layer of silicon dioxide (SiO_2). cFaCES has a simplified structure, i.e. 2 x 2 spatial array of piezoelectric elements, to reduce the amount of data processing required during real-time decoding in an effort to push the boundary of the decoding accuracy with lower cost and lower computational load (Table S1). Further fabrication details can be found in the Methods section. Although any piezoelectric material could be incorporated in a cFaCES as the active layer without sacrifice of functionality, the specific use of AlN fabricated in an 8-inch wafer process results in a low cost ($10/cFaCES), disposable device (Fig. S6a). The sensor achieves a response time (5 ms) fast enough to track the changes in muscle motions, which occur on 10 ms timescales (Fig. S6b). Furthermore, the complementary metal–oxide–semiconductor (CMOS)-compatible nature [33–35] of the AlN piezoelectric layer can allow for mass manufacturability, while the lead-free property of the device materials can make the clinical transition much smoother, when compared to a device with lead-based piezoelectrics, such as PZT, especially in countries where lead-based devices are being actively phased out of production [36,37]. Due to the minimal thickness of all the component layers [38,39], the resulting device can be applied conformally and securely to the skin with the use of a thin 3M Tegaderm® medical tape (40 μm-thick) with an adhesion force of ~1.5N and adhesion strength of ~60 N/m (Fig. S6c) and is stable over a wide temperature range, 25 - 65°C (Fig. S6d). *In vitro* studies with human epidermal keratinocytes demonstrate device biocompatibility. Particularly, cell viability studies reveal no evidence of cell toxicity and the cell culturing process does not alter the surface properties of the sensor (Fig. S7).

1.3 Biokinematic assessment of dynamically deforming soft tissue

The key to achieving highly predictable operation of the aforementioned, localized sensor *in vivo* requires accurate voltage-strain correlation for any sensor placement location, and is realized by reliable, non-contact, full-field spatiotemporal measurements of surface strains with and without cFaCES laminated on the epidermal region of interest. Fig. 1c provides a schematic diagram of the custom-built system for PG and 3D-DIC for measurement of the full-field spatiotemporal facial skin strain. When an object, such as the human face, is positioned in view of a set of cameras — such that each pair of two adjacent cameras has an overlapping field-of-view (FOV) of the object — the cameras can reliably capture 12-bit resolution images of the object's movement at a rate of 6 frames per second (fps). If the object is speckled with a random pattern of dots (Fig. S8) and then undergoes deformation during this image capture, subsequent multi-camera 3D-DIC using MultiDIC [40,41] can accurately reconstruct the surface of the object in 3D space and track the strain field across that surface during movements. Sets of images collected from both a cylindrically-shaped calibration object and a flat checkerboard distortion correction object (Fig. S9) are utilized to derive the intrinsic and extrinsic camera parameters (i.e. focal lengths, principal point coordinates, radial and tangential distortion parameters, and skew parameters, position and orientation of the camera with respect to the global coordinate system) through both direct linear transformation (DLT) and bundle adjustment (BA) methods [40]. The determined DLT parameters and BA parameters are then used to map two-dimensional (2D) image points of the calibration object into 3D space and calculate the reconstruction errors, which result from a variety of sources, such as image quality, focus, and lighting. The presented setup consistently produces root mean-square (RMS) reconstruction errors of approximately 100 μm, which characterizes the calibration of the setup (Fig. S10, S11, Note S1a).

The 3D-DIC process includes analysis of pairwise images to detect matching image points and calculate their correlation coefficient, a parameter describing the degree of “matching” of the speckles on the object of interest as seen from two adjacent cameras (spatially) and as they move over time (temporally) (Note S1b). The calculation of correlation coefficients is the main result of 2D-DIC, and is computed using NCorr [42,43], whose methodology defines a correlation cost function for which a lower degree of matching equates to a higher correlation coefficient. After the correlation process, 3D reconstruction followed by strain calculation results in a spatiotemporal full-field measurement of strain across the surface of the object of interest. Each pair of cameras produces a triangular mesh created from the 3D point cloud resolved from 3D reconstruction of 2D image points (Note S1c). The full-field displacements, deformations, and strains are then calculated from the temporal changes in the 3D coordinates of the triangular mesh from each pair using a variation of the triangular Cosserat point element method (Note S1d) [40,44,45]. The eigendecomposition of the local Lagrangian strain tensor provides principal strain directions and magnitudes on each local surface element comprising the triangular mesh (Note S1d). Throughout this work, the convention is that the first principal strain is the minimal in-plane strain, the second principal strain is the maximal in-plane strain occurring in an orthogonal direction, and the third principal strain, or out-of-plane strain, is immeasurable. Strain data gathered during DIC trials show the in-plane strain occurring on the top surface of the object of study. Control null-strain tests, as shown in Fig. S12, give representative errors resulting from the DIC setup, data collection procedure, and effect of analyzing real human skin, and allow for reliable and theoretically-predictable results for tracking the strain of facial skin and of the sensor laminated on facial skin. Figure 1D depicts a representative spatial map of the strain field at the peak strain time point during a human subject’s right-cheek twitch motion. First (minimal) and second (maximal) principal surface strains are shown for a healthy subject performing the motion without (left) and with (right) a cFaCES laminated on the cheek. Together with cFaCES electrical measurement when laminated on different subjects and in various

locations of the face (Fig. 1e), 3D-DIC optical measurement of strain can be analyzed via theoretical modeling to achieve predictable and verifiable strain-to-voltage correlation for the cFaCES devices. The 3D-DIC methodology, which is only implemented once during an initial calibration period for a new user, allows for the conducting of complex pre-analysis of the human epidermis, which then can translate to smarter device design and informed location selection for device placement on the skin so as to maximize decodability from minimal sensing elements and data processing (Fig. S1f).

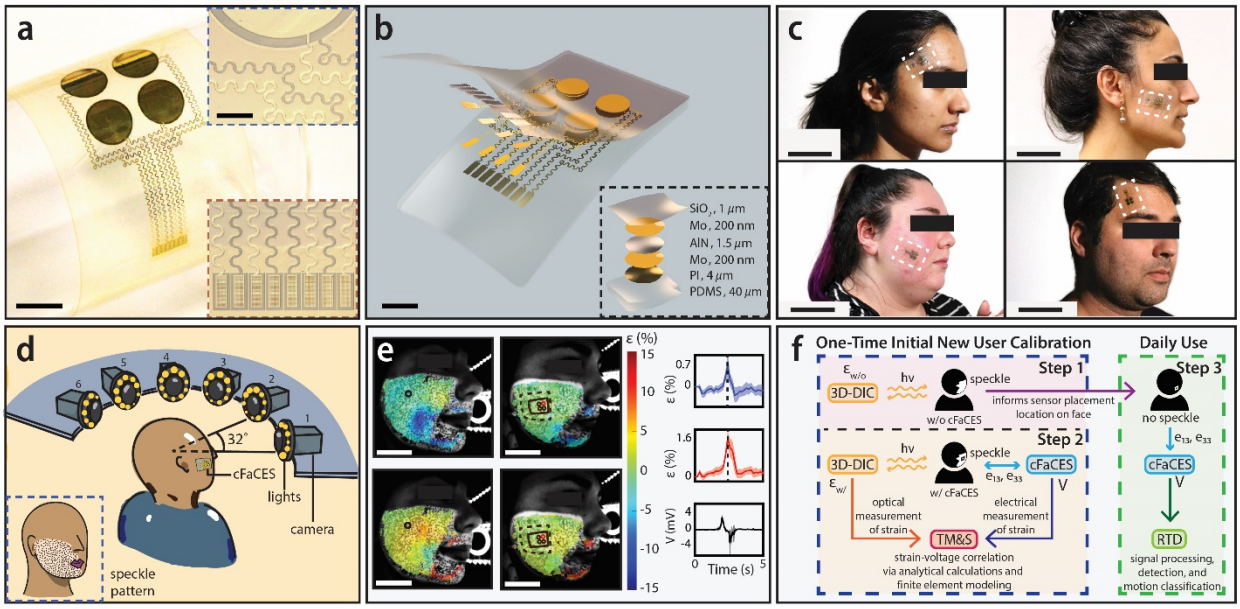

Fig. 1 | The system overview accompanying a conformable Facial Code Extrapolation Sensor, cFaCES. The conformable Facial Code Extrapolation Sensor (cFaCES) is a system which involves measurements via: (i) a conformable sensor for real-time detection of facial motions via electrical response to localized strains and (ii) a non-contact photogrammetry and three-dimensional digital image correlation (PG + 3D-DIC) setup for determining full-field mechanical strains on the face via multi-camera optical imaging. **a**, The conformable sensor laminated on a curved glass cylinder. Scale bar, 5 mm. Insets: edge of the AlN sensing element and its top and bottom Molybdenum (Mo) serpentine electrodes (top right), and the set of eight

serpentine electrodes from four sensing elements connecting to Al bonding pads (bottom right). Scale bar for both insets, 1 mm. **b**, Exploded view of a cFaCES, including each layer encapsulating the sensing elements (bottom right inset). Scale bar, 5 mm. **c,** The cFaCES (white dashed box) laminated on various subjects in different locations of the face, such as cheek and temple. Scale bars, 5 cm. **d**, Schematic diagram of the PG + 3D-DIC setup showing the concept of 3D reconstruction of the face using an array of cameras with overlapping field of view. Random speckling of the face (bottom left) is required to allow for image point matching, resulting in reliable 3D reconstruction and subsequent calculation of skin strain occurring during epidermal deformations. **e**, Skin strain and sensor voltage output are analyzed while subjects perform facial motions, such as right cheek twitch, depicted here. Four inset images show strain maps as an example of the results from 3D-DIC trials of a human subject with the sensor (left) and without the sensor (right), showing minimal principal strain (top) and maximal principal strain (bottom). Line drawings atop the right two images indicate the location of the cFaCES (solid box) and its four active elements (solid circles) and Tegaderm® tape (dashed box). The black circle atop the left two images indicates the area of the skin on top of which the cFaCES element of interest was located during DIC trials with the sensor laminated on the face. The strain scale (%) is given to the right of the strain maps. Three graphs to the right plot minimal principal strain (top, blue) and maximal principal strain (middle, red) measured on the top layer of the cFaCES (adhered to skin with Tegaderm tape) via 3D-DIC, and the resultant voltage output (bottom, black) from one (red circle) of the four sensor elements. For each five-second period, averaged strain across the DIC-generated triangles (n = 21) corresponding to the sensing element from which voltage is measured is represented as a solid line, while the shaded band indicates standard deviation. In all DIC-generated images presented in this work, the eyes of the subjects are blocked with black boxes to maintain privacy. Scale bars, 5 cm. **f,** Flow chart of the key elements of the system. The system, after a one-time initial calibration period for a new user, can be utilized as a daily nonverbal communication tool without further

calibration. (Step 1) The patient's bare facial skin is speckled and optical ($h\nu$) measurement of strain $\epsilon_{w/o}$ is conducted while the patient forms various natural facial motions to inform later placement of the cFaCES on the facial skin. This step can help to maximize distinguishability between distinct motions. (Step 2) After lamination of the cFaCES on the patient's cheek or temple, the facial skin is speckled and optical ($h\nu$) measurement of strain $\epsilon_{w/}$ is conducted simultaneously with electrical measurement of the voltage output (V) of the cFaCES, which occurs via the e_{13} and e_{33} modes of piezoelectricity. The two methods of strain measurement are connected via bimodal (analytical calculations and finite element modeling) theoretical modeling and simulation (TM&S) to achieve voltage-strain correlation. This helps achieve predictable real-time decoding performance in vivo. (Step 3) The cFaCES is laminated on the face, as informed by analysis of contour maps generated by 3D-DIC in Step 1, and the piezoelectrically generated voltage waveforms undergo signal processing, detection, and motion classification.

Chapter 2: Characterization of Conformable Sensor and Facial Skin Using 3D-DIC

2.1 Characterization and theoretical modelling of piezoelectric thin film mechanics

Measurements on controlled, uniaxial buckling, tensile (stretching), and compressive stages with an Instron (MicroTester 5948, Norwood, United States) machine (Fig. 2a) reveal quasi-static mechanical properties of the cFaCES as a bare sensor as well as when coupled with 2 mm-thick mock skin (Dragon Skin, Smooth-On), so as to simulate *in vivo* behavior when laminated on human skin. Fig. 2 displays the results of uniaxial buckling and stretching of a cFaCES laminated on a mock skin. The neutral mechanical plane (NMP) of the cFaCES is located within 110 nm of the midplane of the piezoelectric active layer (Fig. 2b, Note S2). Inclusion of the use of Tegaderm® tape for application on human skin shifts the neutral mechanical plane negligibly, maintaining it within the aforementioned range (Fig. S13). Cyclic tests of cFaCES buckling with buckling centerline in the middle of the piezoelectric array and for buckling distances up to 8 mm (ROC = 1 mm) show negligible (< 200 μV) peak-to-peak voltage outputs (Fig. S13d). For buckling distances of 2 mm of the bare sensor (ROC = 3 mm) with buckling centerline through two of the piezoelectric elements, the maximum strain experienced by the cFaCES piezoelectric element during *in vitro* trials is only 0.0185%, resulting in maximum voltages of ~200 μV (Fig. S14). Given that the maximum strain allowable on wurtzite phase AlN is ~0.09%[46], the minimum radius of curvature (ROC), for buckling with centerline through two of the piezoelectric elements, that cFaCES can support is 834 μm (Note S2). This property of the cFaCES fixes its steady-state voltage output to approximately zero volts regardless of the initial curvature of the object upon which it is placed, which is critical for a device that can be used predictably by a wide variety of subjects. The strain distributions and voltage outputs as predicted by theoretical calculations quantitatively characterize the nature of deformations

occurring on the cFaCES, as a bare sensor when buckled (Fig. S14a) or stretched (Fig. S14b), and when coupled with a mock skin and the resultant structure is buckled (Fig. 2d) or stretched (Fig. 2e). For cyclic compression, similar studies are conducted for the sensor on mock skin without and with Tegaderm tape (Fig. S15a, S15b), as well as for the bare sensor (Fig. S15c). The voltage outputs of the cFaCES as a result of the aforementioned cyclic deformation conditions at a variety of amplitudes are displayed in these figures, revealing that they are similar to predictions from two theoretical modalities: finite element model (FEM) simulations and analytical calculations.

For development of the voltage-strain correlation system, mechanical behaviors and voltages determined experimentally by cyclic, controlled deformation patterns of buckling, stretching, and compression of the cFaCES, whether bare or coupled with a layer of mock skin, are predicted with an analytical model. Buckling behavior is inherently nonlinear, and the partial differential equation governing the vibrations of post-buckled piezoelectric beams [47–52] is similar to the equations of buckling for a unimorph beam [48]. Derived by combining those of a buckled beam [53] and a piezoelectric energy harvesting bimorph [54,55], the governing equation for buckling of piezoelectric beams is as follows:

$$m\frac{\partial^2 w}{\partial t^2} + c\frac{\partial w}{\partial t} + EI\frac{\partial^4 w}{\partial x^4} + [P - \frac{EA}{2L}\int_0^L (\frac{\partial w}{\partial x})^2 dx]\frac{\partial^2 w}{\partial x^2} + \alpha[\frac{d\delta(x)}{dx} - \frac{d\delta(x-L)}{dx}]V(t) = 0 \quad (1),$$

where m is the total mass per unit length of the beam, $w(x,t)$ is deflection along the z-axis, EI is the equivalent bending stiffness of the composite beam, P is the axial load applied by the material testing system, EA is the equivalent axial stiffness of the beam, L is the length of the beam, α is the piezoelectric coupling coefficient, $\delta(x)$ is the Dirac delta function, and $V(t)$ is the voltage across the piezoelectric element. If the width of the beam is noted by b, the thickness of

the substrate by t_s, the thickness of the piezoelectric layer by $t_p$and the transverse piezoelectric coefficient by e_{13}, the piezoelectric coupling coefficient is then $\alpha = 2be_{13}\frac{t_s+t_p}{2}$

The continuous equations of motion are discretized using the assumed-mode method, and the buckling mode shapes are taken to be the same as the vibration mode shapes of a pinned-pinned beam. The axial force applied by the Instron is larger than the first critical load but not the critical load of the higher modes. We, therefore, only consider the fundamental mode shape of buckling [53,56,57]. The fundamental mode shape of the simply supported beam is $\phi(x) = A\sin(\frac{\pi x}{L})$, and the deflection of the beam can be written as a function separable in space and time, $w(x,t) = \phi(x)T(t)$. The differential equations governing the vibrations of the first mode of coupling are:

$$\begin{cases} M\ddot{T} + c\dot{T} + (K-p)T + NT^3 + \beta V(t) = 0 \\ C_0\dot{V} + \frac{V}{R} = -\beta\dot{T} \end{cases} \quad (2),$$

where the modal mass is $M = m\int_0^L \phi^2 dx = \frac{mA^2L}{2}$(the mass-normalized mode shapes are used), the linear stiffness coefficient is $K = EI\int_0^L \phi^{(4)}\phi dx = A^2EI\frac{\pi^4}{2L^3}$, the damping of the beam is characterized by c which is related to the damping ratio as $c = 2\zeta\sqrt{MK}$. The reduction of the stiffness coefficient due to the axial force is $p = -P\int_0^L \ddot{\phi}\,\phi dx = AP^2\frac{\pi^2}{2L}$, the nonlinear coefficient is $N = -\frac{EA}{2L}\int_0^L (\dot{\phi})^2 dx\int_0^L \ddot{\phi}\,\phi dx = A^4EA\frac{\pi^4}{8L^3}$, the coupling coefficient is $\beta = \alpha[\dot{\phi}(0) - \dot{\phi}(L)] = -2\alpha A\frac{\pi}{L}$, and the total capacitance of the piezoelectric layer is $C_0 = 2\frac{\epsilon_0 bL}{t_p}$.

If the axial force is larger than the critical force, which leads to buckling, p will be larger than K, and according to Lyapunov stability theory, in that situation, the zero deflection equilibrium

becomes unstable. This condition, however, creates two new static equilibrium points located at $T = \pm\sqrt{\frac{p-K}{N}}$. The deflection of the beam results in the decrease of its length. If the uniform axial deformation is neglected compared to the geometric effects, the shortening of the beam is $u = \int_0^L \frac{1}{2}(\frac{\partial w}{\partial x})^2 dx = \frac{(AT(t))^2\pi^2}{4L}$. The governing differential equations in Eq. 1 are valid when the axial load is controlled or known; however, in some of the tests, the axial displacement is controlled instead, for which a modified governing equation is used (Note S3).

As another method of theoretical prediction, full three-dimensional multi-physics modeling via COMSOL software (Solid Mechanics, Electrostatics, and Electrical Circuits modules) was used to generate a FEM of the multi-layer sensor in greater detail (see Methods section for further details). Both analytical and FEMs predict the mechanical behavior and voltage output of the cFaCES accurately (Fig. 2). The accurate prediction of the analytical model [47–52] stems from its accounting of the geometric nonlinearities of the post-buckled beam, indicating that the single-mode model is an accurate approximation of the piezoelectric sensor even in a fully nonlinear testing situation. For example, during certain motions, such as pursed lips (PL), the cheek skin may pucker inward due to stretching of skin over an internal mouth cavity. For such cases, the strain maps in Fig. 2e are representative, demonstrating that during stretching on mock skin there occurs some low-amplitude concave buckling, which results in voltage waveforms different from that of convex buckling (Fig. 2d).

The extent of nonlinearities resulting from axial loading of the sample scale with the amplitude of mechanical excitation. The bare sensor buckles under axial loads of less than ~1N (Fig. S14a, Note S4). Laminating the cFaCES on a sample of 2-mm thick mock skin, however, increases the critical buckling load of the system under study and, thus, changes the voltage response of

the cFaCES (Fig. 2d). At low levels of excitation, the beam motion involves an impulse both at the moment of application of the buckling load as well as at its removal, but at larger values of axial deformation, the impulse at the point of force removal disappears. Uniaxial stretching deformations cause significant axial tension in the sample. As a result, the mock skin slides out of Instron clamping jaws and leads to buckling behavior in addition to tensile behavior. To simulate the effects of the sliding of the specimen out of the jaws, an axial constant force was incorporated into the FEM simulation, an approach based on [48,53]. In post-buckled vibrations of the beams, the effect of axial displacement (Note S3, equation (S5)) is similar to the effect of excitations in the form of an axial force (equation (1)). Identifying the amount of the axial pull out of the specimen by identification of the equivalent axial force in the governing equations thus allows for accurate modeling of mechanical behavior of the bare cFaCES in the stretching tests (Fig. S14b) in a manner similar to that for the buckling tests (Note S4). Axial force amplitudes for stretching of the cFaCES-mock skin system are higher than that for the bare sensor. The post-buckled, bi-stable behavior, therefore, is clearly visible in the results of this experiment (Fig. 2e). The strain distributions along the cFaCES-mock skin system for stretching and bending cases are depicted in Figures 2d and 2e, respectively. Compression forces on the cFaCES and cFaCES-mock skin system are similarly modeled (Note S5, Fig. S16) and confirmed experimentally. These findings establish the cFaCES as a robust, versatile tool for characterizing mechanical deformations on soft, elastomeric substrates *in vitro*.

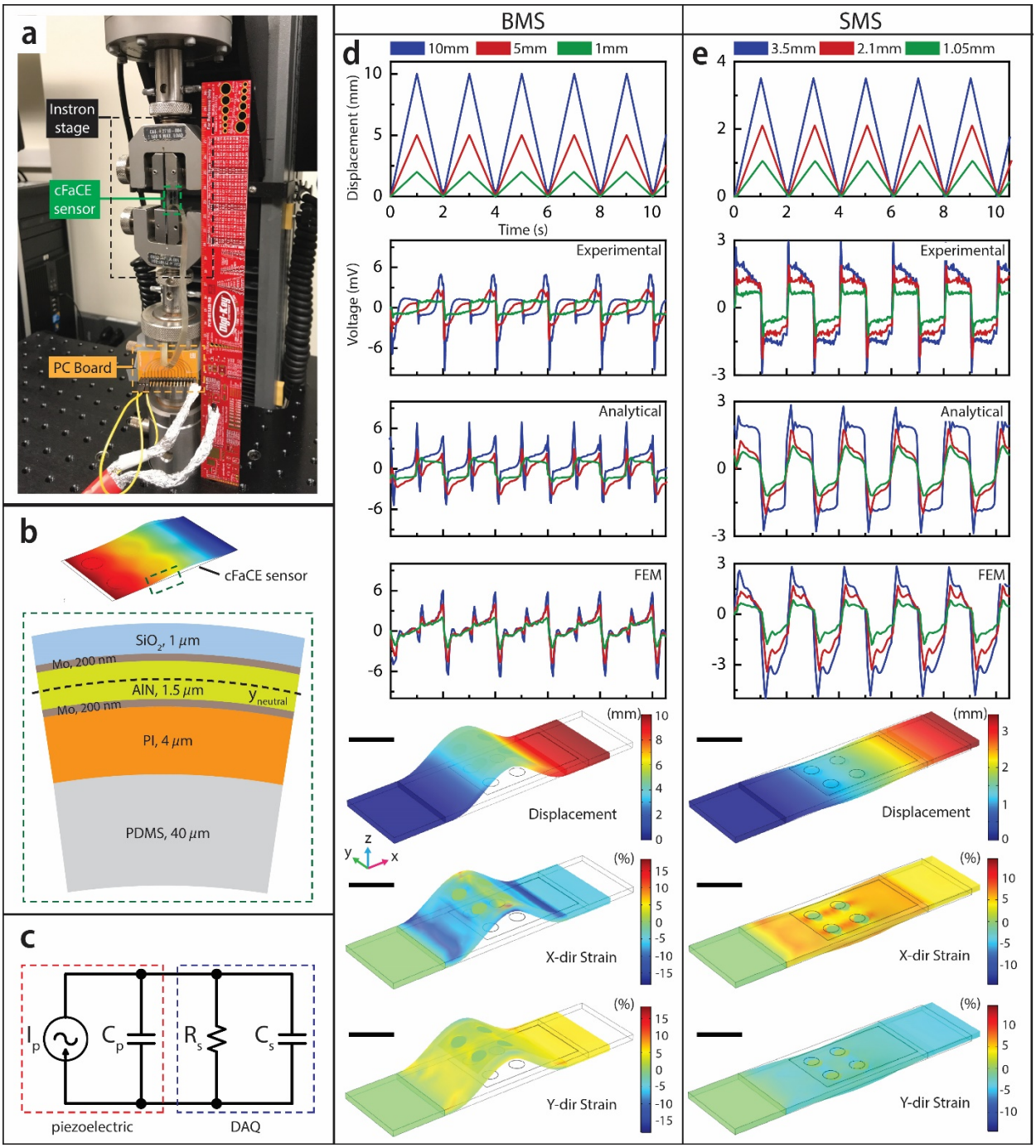

Fig. 2 | *In vitro* mechanical characterization of the cFaCES on a mock skin. Voltage output resulting from uniaxial buckling and stretching of the cFaCES placed on a mock skin serve as a first-order, controlled approximation of the expected behavior of the sensor on human skin. **a,** An optical photograph of the test setup on the Instron machine shows the clamping of the cFaCES system, whether bare or on a mock skin. From the unperturbed state, one end of the

system is either pushed closer, resulting in buckling behavior, or pulled away, resulting in tensile stretching behavior. The electrical output generated by the four sensing elements of the sensor are carried via an anisotropic conductive film (ACF) cable connected to a printed circuit board (PCB), which is then connected via a shielded coaxial cable to the data acquisition (DAQ) system. **b,** The neutral mechanical plane, $y_{neutral}$ (black dashed line), of a cFaCES is located in the middle of the piezoelectric layer as shown in the cross section drawing (green dashed box). **c,** The finite element model simulates a single sensing element (red dashed box) as a current source I_p in parallel with a capacitor $C_p = 807pF$, which mimics the piezoelectric charge-generating behavior. In order to accurately predict the voltage values measured from the sensor, the DAQ system (blue dashed box) is included in the model as a parallel combination of a resistor and capacitor ($R_s = 1M\Omega || C_s = 265pF$) connected to the two-wire output of the piezoelectric element. **d-e,** Voltage outputs from one sensing element as observed experimentally and predicted via analytical and FEMs, in addition to strain fields predicted by the FEM, are shown for the case of buckling (BMS) (**d)** and stretching (SMS) **(e)** motions for the sensor-on-mock-skin system. The time scale is the same for all graphs in (**d)** and **(e)**. Deformation and strain fields are shown in the deformed configuration for the highest axial displacements for buckling (10 mm) and stretching (3.5 mm). The outline of the undeformed cFaCES-mock skin system is shown by the thin gray wireframe in each strain map. The deformation (mm) and strain (%) scale for each strain map is given directly to the right. Scale bars, 2 cm.

2.2 *In vivo* characterization during facial deformations

Subsequent *in vivo* study of soft tissue biokinematics via PG and 3D-DIC completes the system presented herein, since the resultant spatiotemporal strain readings can be used to interpret sensor readings from a cFaCES when laminated on facial skin during facial deformations. Study

of epidermal strain signatures resulting from 16 different facial deformations are studied, and the effect of these deformations on different regions of the face, such as cheek and temple, as well as the resultant strain and voltage output on the cFaCES when laminated on those regions, are compared.

Initial 3D-DIC tests characterize the properties of the subject's facial skin. The protocol for *in vivo* 3D-DIC experiments is outlined in the Methods section. Experiments are first conducted on the facial skin without the cFaCES laminated, resulting in quantitative measurement of full-field skin strains during various types of natural deformations (Movies S2, S3, S4). The resulting minimal and maximal principal strain maps for representative motions are shown in Fig. 3a, c, e, and g. Strain fields between different subjects for the same motion show roughly similar areas of maximum strain, with differences in magnitude or specific spatiotemporal signatures of strain that could be attributed to subject age [18], deviations in motion execution across different subjects, as well as potential muscular atrophy in ALS patients. All procedures in the healthy and ALS subject tests were in accordance with the experimental protocol approved by the Committee on the Use of Humans as Experimental Subjects in Massachusetts Institute of Technology (COUHES # 1809531633), and the participants gave informed consent.

The results of further 3D-DIC experiments in which a cFaCES is laminated on human facial skin characterizes its behavior *in vivo* (Movies S5, S6, S7). Lamination of the cFaCES on the skin as shown in Fig. 3b, d, f, and h, decreases the magnitude of the observed strain in the sensor area, which results from the sensor's absorption of the mechanical energy generated by muscle movements underlying skin deformation. Given that mechanically coupling different materials results in different equilibrium and compatibility constraints in the composite skin-cFaCES system, there results an altered stress-strain distribution throughout materials and on the material interfaces. Detailed calculations and explanations of this phenomenon are discussed in

Supplementary Note S6. Representative results for healthy and ALS subjects for all motions, with and without cFaCES laminated on the face, are shown in Figs. S17-S28. An extensive study on the repeatability of strain field measurements for the same movement and the same subject for testing situations with and without cFaces lamination is demonstrated in Figs. S29-S122; small differences in magnitude or strain waveform shape can also be attributed to slight deviations in an individual subject's repeated motion execution over multiple trials.

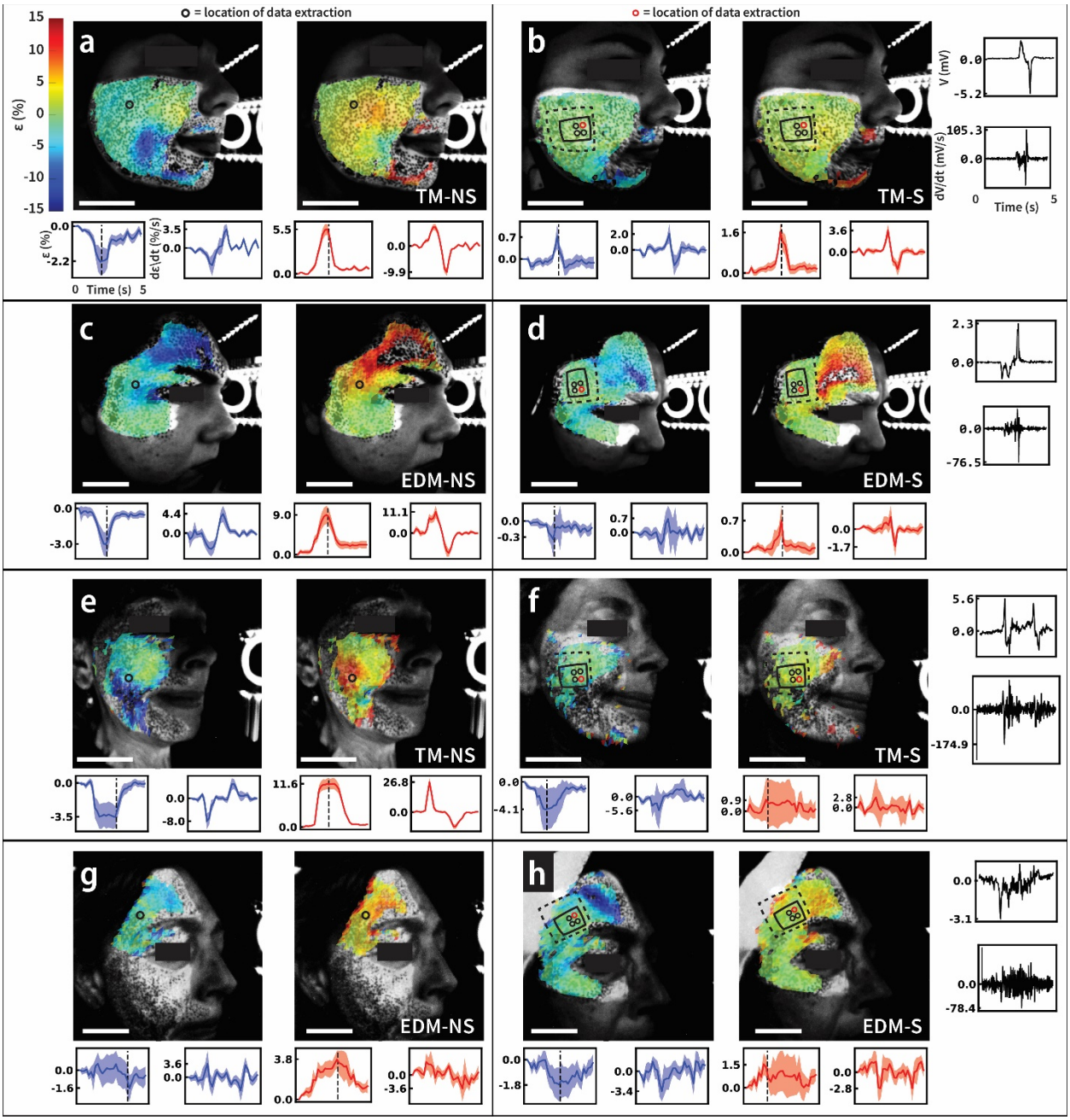

Fig. 3 | *In vivo* mechanical characterization of the cFaCES on facial skin of healthy and ALS subjects. a-h, Using 3D-DIC, evaluation of facial skin and the top surface of a cFaCES when laminated on facial skin *in vivo* characterizes the mechanical interactions between the cFaCES and facial skin. Analyses for two motions are shown: twitch medium magnitude (TM), and eyebrow-down medium magnitude (EDM). The left column **(a, c, e, g)** depicts all results for skin strain without the sensor on the face, denoted as the suffix -NS (no sensor), and the right

column **(b, d, f, h)** depicts all results for skin strain with the sensor on the face, denotes as the suffix -S (sensor). Images depict strain maps in which strains calculated via DIC algorithms run on two pairs of cameras are overlaid on the raw images captured by PG. The strain maps shown are associated with the frame in which peak strain occurred in the area of the sensor (S) or in the area of the skin directly underneath where the sensor was placed (NS). The strain scale (%) for all strain maps is given in the top left corner. Line drawings atop the strain maps from trials with the sensor indicate the location of the cFaCES (solid box), its four active elements (solid circles), and Tegaderm® tape (dashed box). The sensing element from which voltage data and atop which strain data was collected is marked by the red circle. For each of the displayed eight cells, the left-side images and blue graphs (left: strain, ϵ (%), right: strain rate $\frac{\partial \epsilon}{\partial t}$ (%/s)) display results for minimal principal strain, and the right side the same for maximal principal strain (red graphs) as measured on the top surface of the Tegaderm® tape layer, which secured the cFaCES to the skin. For each five-second period, averaged strain across the DIC-generated triangles (n ≥9) corresponding to the sensing element from which voltage is measured is represented as a solid line, and the shaded band indicates standard deviation. The peak strain is denoted in each of the strain graphs by the dashed black line. Voltage (top) and voltage rate (bottom) graphs (black) display the output of the denoted sensing element. Cells **(a), (b), (c)** and **(d)** correspond to a healthy subject, while cells **(e), (f), (g)** and **(h)** correspond to a subject with ALS. Representative strain maps and graphs for all 16 motions are shown for each patient in Figs. S17-S28. Results of five repeats of the same motion for each subject and each motion are available in Figs. S29-S122. Axes titles and units as given in A) are the same for all like graphs. Strain maps and graphs include only triangles for which the correlation coefficient was lower than 0.4. The time scale is the same for all graphs. Scale bars, 5 cm.

2.3 Modelling of device behaviour during facial deformations

Since the piezoelectric elements transform mechanical energy into electrical energy, the observed experimental voltages in 3D-DIC trials can be used to predict the strains expected from the DIC measurements of the top surface deformation of the sensor when laminated on the skin. Assuming the cFaCES sensing element area is small enough that the strain is constant over the area of each sensor element, one can write the following analytical expression for the sensor voltage:

$$C\frac{dV}{dt}+\frac{V}{R}=e_{31}A\frac{d}{dt}(\epsilon_1+\epsilon_2) \quad (3),$$

where C is the capacitance of the sensor, R is the shunt resistance of the DAQ, e_{31} is the effective piezoelectric stress coefficient, A is the area of the piezoelectric element, ϵ_1 and ϵ_2 are the strains in the two principal strain directions and $\epsilon_1+\epsilon_2$ represents the trace of the eigen-decomposed strain tensor where out-of-plane strain, ϵ_3 is immeasurable and assumed negligible for this calculation [58]. The facial gestures do involve shear strains, evident from the appearance of wrinkle lines during some deformations. The buckling showcased by the wrinkles indicates compressive strain normal to the wrinkles and tensile strains along the wrinkles. A combination of compressive and tensile shear strains creates notable shear strains in the non-principal directions. The shear strains are only zero if the coordinate axes are chosen along the strain directions. The principal directions could, however, change in time and thus we derive our equations along a global coordinate system. Shear strains do not affect the generated voltage (equation (3)), since the coupling coefficient between the shear strain in the X-Y plane and electrical displacement in the Z axis is zero. The non-zero coupling coefficient associated with shear deformation is d_{15}, which involves shear deformation along X-Z plane and requires electrodes on the lateral surfaces (normal to the X axis).

The voltage output of the cFaCES, which has electrodes in the Z direction, correlates with the sum of the planar normal strains, or the surface strain tensor trace (ϵ_s), which represents the 3D-DIC-measured value of $\epsilon_1 + \epsilon_2$ from equation (3). To estimate ϵ_s from the cFaCES-generated voltage, a transfer function is determined. To include all the sensor layers and improve the accuracy of this model the full finite element model discussed earlier is used instead of the approximate formulas (equations (1,2)). For this purpose, we first find the transfer function between the strain on the top surface of the sensor and the output voltage in our FEM. We assume the strain to be a chirp signal and run the FEM to evaluate the voltage output. We then arrive at the transfer function by dividing the Fourier transform of the output by the Fourier transform of the input. The following transfer function is an accurate match for the evaluated transfer function: $\frac{\epsilon_1(\omega)+\epsilon_2(\omega)}{V(\omega)} = \frac{Cj\omega+1/R}{\kappa j\omega}$, where κ is the piezoelectric coupling coefficient evaluated from the FEM simulations. This equation can be further simplified by noting that the skin deformation frequencies are in the order of few Hz, while the resonant frequency of the piezoelectric transfer function is $f = \frac{1}{2\pi RC} \approx 148Hz$. This simplifies the transfer function to: $\frac{\epsilon_1(\omega)+\epsilon_2(\omega)}{V(\omega)} = \frac{1}{R\kappa j\omega}$. This transfer function is used to predict the strain on the top layer of the cFaCES + Tegaderm® tape when the piezoelectric voltage output is known.

The resulting predicted values of strain compared to those measured using 3D-DIC are shown in Fig. 4a and 4B for a few representative motions performed by healthy and ALS subjects, respectively. Measured strains from 3D-DIC show qualitative agreement with strains predicted from the cFaCES voltage output for most of the motions for both the healthy and ALS patient (Fig. S123, S124). While the exact magnitudes are off due to the simplifying assumptions made in the FEM, the complexity and strain anisotropy of the deformations, i.e. surface wrinkling, and limitations on camera and speckling resolution in 3D-DIC (Note S6, Fig. S125), the qualitative close match offers an accurate predictive power for strain shape, and thus epidermal

deformation signature. Asynchronous timing of voltage and strain measurements may result in slight time offsets between experimental observations and theoretical predictions. Results of integration of 3D-DIC-measured strains with cFaCES-measured voltage via theoretical modeling, prediction, and validation, thus provide methodologies for establishing predictable and verifiable voltage-strain correlation of cFaCES *in vivo.* This means that local deformation signatures resulting from different facial motions can be predicted based on cFaCES voltage behavior, setting the stage for explorations with real-time decoding.

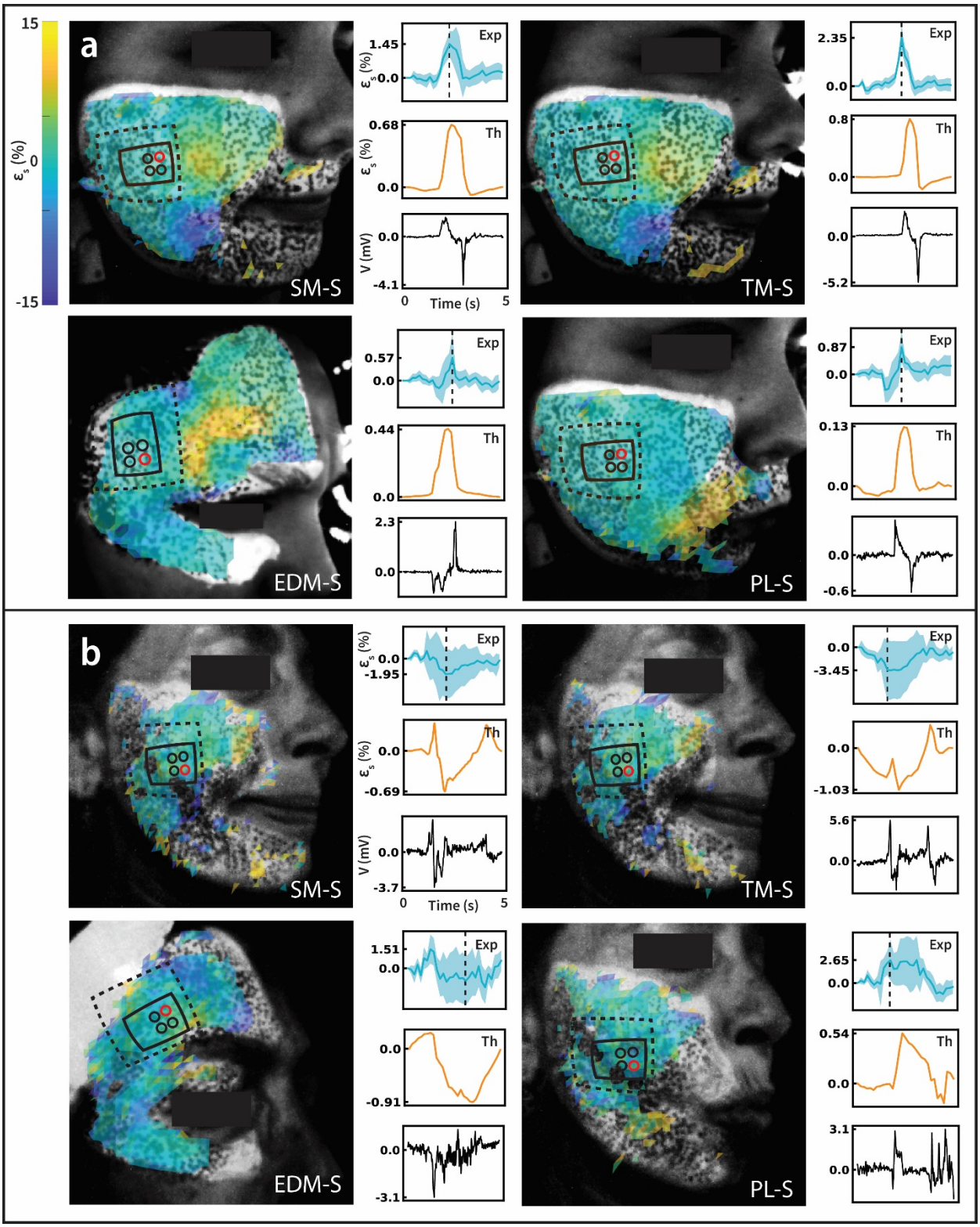

Fig. 4 | 3D-DIC and theoretical modeling for prediction and validation of cFaCES performance *in vivo*. a-b, Experimental (Exp) surface strain tensor trace (with ϵ_s) (blue) and

cFaCES voltage (black) data simultaneously collected and recorded while the subject performed various facial motions were analyzed to determine the validity of measured strains and the capability of the theoretical model to predict surface (top of Tegaderm® tape layer) strain given the sensor voltage output. For each five-second period, averaged ϕ across the triangles ($n \geq 9$) generated by DIC corresponding to the sensing element from which voltage is measured is represented as a solid line, and the shaded band indicates standard deviation. The peak strain is denoted in each of the strain graphs by the dashed black line. Voltage graphs (black) display the output of the denoted sensing element (red circle). Theoretical (Th) prediction (orange) of *in vivo* with ϵ_s from the voltage output of a cFaCES when laminated on facial skin is qualitatively and quantitatively similar to the experimentally observed strains from 3D-DIC under the same conditions for the healthy subject, but deviate for the ALS subject. Images depict spatiotemporal with ϵ_s maps in which strains calculated via DIC algorithms run on two pairs of cameras are overlaid on the raw images captured by PG. The strain maps shown come from the frame in which peak strain occurred in the area of the sensor. The strain scale bar (%) applying to all strain maps is given in the top left corner. Line drawings atop the strain maps from DIC trials with the sensor indicate the location of cFaCES (solid box) and its four active elements (solid circles) and Tegaderm® tape (dashed). The sensing element from which voltage data and atop which strain data was collected is marked by the red circle. Results shown in **(a)** are from a healthy subject and in **(b)** are from an ALS subject. The time scale is the same for all graphs.

Furthermore, 3D-DIC results without the sensor can be utilized to determine a sensor placement location such that the four piezoelectric elements of the cFaCES experience computationally distinguishable epidermal deformation signatures, i.e. spatiotemporal strain profiles, during distinct motions for an individual. This is useful for real-time decoding (RTD), in which the sensor should be placed such that each motion can be uniquely identified by the measured voltages in each sensing element. Given that the sensor remains laminated in the same location

during the occurrence of different facial motions, the goal is to maximally differentiate the voltage waveforms generated by the four cFaCES piezoelectric elements.

Most biomedical sensor designs lack an in-depth study of the target soft tissue before the design and fabrication of the sensor meant to couple to that tissue. In this study, we propose the use of 3D-DIC as a method for in-depth biokinematic study of the target region upon which a sensor with mechanically-active functional material, such as piezoelectrics, will be placed. Similar to how chemical assays of a body part would be conducted before designing medication for disorders of that body part, so too does 3D-DIC allow for the mechanical study of biological soft tissue before designing the mechanically-active functional materials on mechanically-adaptive substrates that are meant to intimately integrate with that soft tissue. We specifically utilize 3D-DIC results to determine the validity of the size and spacing of AlN piezoelectric elements (see “Device Design Considerations” in Methods). Indeed, given the above discussion demonstrating sensor voltage correlation with with ϵ_s (Fig. 4), contour maps (with isolines of measured with ϵ_s) can be generated from 3D-DIC results and used to determine sensor design parameters and sensor placement location. For determining sensor placement location, these contour maps for different motions are made translucent (50%) and overlaid on top of each other (this process is repeated over three time points during the facial deformation) to determine, by inspection, an area of facial skin where the four cFaCES piezoelectric elements would experience distinct spatiotemporal strain signatures (Fig. 5), which could purportedly lead to computationally distinguishable voltage waveform signatures. Future automation of determining a sensor placement location via code written to analyze the spatiotemporal strain contours would be possible using machine vision algorithms.

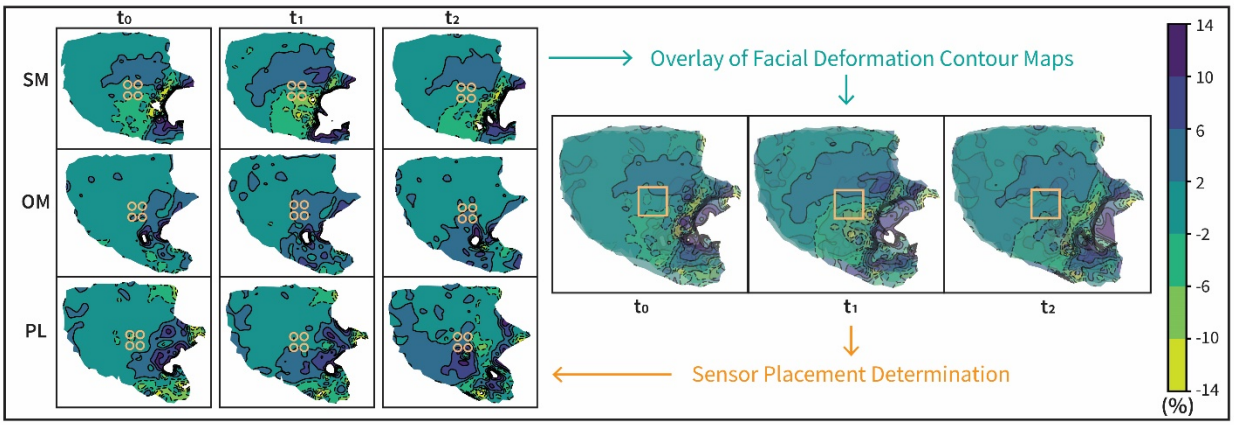

Fig. 5 | Sensor placement for real-time decoding informed by analysis of skin strains from 3D-DIC. Contour maps generated from skin strains without a cFaCES laminated on the skin help to guide placement of cFaCES on facial skin such that the strain observed by each of the four sensing elements is temporally distinct for different motions. Overlaying contour maps from similar motions observed at the peak strain allows qualitative selection of sensor placement. The orange square indicates a potential location for the four sensing elements that would result in distinct strain observations on each element.

Chapter 3: Pilot Studies for Real-time Decoding and Classification of Facial Deformations

When laminated on the facial skin, this low-cost, mass-manufacturable cFaCES thus enables the creation of a library of motions from which a large subset of human language could possibly be inferred. The size of this subset depends on the method of mapping facial motions to language as well as the number of distinct facial motions chosen for decoding. The final number of motions chosen for decoding will depend on the number of phrases or ideas desired to be communicated as well as the chosen mapping strategy. As an example, Fig. 6a shows how different strategies for this mapping, i.e. direct, tree, conditional, affect the total number of possible ideas or actions the user can communicate using seven motions. The motion library can be created by each user, based on their preferences and comfort. Each motion can be classified as one of the motions in the library via a real-time decoding (RTD) algorithm, which uses a dynamic-time warping, K-nearest neighbors (KNN-DTW) model [59–61], as depicted in Fig. 6a. The KNN-DTW algorithm predicts the most likely motion based on calculating the distance between each of the voltage waveforms detected during testing with all the detected waveforms in the training set for the model. Motion classification relies on calculating the distance between sets of voltage waveforms from two motions. It is important to note that the KNN-DTW algorithm effectively compares the voltage waveform shapes rather than voltage values or principal-component analysis. For each detected motion, n voltage waveforms are captured, each one corresponding to a particular sensing element on cFaCES. Distances d_i between the voltage waveforms corresponding to the same element i are calculated, and the root-mean square value is then calculated to get the total distance, $d = \sqrt{\sum_{i=1}^{n}(d_i)^2}$, between an observed signal and a signal in the training set, where n is total number of sensing elements. Each distance d_i is calculated from DTW, and specifically an approximation for DTW which coarsens temporal

resolution of the voltage waveform, computes a warped distance matrix between two signals at that lower resolution, and projects that matrix back into finer resolution. This algorithm has previously been developed and built into a Python library called fastdtw [62], which was adapted for use in this KNN-DTW model. Once the total distance between the detected motion and each of the motions in the training set is calculated, the K nearest neighbors, i.e. voltage waveform sets with the K lowest total distances, are identified and their motion labels are used to determine the weighted-average probabilities of each motion label. The motion with the highest probability is dubbed the "classification" of the detected motion.

In the RTD system, a cFaCES is laminated on the facial skin and connected to a custom-built signal-processing board (SPB) that performs differential voltage amplification, analog signal filtering, and analog-to-digital conversion (Fig. S126), and whose output is connected to a Raspberry Pi (RPi), for portable applications. The onboard processor on the RPi runs the KNN-DTW algorithm code files, which are written in the Python language (v3.6). Before RTD can be tested, the subject completes a training session which involves performing a motion 12 times. Each motion is identified in the code, and the four-second interval containing the motion-induced voltage output (100 Hz sampling rate) of the sensor is detected, stored, and filtered digitally using a 6th order low-pass Butterworth filter with 6 Hz cutoff frequency. This is repeated for each distinct motion type in the subject's desired library, and forms the calibration set. The subject then performs a series of motions which are classified in real-time using the KNN-DTW algorithm (Movie S8). The extent of the "real-time" aspect of our decoding algorithm is qualified by the average lag time between the end of the user's performance of the motion and the display of the classification result, which is 1.71 ± 0.12 s (Table S3). Evaluation of the RTD system on healthy and ALS subjects involved measuring the testing accuracy, and is depicted in Fig. 6b and 6c, respectively. Eight voltage waveforms are randomly selected from each motion in the calibration set, forming the training set. Testing accuracy refers to the percentage of

motions correctly identified from the remaining 4 voltage waveforms from each motion in the calibration set when predicted using a model containing the training set. Testing accuracies reported here are calculated upon evaluating the RTD model using 3-fold stratified cross validation, resulting in 27 different data set combinations for each combination of piezoelectric elements usable for model evaluation.

For this study, we show results of RTD performed with a small subset of 3 motions (smile medium - SM, open mouth - OM, pursed lips - PL) performed by healthy and ALS patients, and focus on testing the effect of increasing the number of piezoelectric elements n used for classification on the testing accuracy. For a given sensor for which n used for classification on the testing accuracy. For a given sensor for which n elements are usable for RTD, evaluation is performed for every combination of $j \leq n$ elements. RTD evaluation suggests that increasing the number of elements improves the testing accuracy, as shown in Fig. 6b and 6c. Average of overall classification testing accuracies involving only one element are 59.9% ± 2.1% and 59.4% ± 4.7% for the healthy and ALS subject, respectively. For two elements, the accuracies are 74.3% ± 1.4% and 65.0% ± 7.9% for the healthy and ALS subject, respectively. For three elements, the accuracies are 82.7% ± 1.8% and 70.3% ± 10% for the healthy and ALS subject, respectively. For four elements, the accuracies are 86.8% ± 3.0% and 75.0% ± 17.4% for the healthy and ALS subject, respectively. Examples of voltage signals simultaneously recorded from all four elements of a cFaCES laminated on the cheek are shown in Fig. S127. This observation suggests the importance of using multiple spatiotemporal signals, i.e. multiple sensing elements, to improve the accuracy of RTD. The cFaCES design allows for a maximum of four such sensing elements, but further increasing the number of elements used for real-time decoding could potentially make decoding accuracy even higher. Still, it is possible that certain motions may be too similar for a given subject, e.g. the case of OM and PL for healthy subject

(Fig. 6b), and for such cases only one of those motions should be included in the subject's nonverbal communication library to increase decoding effectiveness.

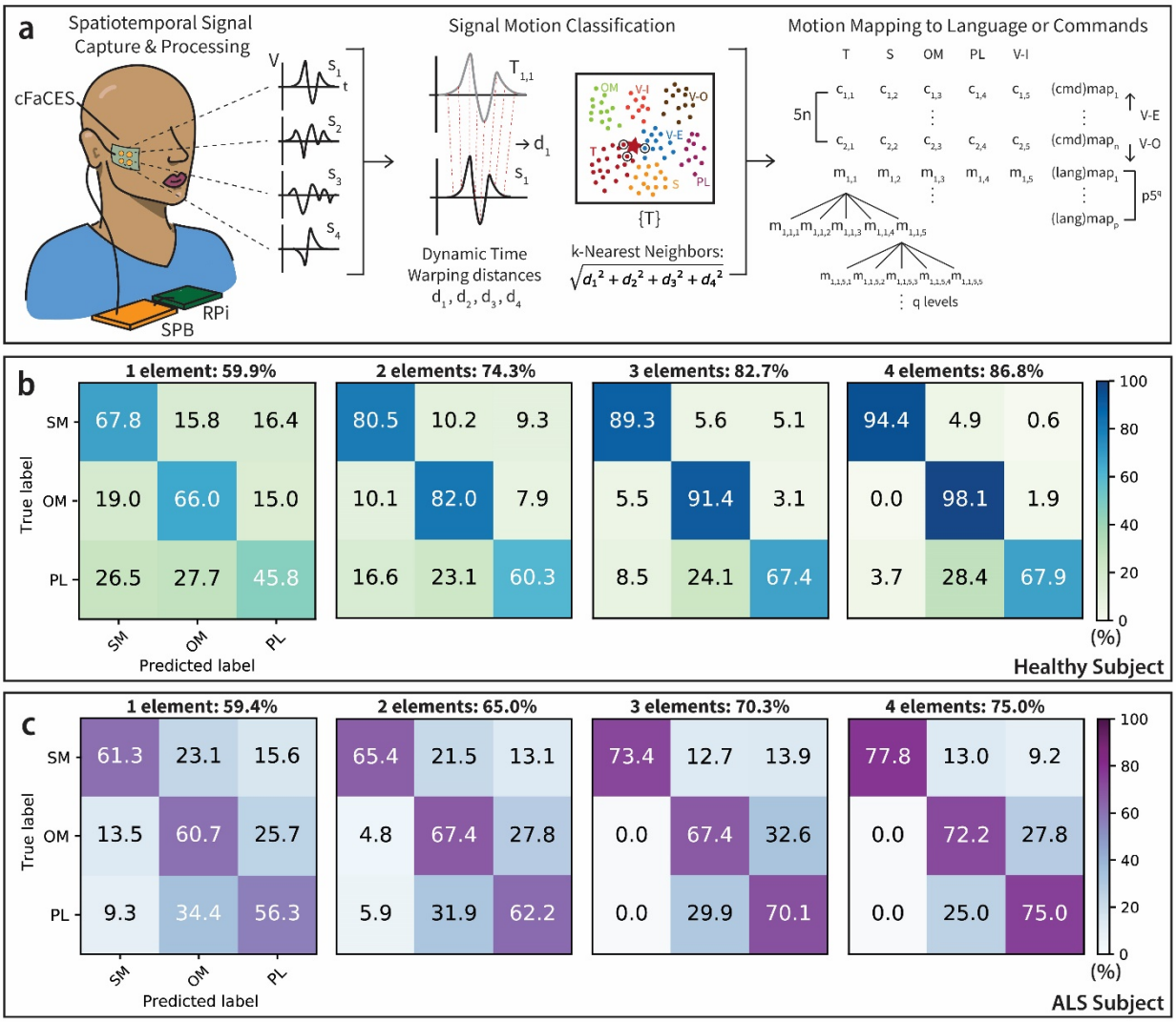

Fig. 6 | Real-time decoding of facial motions and library construction. a, Schematic drawing of the RTD system. A cFaCES is laminated on the face and its four sensing elements are connected to a signal processing board (SPB) for differential signal amplification and analog-to-digital conversion. The digital signal from the SPB is fed to the Raspberry Pi (RPi), which automatically detects facial motions and classifies them as one of the motions in the subject's library of motions. The classification is based on a dynamic time warping, k-nearest

neighbors (KNN-DTW) algorithm, modified to calculate the k=3 nearest neighbors based on the magnitude of efficiently calculated dynamically-time warped distances of each of the four sensing elements' signals, with total distance calculated as $d = \sqrt{\sum_{i=1}^{n}(d_i)^2}$. The classified motion can be used to create a library of any desired size, due to the potential to assign either additive, multiplicative, or exponential meaning to each motion. **b-c,** 3-fold stratified cross validation for model evaluation results in average testing accuracies of the RTD system for an ALS **(b)** and a healthy **(c)** patient, respectively. The average of overall classification accuracies involving only one element are 59.9% ± 2.1% (n = 675) and 59.4% ± 4.7% (n = 135) for the healthy and ALS subject, respectively. For two elements, the accuracies are 74.3% ± 1.4% (n = 783) and 65.0% ± 7.9% (n = 27) for the healthy and ALS subject, respectively. For three elements, the accuracies are 82.7% ± 1.8% (n = 405) and 70.3% ± 10% (n = 27) for the healthy and ALS subject, respectively. For four elements, the accuracies are 86.8% ± 3.0% (n = 324) and 75.0% ± 17.4% (n = 27) for the healthy and ALS subject, respectively. As the number of sensing elements used in RTD is increased, the accuracy of motion classification increases.

In order to evaluate the potential for the RTD system to be used across a wider range of motions, we studied the classification testing accuracy of the KNN-DTW algorithm, again using stratified cross validation, on a set of post-recorded cFaCES single-element signals (Fig. S128). For four, six, and eight motions, the accuracies were 89.3% ± 18.5%, 65.5% ± 16.6%, and 50.1% ± 23.9%, respectively. Given these positive results from one element signals, and the clear potential for improvement of the accuracy with increasing number of elements included in RTD (Fig. 6b, c), it is viable to use the RTD system reported here for a wider range of motions in future studies. Although our study aims to achieve a balance between real-time computational load and decoding accuracy, a further easily achievable increase in testing accuracy could result from increasing the number of voltage waveforms per motion collected in the calibration

set and used in the training set [63,64]. For this representative study, we establish the potential for the cFaCES to be used as part of a nonverbal communication interface.

Chapter 4: Methods

4.1 Device design considerations of a cFaCES

Aluminum nitride (AlN) was used as the piezoelectric material in cFaCES for several reasons: low cost [65], complementary metal oxide semiconductor (CMOS)-compatible processing [34,35], and lead-free nature - making the material more suitable for mass manufacturing, clinical translation, and adoption in future lead-free industrial standards [36,37]. From a processing standpoint, piezoelectric AlN thin films are usually prepared by a reactive sputtering process in N_2/Ar plasma, using an Al target. In this study, the reactive sputtering process is compatible with the standard 8-inch wafer process, making it suitable for mass production [66]. The CMOS-compatible nature of the AlN piezoelectric layer further enables ease of mass manufacturability. Although AlN has lower piezoelectric coefficients than standard thin film piezoelectrics such as PZT [25], PZT is not CMOS-compatible and may suffer from aging and other material property changes over time [67]. As a post-CMOS compatible piezoelectric material, AlN-sputtered thin films are commercially used in fingerprint sensors [68] and thin film bulk-wave acoustic resonator filters [69,70]. Due to its low-cost microfabrication and mass production capability via MEMS technology, AlN-based resonators have been developed and proven to operate above 6GHz for 5G mobile communication [71]. Finally, the KNN-DTW real-time decoding algorithm utilized in this work classifies facial motions based on piezoelectric voltage waveform shapes rather than voltage values (Fig. S127), so the relatively lower voltages generated by AlN piezoelectrics is not an issue in our nonverbal communication technology.

Furthermore, functional AlN thin films have been demonstrated widely on flexible substrates (usually polyimide or polyethylene terephthalate) [32,72–76]; however the use of AlN thin films in conformable, stretchable conditions has not yet been demonstrated due to difficulties in microfabrication processing techniques. Conventionally, high-quality AlN thin films are

manufactured on Si wafers with or without a layer of SiO_2, and thus most AlN MEMS devices are rigid [77–79]. This work presents microfabrication techniques that maintain the CMOS-compatible, low-cost nature of AlN in a conformable form factor for coupling with the highly curvilinear surfaces of the face (Fig. 1) and while remaining operational over high-strain, cyclic dynamic stretching and buckling deformations involved in facial motions on the cheek and temple (Fig. 2, Fig. 3). The full width at half maximum (FWHM) of XRD rocking curve is one well-established criteria to determine the quality of the synthesized AlN along the c-axis. Table S2 compares the FWHM of this work with other studies of AlN thin films on rigid and flexible substrates. Although AlN has been reported to be fabricated on polymeric substrates such as polyimide and parylene, their FWHM of XRD rocking curve are significantly higher than that of AlN on Si or SiO_2, as a consequence of the rough surface of the polymeric substrates and large lattice strain mismatch. In this study, a new microfabrication process has been developed to enable the flexible AlN sensor without undermining the quality of the AlN crystal thin film. The FWHM of the AlN in this work is only 1.69° (Fig. S5, Table S2), fairly close to those on Si based substrates. Therefore, our microfabrication process of AlN maintains cFaCES as a conformable device without sacrificing functionality significantly.

The thickness of the AlN piezoelectric layer was chosen by considering the tradeoff between signal-to-noise ratio (SNR) and bendability of the final device that comes with changing the thickness of AlN. A thicker (thinner) AlN layer results in higher (lower) SNR, due to higher d_{33} coefficient [80], and reduced (greater) bendability. Theoretical modeling results show that increasing the thickness of the AlN layer increases the voltage output of the cFaCES, but decreases the minimum allowable radius of curvature before fracture (Note S2, Fig. S129). Since the KNN-DTW algorithm distinguishes between distinct motions by voltage waveform shape instead of value, the exact thickness of the AlN layer would negligibly affect the detection accuracy, as long as the signal processing circuitry can reliably filter and amplify the voltage

signal generated by this piezoelectric layer. Finally, from a processing standpoint, when growing a thicker AlN layer, more defects appear and the c-axis orientation of AlN is gradually undermined [81]. The non c-axis oriented AlN has negative effects on its piezoelectric properties. In this study, the 1.5 μm thick AlN has been proved to be highly c-axis oriented by TEM and XRD rocking curve (Fig. S5).

Molybdenum was selected as the electrode material due to the reduced lattice mismatch it provides for the piezoelectric layer, as well as its compatibility to the MEMS process. To ensure the high quality of the c-axis texture of the AlN layer, a critical strategy is to reduce lattice mismatch between the underlying metal layer and the AlN layer. The lattice parameter of AlN ranges from 4.978 to 4.982 Å for c-axis. Despite the fact that high-quality AlN has been synthesized on Mo (110), Al (111), Pt (111), Ti (002) and Au (111) substrates due to their reduced lattice mismatch, a large concentration of nitrogen was reported to incorporate into Ti and Al layers, which undermines the electrode conductivity (nitrogen plasma reacts with Al to form AlN during the reactive sputtering process) [34,82–84]. Moreover, Pt, Au and Ag are not CMOS-compatible materials, and they cannot be etched by dry etching processes using MEMS technology. On the contrary, Mo is a CMOS-compatible material, and can be precisely etched by the mixture of O_2/Cl_2/Ar inductively coupled plasma. A Mo bottom layer also provides good adhesion for the AlN layer [85]. Finally, conductive materials for cFaCES were selected such that relatively low-cost, widely available materials that are often used in current manufacturing or microfabrication processes can be used. While conventional electrode materials used in research, such as gold (Au), platinum (Pt), and silver (Ag), could have been used for greater ductility, molybdenum (Mo) electrodes and aluminum (Al) bonding pads were used for their relative low-cost and standard usage in industrial processes [86–88]. The limited thickness (200 nm) and serpentine structures of the Mo electrodes allow for increased stretchability despite lower ductility than precious metals [89].

Silicon dioxide (SiO_2) was chosen as the encapsulation material due to a few processing concerns. The growth of SiO_2 on the silicon (Si) test wafer can ensure a flat surface better than allowable by other polymer materials in terms of surface roughness. The flat substrate surface enables the growth of highly crystalline AlN along the c-axis [90]. The use of SiO_2 as the substrate layer for AlN growth during microfabrication is the primary reason why the AlN layer in cFaCES has similar piezoelectric effect to those grown on rigid silicon, as evidenced by the XRD rocking curve (Fig. S5). Furthermore, SiO_2 is a dielectric material commonly used for the insulation of MEMS devices, so it is a well-known, relatively inexpensive material in standard cleanroom procedures. Additionally, the plane-strain modulus (Note S2) of SiO_2 is 25 times greater than that of polyimide. Therefore, roughly the same neutral mechanical plane of cFaCES can be achieved with a thinner layer of SiO_2 than polyimide, which allows for less material usage.

We utilize our developed theoretical models to study the effects of the design parameters (thicknesses, sizes, shapes, and distances in between elements) on the performance of a cFaCES. Two types of models were developed for this purpose. The first is the finite element modeling (FEM), which can include all intricate details and complexities of the cFaCES. The second are analytical models that rely on effective simplifications of the sensor and give closed-form relations that better reveal the design decisions. There are two key design objectives studied using these models. The first objective is voltage sensitivity (i.e., the amplitude of the generated voltage for a given facial strain). Larger voltage sensitivities enhance the signal-to-noise ratio (SNR) and, thus, are preferable. The second objective is the compliance of the cFaCES sensor. If the sensor is notably stiffer than the skin, it will significantly affect the skin deformations, potentially diminishing the amplitudes of those deformations. This not only will be uncomfortable for users, but also will make the cFaCES dysfunctional. Detailed results from this work's theoretical models reveal that the thicker the AlN layer, the more the voltage sensitivity and the less the sensor compliance. The cFaCES has enough voltage sensitivity to respond to

facial deformations (~0.5% - 15%) (Fig. S29 - S122) and, at the same time, does not disrupt the facial motions. Although increasing the AlN thickness improves the voltage sensitivity, it does not increase notably the accuracy of the device, since the current dimensions result in high SNR for all cases. Increasing the AlN thickness will, however, make the cFaCES more rigid than the skin and will disrupt facial motion. The current dimensions are thus close to the optimal values for our multi-objective optimization problem.

Our main method for parametric study is FEM, which can handle all the details and complications of the cFaCES sensor, including all layers. We study the effect of the design parameters on 1) the generated voltage (i.e., the sensitivity of the cFaCES) and 2) the stiffness of the cFaCES (i.e., the feel of the sensor).

In the sensitivity analysis, we examine voltage generation of the sensor subjected to a sinusoidal uniaxial facial strain of 1% amplitude. As shown in Fig. S129a, the amplitude of the generated voltage increases with the thickness of the sensing elements and decreases with the thickness of the substrate PDMS layer. This suggests that the thicker the AlN layer, the greater the voltage sensitivity, and the only limitations for the AlN thickness are set by fabrication. This verdict is contradicted, however, by the fact that if the AlN layer is thick, the cFaCES will be too stiff - it will not only feel uncomfortable, but it will also diminish facial gestures (the very thing it should measure).

To analyze the stiffness (and the “feel”) of the sensor, we calculate the axial stiffness from the equation $k = \frac{F_x}{\delta_x}$, where F_x is the force applied to one end of the sensor in X direction and δ_x is the displacement in the X direction. In this analysis, we apply forces at the two ends of the cFaCES and simulate its deformation in COMSOL. We measure the motion of the two end

faces and use it in the aforementioned formula. As shown in Fig. S129b, increasing the AlN thickness increases the overall stiffness of the cFaCES.

The critical stiffness value for the cFaCES is the skin stiffness. We compare the stiffness of the cFaCES to that of the skin. If the stiffness of the sensor is notably larger than the skin stiffness, it will affect the skin motion. The stiffness of the skin is estimated as $k = \frac{EA}{L}$, where *E* is Young's Modulus, *A* is lateral area and *L* is length of skin under the sensor. The skin Young's Modulus is assumed to be *E* ~31 kPa [91] and thickness ~6.39 mm (this corresponds to experimental average values from cheek skin) [92]. The resulting estimated value of the stiffness of the skin is 113 N/m. The current device design with 1.5 μm thick AlN has a stiffness of 166 N/m, which shows that the stiffness of the device is close to the skin stiffness; therefore cFaCES does not fundamentally change the skin stiffness.

The cFaCES piezoelectric elements themselves are much stiffer than the cFaCES substrate material and human skin; therefore, changing the size (lateral area in the X-Y plane) of the piezoelectric elements affects the cFaCES stiffness considerably. The chosen lateral area was determined by evaluating the trade-off between (i) large size diminishing spatial resolution of strain measurement while increasing the stiffness, and (ii) small size resulting in low voltage sensitivity (Fig. S129c). The chosen value of lateral area was ~0.725 cm^2, resulting from a 0.24 cm AlN element radius.

The shape of piezoelectric elements, however, does not affect the cFaCES stiffness as long as lateral area and thickness remain constant, which means a cFaCES with square piezoelectric elements of side length $\sqrt{\pi} * r$ results in the same cFaCES stiffness as a cFaCES with circular piezoelectric elements of radius *r*. We performed two FEM models with the same piezoelectric

lateral area. One has circular patches with ~0.24 cm radius and the other one has rectangular patches with side length of ~0.42 cm. The sensor is pulled with a specific force from one side and the average displacement field of that side in the same direction is measured. As shown in Fig. S129d, both models have the same displacement field distribution, which confirms that sensor stiffness is independent of the shape.

We have further developed an analytical model in order to show the relationship between the output voltage and the amount of shear force exerted to the device. The electric displacement vector *D* can be defined as $D = \frac{Q}{A_p} = d_{31}\sigma_{xx} + \varepsilon E$[93], where *Q* is electric charge, A_p is lateral area of piezoelectric element, ε is the dielectric constant matrix, *E* is the electric field vector, $d_{31}$is the piezoelectric coefficient, and $\sigma_{xx}$is the *xx* component of the stress matrix. Since there is no external voltage applied to the piezoelectric patch, the equation reduces to $D = d_{31}\sigma_{xx}$. Therefore, the electric charge is $Q = d_{31}\sigma_{xx}A_z$, where A_z is the lateral area of the electrode. Furthermore, for a simple beam comprising of a piezo layer and a substrate layer, the tension in the longitudinal direction is given by $F_{xx} = \frac{k_p}{k_p+k_s}F$,where F_{xx} is the force in piezo layer, *F* is the total force applied to the beam, and k_p and k_s are stiffnesses of piezo and substrate, respectively which can be calculated by $k_p = \frac{E_p t_p w}{L}$and $k_s = \frac{E_s t_s w}{L}$[93] (where *p* and *s* subscripts refer to piezo and substrate layers, *E* is Young's Modulus, *t* is the thickness of layer, *w* is the width of the sensor, and *L* is the length). Thus, the tension can be written as $\sigma_{xx} = \frac{k_p}{k_p+k_s}\frac{F}{t_p w}$. Based on this, the electric charge can be rewritten as $Q = d_{31}\, Lw\frac{k_p}{k_p+k_s}\frac{F}{t_p w}$. One can solve for the instantaneous current in the circuit by taking the time derivative of both sides and writing Kirchhoff's law for the current, which yields $I = C\frac{dV}{dt} + \frac{V}{R} = \alpha\dot{f}$, where $\alpha = \frac{d_{31}\, LE_p}{E_p t_p + E_s t_s}$, *C* is the capacitance of the simplified sensor model, *V* is the voltage generated, *R* is the equivalent

resistance, and $\dot{f}$ is the time derivative of the applied force. Furthermore, one can form the transfer function between the voltage as output and force as input and rearrange terms in the following format $\frac{V(s)}{F(s)}=\frac{\alpha s}{Cs+\frac{1}{R}}$. The frequency response function (FRF) of the above transfer function is shown in Figure S128e.

Similarly, for the case of constant strain, one can formulate the electric-charge density as $D = \frac{Q}{A_p}=e_{31}\varepsilon_{xx} + \varepsilon E$, where ***e*** is stress piezoelectric matrix,$\varepsilon_{xx}$is the strain component xx, ε is the dielectric matrix with the coefficients of electric permittivity on its diagonal, and ***E*** is the electric field vector. The external voltage applied is zero and so is the electric field ***E***, thus, $D=e_{31}\varepsilon_{xx}$. Therefore, the electric charge along the electrodes are obtained by $Q=e_{31}\varepsilon_{xx}A_z = e_{31}\varepsilon_{xx}\, Lw$. Taking time derivative of both sides of the equation and using Kirchhoff's Law yields to $C\frac{dV}{dt}+\frac{V}{R}=\beta\varepsilon_{xx}$, where $\beta = e_{31}\, Lw$. Taking the Laplace transform of both sides of the equation and rearranging the terms with respect to voltage leads to $\frac{V(s)}{\varepsilon_{xx}(s)}=\frac{\beta s}{Cs+\frac{1}{R}}$ which describes the transfer function between the voltage and strain for the case where the strain is assumed to remain constant. The FRF of this transfer function can be seen in Fig S128f.

The total force exerted on the device can be obtained using the equivalent stiffness k_{eq}, which relates to the force ***F*** by $F = k_{eq}\,\delta$[94], where δ is the uniaxial displacement. Therefore, the strain can be calculated by $\varepsilon = \frac{\delta}{L}=\frac{F}{k_{eq}\,L}=\frac{F}{w(t_pE_p+t_sE_s)}$. Similarly, the total stress in the device section can be obtained by $\sigma = \frac{F}{(A_p+A_s)} = \frac{F}{(t_p+t_s)w}$. We can define the equivalent modulus of elasticity for the device by $E_{eq} = \frac{\sigma}{\varepsilon}=\frac{t_pE_p+t_sE_s}{t_p+t_s}$[94]. From this equation, it is clear that the equivalent stiffness and elastic modulus of a cFacES are more sensitive to the variation of the piezoelectric layer

thickness compared to that of the substrate, because the elastic modulus of the piezoelectric layer is two orders of magnitude higher than that of the substrate.

From a user experience standpoint, we considered the effect of the size of the entire device. A large device area (i.e. covering nearly the whole face) may be quite uncomfortable for continuous lamination on the skin of ALS patients. Furthermore, a large-area sensor would involve more unnecessary signals, making the real-time decoding much more complex. With such considerations, we felt that a 2.5 cm x 3.5 cm device with a ~1.1 cm x 1.1 cm sensor array, which can cover the areas where dynamic deformations of the skin occur during facial motions (Fig. 5), could provide functionality without diminishing user comfort too greatly.

Finally, the strategy for determining the size and spacing of the sensing elements directly relates to the strain contour maps given in Figure 5. In addition to the voltage generation (Fig. S129c) and stiffness considerations discussed above, we evaluate contour maps generated by 3D-DIC (see “Modeling of cFaCES behavior during facial deformations and implications for device placement”) in order to determine if the radius of the AlN piezoelectric element will be sufficient to capture the dynamic strain deformation patterns occurring on the face during facial motions. Too large of an element would average out, and thus lose, the spatiotemporal dynamics of the facial deformation strains, whereas too small of an element would require too large of an array, making for a high computational load for the real-time decoding classification algorithm. Based on a study of 3D-DIC contour maps, the minimum spacings between strain isolines (each representing a 3% gradation change) for various motions ranges from 0.15 cm to 0.27 cm in the target region of interest for the sensor (Fig. S130). The choice of an element radius of 0.24 cm (and thus diameter of 0.48 cm) would provide an acceptable choice by which ~3% strain gradations can be appropriately deduced by the piezoelectric elements without too much loss of dynamic strain data and without requiring too large of an array of elements. Given

the size of the piezoelectric elements and the desired size of the element array (2x2), it is important to note that the one-time data gathered by 3D-DIC can be used as a method to determine where sensing elements can be located to maximize distinguishability. For our study, we designed the spacing to strike a balance between two factors: (i) to be able to distinguish between local strain deformation patterns, as identified by 3D-DIC contour maps (Fig. 5) and (ii) to have a smaller footprint on the face so that it can be more comfortable and also be made visually invisible with cosmetic products (Movie S1). With such considerations, and given that the spacing has to be at least as large as the piezoelectric element diameter of 0.48 cm, the distance between the centers of adjacent elements was selected to be 0.6 cm.

4.2 Microfabrication process of a cFaCES

The microfabrication of a cFaCES starts from a standard wafer cleaning process on an eight-inch silicon (Si) test wafer (Sumco Corp., Tokyo, Japan). Subsequently, a layer of 50 nm-thick aluminum (Al) was deposited on the surface of the cleaned Si wafer. Using plasma-enhanced chemical vapor deposition (PE-CVD, Oxford Instruments, Bristol, UK), a silicon dioxide layer was grown on the Si wafer with the following precursors: SiH_4 (260 sccm), N_2O (1000 sccm) and N_2 (500 sccm). Molybdenum (Mo) bottom electrode (200 nm-thick) has been deposited onto the soft oxide layer by sputtering technique in the same deposition run, followed by an AlN bulk layer deposition (1.5 µm-thick). Both AlN seed and bulk layers have been deposited using a pure Al target (99.9995%, Vacuum Engineering & Materials Co. Santa Clara, CA, USA) in a mixture of Ar (20 sccm) and N_2 (20 sccm) gases in direct current (DC) pulsed power supply (Sigma Deposition Systems, SPTS Technologies, Newport, UK) at 750 W and with a working pressure of 2.8×10^{-3} mbar. Mo layer has been sputtered using a pure Mo target (99.95%, Vacuum Engineering & Materials Co. Santa Clara, CA, USA) in pure Ar atmosphere (66 sccm) under DC power supply of 400 W and a working pressure of 5×10^{-3} mbar. After the optical lithographic process to pattern AlN and Mo stacked layers, the Mo top layer was sputtered in the

same condition of the Mo bottom electrode layer. The Mo top layer was dry etched by an inductively coupled plasma (ICP)-reactive ion etching (RIE) system (PlasmaPro 100 Cobra ICP etching system, Oxford Instruments, Abingdon, UK) under the same conditions reported for the Mo bottom layer. Eventually, PI2611 polyimide (PI) precursor solution (HD Microsystems, Parlin, NJ USA) was spin coated (PWM50, Headway Research, Inc, Garland, TX USA) at 2000 rpm for 60 s on the Mo top electrode and followed by a curing process at 350 °C for 30 min performed on a VWR® hot plate (VWR International, Radnor, PA USA). Then, a layer of polydimethylsiloxane (PDMS, matrix/crosslink ratio 1:10), Sylgard™ 184 Silicone Elastomer, Electron Microscopy Science) was spin coated (1000 rpm, 60 s) and cured at 60 °C overnight in a curebox (CB-4015, Wicked Engineering, USA) as the final encapsulation layer.

After the micro-fabrication process, the cFaCES was released via an anodization process in a 3% NaCl (Chemical reagent, Sigma Aldrich, St. Louis, MO USA) solution (Fig. S3). The microfabricated chip served as the anode, while a chip coated with a layer of gold acted as the cathode. +2V potential was applied via a direct current power supply (E3631A, Keysight Technologies, Santa Rosa, CA USA) to the anode and cathode. After release, the sensor was placed upside down onto a glass plate and the SiO_2 layer was patterned to expose the bonding pads and form electrical connections using anisotropic conductive film (ACF) cables. Eight identical cFaCESs were used to perform all experimental demonstrations to characterize the device performance and for use *in vivo* tests.

4.3 Biocompatibility testing of the cFaCES

To conduct biocompatibility tests (Fig. S7), Human Epidermal Keratinocytes (Sigma Aldrich, St. Louis, MO, USA) as representative cells were grown in Keratinocyte serum-free growth medium (Sigma Aldrich, St. Louis, MO, USA). The medium was changed every time the cells reached 40

percent confluence at 37 °C, 5% CO_2 and 95% relative humidity. When the keratinocyte culture reached 80 percent confluence, it was prepared for subculture.

To prepare for biocompatibility study, a cFaCES was sectioned into 1 cm^2 coupons to fit into a 24 well glass bottom culture plate (CellVis, Mountain View, CA USA). The coupons were sterilized under ultraviolet (UV) light for 30 min. The control wells and devices were coated with 150 µL of 1 mg/mL fibronectin (Thermo Fisher) for 20 min. Excess fibronectin was removed through aspiration and allowed to dry for an additional 30 min. Human Epidermal Keratinocytes (HEK) were cultured until reaching 75 percent confluence. HEK cells were cultivated for 1, 3, and 9 days at 37 °C, 5% CO_2, 95% of relative humidity. The medium was changed every 48 hr.

To evaluate the biocompatibility of the AlN structures, the viability and cytotoxicity of the keratinocytes was determined after 9 days of cultivation by utilizing two color fluorescence LIVE/DEAD viability (Invitrogen) assay. For LIVE/DEAD assay, the cells were grown on the cFaCES and after 9 days were prepared and stained according to the manufacturer's protocol (Sigma Aldrich, St. Louis, MO, USA). Briefly, the culture medium was aspirated from each of the wells and then rinsed three times with 1x phosphate buffered saline (PBS). A working solution (consisting of 5 mL 1x PBS, 10 µL of 2 mM Ethidium Homodimer I (EthD-I), and 2.5 µL of 4 mM Calcein AM) was added to cover each of the samples. The submerged samples were incubated for 30 min at 37 °C. After the incubation period, the working solution was removed, and the samples were rinsed once with 1 x PBS, then mounted and immediately imaged with the Nikon Ti confocal fluorescent microscope with a 40x Nikon water-immersion (WI) objective (NA = 1.15). For brightfield imaging of cells growing on devices, a 40x WI objective (NA = 1.15) was used without the confocal fluorescent system.

4.4 Preparation of mock skin sample

The process to prepare mock skin was divided into 3 steps: (1) fabricating the skin mould, (2) synthesizing the artificial skin layer, and (3) peeling the artificial skin layer from the skin mould. Firstly, Ecoflex A and B (Body Double™ Silk, Smooth-On, Inc., Macungle, United States) were mixed with 1:1 weight ratio, blended thoroughly for 2 min, and placed on the skin of dorsal area of hand, where it was naturally cured under ambient indoor conditions for 30 min. Afterwards, the cured layer was removed from the hand, and placed in a plastic petri dish (VWR International, Radnor, PA USA) with the textured side up, so that it can serve as a mould. Subsequently, the mixture of Dragon Skin A and B (Dragon Skin 30, Smooth-On, Inc., Macungle, United States) with a weight ratio of 1:1 was blended with 3 wt% silicone pigments (Silc Pig®, Smooth-On, Inc., Macungle, United States) to simulate the skin color, and then poured on the top of the mold made by Ecoflex A and B. Eventually, the artificial skin layer was peeled from the top of the mold after curing for 12 hr at room temperature.

4.5 Lamination process of a cFaCES on the skin

Laminating a cFaCES on the same location of the facial skin over multiple sessions of lamination and delamination is possible using a scaffold (Fig. S1). The subject's face is prepared to be free of lotions, creams, and oils. Then, a low-stretch fabric is held in place over the region of interest on the face upon which the sensor is to be placed. The fabric is fitted over facial features such as the chin and nose. A thin marker is used to outline key features of the face, such as corners of the ear, nose, mouth, and eye, which can be used to re-align the fabric. The fabric is cut along the drawn lines and checked for alignment with facial features. Then, a 3 cm x 5 cm area is outlined and cut out of the fabric. This location is where the cFaCES and Tegaderm® is placed. Two pieces of clear, pressure-sensitive tape are placed on the short sides of the cut-out rectangle to achieve adhesion with Tegaderm® tape. A pressure-sensitive

tape with relatively low adhesion force to the non-sticky side of Tegaderm® tape is preferred. This creates the alignment scaffold. The sensor is then placed on Tegaderm® tape's sticky side and the non-sticky side of Tegaderm® tape is adhered onto the sticky side of the alignment scaffold and prepared for attachment to the face. The alignment scaffold with the cFaCES attached is laminated on the face, starting from one edge and making sure that all previously marked key features are aligned. Subsequent removal of the alignment scaffold leaves behind the cFaCES laminated on the skin in a particular region of interest. Removal of the paper backing on Tegaderm® tape is removed so the sensor can freely follow facial deformations.

4.6 Surface characterisation of a cFaCES

The mass of a cFaCES was determined using an analytical balance (ME-T, Mettler Toledo LLC, Columbus, United States). Low resolution and high resolution optical images of the cFaCES were collected using a single lens reflex camera (EOS 6D, Canon, Tokyo, Japan), and an optical microscope (BX53M, Olympus, Tokyo, Japan), respectively. The cFaCES mounted on the artificial skin was imaged using a scanning electron microscopy (SEM, JSM-5600LV, JEOL, Tokyo, Japan) at low magnification (100 X), while the cross-section morphology of the cFaCES and top-view morphology of the AlN bulk layer were visualized using field emission scanning electron microscopy (FE-SEM, Ultra Plus, Carl Zeiss, Oberkochen, Germany) at high magnification (5000 X) with an acceleration voltage of 10 kV. The colorization process for the SEM image of the cFaCES on skin was based on the color burn function in Adobe Photoshop CC 2018 (Fig. S4). The AlN grain size was calculated from the high resolution SEM images using an image processing software (ImageJ, National Institution of Health, Bethesda, United States). To determine the phase composition of AlN bulky layer and verify the multi-layered structure, the microfabricated cFaCES was examined by an X-ray diffractometer (XRD, SmartLab®, Rigaku, Tokyo, Japan) operating at 40 kV and 30 mA with a Cu-Kα radiation source (Fig. S5). After the θ~2θ scans from 20°~70°, a rocking curve scan was carried out at 2θ

where the (0001) reflection is present, by varying the sample holder angle (ω). The full width at half maximum (FWHM) was measured from the rocking curve to evaluate the AlN crystal orientation. The cross-section scanning transmission electron microscopy (STEM) samples were prepared using a focused ion beam (FIB) milling lift out technique with a FEI Helios microscope (Helios NanoLab^{TM} 660, Field Electron and Ion, Hillsboro, United States) operating at 0.5~30 keV ion beam energy. The cross-section microstructure of the AlN bulk layer was characterised by TEM (ARM 200F, JEOL, Tokyo, Japan) at an accelerating voltage of 200 kV with a point-to-point resolution of 0.2 nm.

4.7 Adhesion strength tests

Standard vertical peel tests were carried out to determine the adhesion strength between test samples (3M Tegaderm® tape + cFaCES), as well as the cFaCES itself and the skin, at room temperature (Fig. S6b). The tests followed a previously established methodology [30]. Tegaderm® tape cut into the same size as the cFaCES (3.5 × 2.0 cm^2) was used as the control in the test. In both tests, the measurement location was the skin on the back of hand, cleaned with a pad soaked in ethanol. Samples with fixed area (3.5 × 2.0 cm^2) were placed on the inner surface of the left forearm, where they were cleaned with a pad soaked in 70% ethanol solution (≥96% (v/v), EMSURE®, MilliporeSigma). A corner of the sample was attached to the tip of the micro-universal testing system (MicroTester 5948, Instron, Norwood, United States) at 90°. The tip moved in an upward direction to peel samples off from skin at a speed of 10 mm/sec. The reported adhesion strength was divided by the entire cFaCES area, corresponding to the maximum force value recorded just before the complete removal of samples from the skin.

4.8 Mechanical characterization of the cFaCES

The mechanical performance of the cFaCES was investigated in terms of cyclic compression, bending and stretching tests using a micro-universal testing system (MicroTester 5948, Instron, Norwood, United States) equipped with a 50 N load cell exhibiting the force resolution of 2 mN. During the mechanical tests, the cFaCES was electrically connected with a data acquisition (DAQ) system with PXIe-1071, PXIe-8821 and PXIe-4464 components (National Instruments, Austin, TX, United States). The electrical output from the cFaCES was recorded in real time with application of a 6^{th} order Butterworth filter. Electrical data was recorded with NI SignalExpress 2015 and mechanical data was recorded in BlueHill software. Cycles of compression (200x), bending (50x) and stretching (20x) were conducted for each type of testing, respectively.

For the compressive test, the cFaCES devices were deformed under three different conditions, i.e. bare sensor on a glass plate; sensor on mock skin; sensor on mock skin with the coverage of Tegaderm® tape. The compressive test for the last group is to simulate the condition of wearing the sensor on human body with Tegaderm® tape. A small glass plate (15.75 mm × 16.20 mm, Fisherbrand®, Fisher Scientific International, Inc., Hampton, NH USA) was placed on the top surface of sensors, entirely covering all sensing elements. The size of the glass plate and mock skins to carry the sensors is the same (2.5 cm × 5.0 cm). The compressive load was applied in the range of 0 ~ 120 kPa and 0 ~ 40 kPa for sensors on the bare sensor and sensor on mock skin, respectively.

The bending test was carried out for bare sensors and sensors on mock skin under a frequency of 0.5 Hz. For bare sensors, Instron tips vertically clipped the top and bottom of the sensor to expose a testing length of 1.42 cm. For sensors on mock skin, two terminals of the mock skin substrate are fixed to leave a testing length of 5.4 cm. To prevent the sensor delamination from mock skin during test, Tegaderm® tape was covered on the top surface of the sensor. The

bending line was located in the middle of two rows of sensing elements. For sensors on mock skin, the bending distance that the upper tip goes down was varied from 1 mm to 10 mm with an interval of 1 mm between each test. The corresponding bending radii were determined by fitting the sensor profile from optical images. In the case of bare sensors, the bending distance was set from 2 mm to 8 mm with an interval of 2 mm.

Following the bending test, the stretching test was performed for bare sensors and sensors on mock skin as well. Similarly, a layer of Tegaderm® tape was laminated on the top of the sensor to prevent relative motion between the sensor and the mock skin substrate. The testing dimension of samples are the same as those in the bending test, i.e. the testing length of samples is 1.42 cm and 5.40 cm for bare sensors and for sensors on mock skin, respectively. The stretching distance that the Instron tip moves upward ranged from 0.35 mm to 3.5 mm for sensors on mock skin, and from 0.0025 mm to 0.3 mm for bare sensors.

Additional calculations demonstrate that the concave and convex buckling cases of the bare sensor would theoretically result in the same voltage waveform output. Essentially, the theoretical model used for buckling is not sensitive to directionality (concave or convex), since the direction of the buckling only depends on the small transversal perturbation displacement, which can be in-plane (convex) or out-of-plane (concave). Theoretically and without using a rectification circuit, one can determine whether the buckling is convex or concave by tracking the polarity of the output voltage. In order to show that the convex buckling is identical in all modeling aspects to concave buckling, one can consider the relationship between the strain ε and radius of curvature $\frac{z}{\rho}=\varepsilon$, where *z* is the distance of a given point from the neutral axis and ρ is the radius of curvature (ROC). This leads to the following relationship between the moment *M* and ROC: $\frac{1}{\rho}=\frac{M}{EI}$[94,95], where *E* is the Young's modulus and *I* is the area moment of inertia. It

can be seen from the above equations and the mentioned references that the governing equations of motion are symmetric in the buckling directions. The order of layers gets encapsulated in the equivalent *EI* term and the stiffness of the sensor in convex and concave deformations are identical; so is the density of the system in the two deformations. The convex and concave buckling solely depend on the initial conditions and are of no consequence to the magnitude of the generated voltage.

Lamination of the cFaCES on skin, however, means that the same deformation magnitudes of convex and concave buckling cannot occur, which results in distinguishability. The mechanical testing is performed on the mock skin with the purpose of simulating the *in vivo* trials on skin. High-magnitude concave buckling is not possible when a cFACES is laminated on the face, since the bottom of the device is stuck to facial skin, and facial skin does not undergo high-amplitude concave buckling during any natural facial deformations. It is true that during certain motions, such as pursed lips (PL), the cheek skin may pucker inward due to stretching of skin over an internal mouth cavity. For such cases, Fig. 2e strain maps demonstrate that during stretching on mock skin there occurs some low-amplitude concave buckling (note the out of plane deformation in the negative Z direction), and shows that the waveform resulting from such stretching/concave buckling is different from the convex buckling, i.e. Fig. 2d. Since these two cases result in different voltage waveforms, as seen in Fig. 2d and 2e experimental and bimodal theoretical (analytical and FEM) voltage waveforms, the decoding algorithm based on KNN-DTW can distinguish between the two cases (Fig. 6b and 6c).

4.9 Finite element modeling

To model the sensor in different configuration using finite element analysis, we use COMSOL multiphysics modeling software. This allows us to model the multi-layer sensor in full details. We use Solid Mechanics, Electrostatics, and Electrical Circuits modules in COMSOL Multiphysics®

Version 5.4. The Solid Mechanics module allows the inclusion of piezoelectric effects in the model. The dynamic equation of motion is $\rho\frac{\partial^2\vec{u}}{\partial t^2} = \nabla\cdot\bar{\bar{S}} + \bar{\bar{F}}$, where $\vec{u}$ is the deformation vector, $\bar{\bar{S}}$ is the stress tensor, and $\bar{\bar{F}}$ is the piezoelectric coupling coefficient tensor. The stress is related to the strain tensor through the constitutive equation for linear elastic material, $\bar{\bar{S}} = \bar{\bar{E}}\bar{\bar{\epsilon}}$, where $\bar{\bar{E}}$ is the elastic modulus tensor and $\bar{\bar{\epsilon}} = \frac{1}{2}(\nabla u + \nabla u^T)$. The electrical displacement, $\vec{D}$, is related to the electric field $\vec{E}$ and strain as $\vec{D} = e\bar{\bar{\epsilon}} + \epsilon_0\epsilon_{rs}\vec{E}$, where the electrical permittivity is equal to $\epsilon_0\epsilon_{rs}$. The model necessarily includes external electrical elements, including the equivalent resistance ($1M\Omega$) and capacitance ($265\ pF$) of the DAQ, as shown in Fig. 2c, since the current draw from the DAQ affects the shape and magnitude of observed voltages at the output of the cFaCES. One of the key parameters affecting the results of the finite element model is damping, for which the isotropic damping assumption resulted in a good match between experimental and finite element analysis. The damping loss factor η is directly related to the damping ratio $\eta = 2\zeta$ used in the analytic models, which ensured both analytical and finite element models use the same modeling parameters. The 3D geometry of sensor consists of thin layers with high aspect ratio. Swept meshing which is specifically designed for ultra-thin geometries is used in the model. This is a geometry discretization technique that effectively creates far less hexahedral or prismatic mesh elements for disproportionate dimension sizes. The technique is a good compromise between accuracy and computational efficiency as other meshing techniques create an overabundance of elements for a thin geometry.

4.10 Analytical modeling

During the characterization tests, the cFaCES performs two fundamentally distinct motions: The first is the buckling motion, which is the dominant form of deformation in bending tests. Buckling motion is also observed in the stretching tests due to the specific configuration of the stretch tests. During the stretch tests the specimen slides out of the clamp jaws in the first cycle of

stretching. This results in buckling of the specimen in the next cycles. The second type of motion is uniaxial deformation observed in compression tests. We model each of these two fundamental motions separately as the motion in each type is inherently different from the other. The buckling and stretching model has been outlined in the Results and Discussion section. The model for compression is discussed in Note S4.

The key point in the analytical model is that the small AlN patches are part of the larger rectangular sensor. The model does not isolate the AlN circles but models the entire rectangular sensor considering the effects of the AlN patches. We have assumed an Euler-Bernoulli beam assumption, i.e., we have assumed: i) the cross-section is infinitely rigid in its own plane, ii) the cross-section of a beam remains plane after deformation, and iii) the cross-section remains normal to the deformed axis of the beam. Experimental measurements show that Euler-Bernoulli assumptions are valid for long, slender beams made of isotropic materials with solid cross-sections [96]. Euler-Bernoulli beam theory is applicable to the problems in which the length-to-thickness ratio is at least 10 [97,98]. In this study, the length of the cFaCES is 3.5 cm and its overall thickness is less than 50 μm, which implies that the ratio is about 700, and that the Euler-Bernoulli theory can be used to model the cFaCES. The challenging part in our model is the fact that the width to length ratio of our model is less than 10. This does not match the assumption that the structure is “long”. Although, generally speaking, this requires a plate model for the sensor, the forcing conditions make beam models sufficiently accurate. The clamping conditions in all characterization tests make application of loads completely symmetric along the width. The clamps also prevent application of any torsional loads to the sensor. As a result, although the natural frequencies of the transverse modes are larger but comparable to those of the beam modes, they are never excited; therefore, it is unnecessary to include them in this model [99,100]. All factors combined, beam theory is applicable to the theoretical model of the cFaCES in the loading conditions which it experiences.

4.11 Temperature stability test of a cFaCES

The temperature stability of the cFaCES was evaluated using a thermometer (51-2, Fluke, Everett, WA) at different temperatures ranging from 20 °C to 60 °C (Fig. S6c). The cFaCES was mounted on a glass plate (Fisher Scientific, 12-550-A3, 25 x 25 x 1 mm) which was placed on the top surface of a hot plate (HS40A, EchoTherm^{TM}, Carlsbad, CA). To monitor the sensor temperature during the test, there is intimate contact between the probe of the thermometer and the surface of AlN sensing element. Sensor temperature was regulated to a series of pre-set temperature points by tuning the temperature of the hot plate. At each temperature point, electrical output from the cFaCES was recorded by a DAQ system with PXIe-1071, PXIe-8821 and PXIe-4464 components (National Instruments, Austin, TX, United States).

4.12 Facial motion strain field measurements with DIC

A 3D-DIC setup (Fig. S9a, S9b) was created using 6 Blackfly GiGE 1.3 MP cameras (Point Grey Research Inc., Richmond, BC, Canada) equipped with Computar (A4Z2812CS-MPIR, 2.8mm-10mm, 1/2.7") adjustable lenses (Point Grey Research Inc., Richmond, BC, Canada). The cameras were placed in a circular array around a single focal point in which the subject could place their head during image acquisition. The cameras were placed along a circular arc (32 cm diameter) spanning 160 degrees, with each camera 32 degrees away from its adjacent, allowing for full facial view within images. In order to power and take images simultaneously from all cameras, each camera was connected via ethernet to an 8-port network switch (PoE Netgear) as well as an adapter (Point Grey Intel Pro GigE host adapter), which allowed for connection to a computer with a PCIex1 slot. To enable uniform lighting and higher contrast images, three 2-foot LED strips (HitLights, Baton Rouge, LA, United States), each providing 384 Lumens per foot were placed on top of the cameras facing the subject, and 5800K COB (chip-on-board) Halo lights (Super Bright LEDs, St. Louis, MO, United States) were placed around the lens of

each camera. All lights were connected to a single breadboard, and supplied power from one of two 12-volt, 2-amp power supplies plugged directly into wall outlets. The 3D-DIC setup was built with enough spatial resolution (1.2 MP, 12-bit) to capture the ~1.5 mm dot sizes and their random spacings and with enough temporal resolution (6 fps) that it can capture the natural facial deformations with no blurring in the regions of interest.

Custom code was written to enable image acquisition from the DIC setup to take photos simultaneously at 6 frames per second (fps) during each motion. The delay between the first camera and the last camera image for each timestep is ~2 ms. This command line-based script in Python 3.6 acquired and saved images from a setup of multiple Point Grey Blackfly GigE cameras. The script utilized FLIR's Spinnaker SDK and PySpin Python library to interface with the cameras. The user can choose from three different modes of image acquisition: manual, timed and continuous. After image acquisition is completed, all images are rotated 270 degrees to correct the camera orientation and saved under the PNG file format. All images were taken in grayscale, and image naming followed the requirements specified for use with MultiDIC [40].

For image collection, the subject's skin surface of interest (either temple or cheek) was first cleaned with water and dried with paper towels. The skin was then painted with non-toxic, water-based, white liquid makeup (Mehron Inc., Chestnut Ridge, NY, United States), which was applied in a thin layer with a paintbrush (Zhu Ting, China) to provide a high-contrast background. A speckled dot pattern was applied on top of the dried background layer by airbrushing non-toxic, water-based, black liquid makeup (Mehron Inc., Chestnut Ridge, NY, United States) through a stencil using a Master Airbush system (TCP Global, San Diego, CA, United States). All the material components (i.e., ingredients) of the non-toxic liquid face makeup used are FDA approved and therefore biocompatible. The name of the ingredients are as following: Water/Aqua/Eau, Propylene Glycol, Magnesium Aluminum Silicate,

Glycerin,Cellulose Gum, Bis-PEG-15 Dimethicone/IPDI Copolymer, Triethanolamine, Talc, Disodium EDTA, Phenoxyethanol, Iodopropynyl Butylcarbamate. May Contain: [+/- CI 77891 (Titanium Dioxide), CI 77007 (Ultramarines), CI 77491, CI 77492, CI 77499 (Iron Oxides), CI 77288 (Chromium Oxide Greens), CI 15850 (Red 7 Lake),CI 15850 (Red 6 Lake), CI 19140 (Yellow 5 Lake)]. Since this liquid makeup is water-based, it is easily washable. The stencil was generated by custom code, written in Python 3.6, to produce a random non-overlapping speckle pattern (1.5 mm dot size, 50% fill). The speckle pattern was laser cut into a 1/16" (1.6 mm) thick, 10x11 cm wide rubber sheets in a 120W CO_2 laser cutter (Universal Laser Systems, Scottsdale, AZ, United States). After painting the facial skin, the subject placed their head within view of all cameras, and cameras were adjusted to the proper iris (light intake) and focal length (zoom) settings to allow for capture of clear images. The subject then removed their head from view of the cameras while images of a distortion correction object (flat checkerboard, 13 x 20 square grid, 11.4 mm edge length of each square, Fig. S9c) and a stereo calibration object (10 cm diameter cylindrical object, with ordered pattern of 3 mm square dots with 10 mm spacing, Fig. S9d) were acquired using adjusted camera settings. This step allowed for characterization of calibration errors (0.1 mm root-mean-squared (RMSE) error) (Fig. S10, S11). Null strain tests serve as a control and establish that errors from the entire 3D-DIC data collection process are at least one order of magnitude lower than the strains measured from almost all facial deformations (Fig. S12). Images from three cameras were then acquired of the subject's face as they were instructed to perform different facial motions.

After image collection, all images were edited in Adobe Photoshop CC 2019 in order to increase the contrast and clarity of the speckle pattern on the face. First, tonal range and color balance was adjusted using the "Levels" adjustment (grayscale bits 70 to 255 were kept, with gamma level of 0.7). Then, a "Despeckle" filter was applied as a low pass filter to decrease the noise in the image.

All resultant images were processed using DIC methodology to create 3D models of the face from 2D images. A MATLAB-based open-source software, MultiDIC [40], was used for DIC processing and skin strain calculations. MultiDIC processing consisted of the following steps: 1) distortion correction (for determination of each camera's radial and tangential distortion, skew, and focal length parameters), 2) stereo calibration (for determination of reconstruction of 3D point locations from 2D images of those points), 3) 2D-DIC (analysis of speckle images to determine spatiotemporal correlation coefficients and point cloud), 4) 3D-DIC (reconstruction of 3D points and surfaces), and 5) post processing (determination of surface strains and rigid body motions).

Custom-written MATLAB scripts were implemented to interface with MultiDIC to extract local spatiotemporal strain values and correlation coefficients from the region of the face over which the sensor was placed. After selecting a point on a 3D strain map from MultiDIC's step 4 results and saving the coordinates as a variable, one such script can then plot the calculated values for all faces within a specified radius of this point and with a correlation coefficient below the specified maximum (0.3 for all trials reported in this study). All figure graphs related to spatiotemporal strain data were created by running this script on a point selected in the center of the area of one of the cFaCES sensing elements. Using the resultant strain graphs for 16 different motions (11 at the cheek, 5 at the temple), two regions of interest (one on the cheek, one on the temple) were identified for placement of the cFaCES on the face. Strain values were also used to cross-validate sensor functionality and estimate the contribution of the surface strain to the sensor's voltage output. All code can be made available upon request. This procedure was repeated at the temple and cheek of two healthy patients and an ALS patient.

4.13 Facial motion capture with the cFaCES

In order to measure the voltage output of the cFaCES during different facial motions, the sensor was placed on the temple or the cheek of the subject in a location which showed moderate strain values during all the motions, based on DIC trials conducted on that subject. The sensor was not placed in areas of large deformation, such as the corner of the lips or corner of the eye, due to higher likelihood of sensor breakage and/or impediment to normal facial motions. For the temple, this was below the eyebrow and halfway to the hairline. For the cheek, this was in the middle of the cheek directly under the outer edge of the eye and in line with the bottom of the nose. The sensor was fixed to the face using 3M Tegaderm® tape and contact of the back of the sensor with the skin was achieved by applying a thin layer of DI water to the back of the sensor before lamination. The sensor was connected via an anisotropic conductive film (ACF) cable, printed circuit board, and 22 awg wire to a DAQ (NI PXIe-4464 in PXIe-1071 chassis) with input impedance 1 MΩ || 265 pF. The DAQ system was set up with a software filter to remove 60 Hz noise and data were recorded and saved as text files.

4.14 Real time detection and classification of facial motions

For demonstration of real-time detection and classification of facial motions, the sensor voltage was fed into a custom-designed circuit (Fig. S126) for amplification, filtering, and analog-to-digital conversion. The 10-bit digital signal was sent to a Raspberry Pi 3 B+. Custom Python 3.6 code was written to read the stream of data from the sensor and classify detected motions to their appropriate label. The classification model is a k-nearest neighbors dynamic time warping (KNN-DTW) algorithm, utilizing the Python fastdtw library [62]. Label assignment and model setup (setting number of nearest neighbors, warping radius, etc.) and training were performed once per subject before real-time decoding was conducted.

4.15 Ethics Oversight

All procedures in the healthy and ALS subject tests were in accordance with the experimental protocol approved by the Committee on the Use of Humans as Experimental Subjects of the Massachusetts Institute of Technology (COUHES # 1809531633). The participants gave informed consent.

4.15 Code availability

Code used for addressing and capturing images from the cameras for 3D-DIC was written in Python 3.6 and is available at https://github.com/ConformableDecoders/PT-Grey-Image-Acquisition. Code used for 3D-DIC analysis was written in MATLAB is available at https://github.com/MultiDIC/MultiDIC. Code used for real-time decoding of facial deformations was written in Python 3.6 and is available at https://github.com/ConformableDecoders/cFaCES_RTD.

Chapter 5: Outlook and Conclusions

The concepts, materials, system design and characterization methods introduced here offer new routes for rapid, *in vivo* biokinematic assessment of epidermal surfaces during dynamic movements. The conformable nature of the sensors, together with their predictable responses, consistent with theoretical models, offer high-performance operation that is cross-validated with 3D digital image correlation studies. Non-contact, full-field optical strain assessment methodologies coupled with theoretical models have wide applicability for design, placement, and cross-validation of a host of conformable on-body sensors [27,28], even when they are laminated on highly curvilinear regions of the body. Particularly, 3D-DIC studies coupled with detailed 3D multiphysics simulations and analytical calculations, have the potential to characterize *in vivo* strain sensing via modalities other than piezoelectric elements and even inform mechanically-adaptive device design. *In vivo* real-time decoding trials of facial motions to evaluate the proposed, fully characterized device for use as a nonverbal communication interface demonstrate that increasing the number of sensing elements used in classification leading to increased testing accuracies. Current limitations of the cFaCES system are as follows: (i) low density of sensing elements, (ii) small area coverage, (iii) wired connections, and (iv) external adhesion mechanism (Tegaderm® tape). Specifically, low spatial resolution and small area coverage of the sensing elements, although ensure low computational load, nevertheless limit the ultimate distinguishability of a large set of distinct facial motions ($n > 8$). Future embodiments might incorporate high-density, further miniaturized arrays of sensing elements to increase spatial coverage, and thus improve language classification accuracy across a wide variety of motions, which could greatly increase the library size of facial motions. Scaling the spatial density of strain measurements attainable by the cFaCES from its present form (2x2) to a larger configuration (NxN) would necessitate careful routing of a larger number of interconnects, further streamlined fabrication flow, and improvements in the signal processing

circuitry (i.e., by implementing multiplexing). Since our system serves to project the capabilities of a first-prototype low cost, computationally light, conformable nonverbal communication technology, wireless data or power transmission components were not pursued in this study. Such systems, however, may be developed to co-integrate with wireless communication for continuous clinical monitoring of a wide range of neuromuscular conditions, where variations of strain values measured by cFaCES are anticipated due either to time-dependent alterations in muscle movements, and thus measurable epidermal deformations, due to neurodegeneration or a response throughout medical therapy.

Finally, although this work utilizes a static 3D-DIC system to capture epidermal deformations on fairly static regions of the body, such as the face, it would be illuminating to track the epidermal deformations on very dynamic regions of the body, such as the arms and legs and joints thereof, during naturally occurring human movements, such as walking or running. Therefore, the development of conformable sensors for such bodily regions would benefit from a dynamic 3D-DIC instrument that (i) can study naturally occurring, rapid soft tissue movements with cameras housed on a custom-built, moving gantry which automatically tracks and follows the movement of any targeted human body region, (ii) incorporates cameras with high resolution, frame rate, and shutter speed, as well as low-distortion lenses, and (iii) has a custom, hard-wired mechanism to capture and save images that can be remotely triggered to operate 10+ cameras simultaneously and wirelessly.

Appendix A: Supplementary Notes

A.1 Note S1: Photogrammetry (PG) and Three-Dimensional Digital Image Correlation (3D-DIC) governing equations

A.1.1 S1a. DIC system characterization: calibration and distortion correction

System calibration (using direct linear transformation, or DLT) and distortion correction (using bundle adjustment, or BA) were undertaken to characterize the system and determine appropriate camera parameters as needed for further steps.

In DLT, the image point coordinates $I(x_p, y_p)$ are mapped to the 3D positions of the dots on the cylindrical calibration object $s(X, Y, Z)$, which are known with high accuracy, via a set of DLT parameters ($L_{j=1,2,...,11}$), as shown in equation (S1).

$$x_p = \frac{L_1X+L_2Y+L_3Z+L_4}{L_9X+L_{10}Y+L_{11}Z+1}$$

$$y_p = \frac{L_5X+L_6Y+L_7Z+L_8}{L_9X+L_{10}Y+L_{11}Z+1} \quad \text{(S1)}$$

In BA, nonlinear lens distortion correction replaces idealized image point coordinates (x, y) with distorted normalized coordinates (x_d, y_d) through a set of radial (k_1, k_2, k_3) and tangential (p_1, p_2, p_3) distortion parameters, as shown in equation (S2).

$$\begin{bmatrix} x_d \\ y_d \end{bmatrix} = (1 + k_1r^2 + k_2r^4 + k_3r^6) \begin{bmatrix} x \\ y \end{bmatrix} + \begin{bmatrix} 2p_1xy + p_2(r^2 + 2x^2) \\ p_1(r^2 + 2y^2) + 2p_2xy \end{bmatrix} \quad \text{(S2)}$$

where $r^2 = x^2 + y^2$. These parameters are determined through analysis of images of the distortion calibration flat checkerboard object taken with the DIC setup. Further details for the stereo calibration and distortion correction processes can be found in the MultiDIC [40] paper.

A.1.2 S1b. Correlation

Calculation of the matching between images from two adjacent cameras and across two images taken at different times is crucial for achieving accurate full-field strain calculations from 3D reconstructed points. The 2D DIC methods involved in calculating correlation coefficients, therefore, must precede 3D reconstruction. 2D DIC as computed using open source MATLAB software NCorr matches corresponding points on stereo images of the speckled object and is repeated for every stereo pair at every time step. Ncorr implements a first order shape function to describe pixel subset transformations across two images. It further defines the least-square correlation criterion as a correlation cost function, uses the Inverse Compositional Gauss-Newton method as a nonlinear optimizer [101], and uses the Reliability-guided method [102] to propagate the analysis over the region of interest (ROI), the common area viewable from both cameras in a stereo pair, starting from user-defined seed points. In MultiDIC's wrapper for Ncorr, a triangular mesh is defined on the point grid and used for the 3D reconstruction step. Further details for the 2D DIC process can be found in MultiDIC [40] and NCorr [42] papers.

A.1.3 S1c. 3D Reconstruction

At each timestep, 3D reconstruction uses the DLT parameters $L_j^{C_k}$ and $L_j^{C_l}, j = 0, 1, 2, 11$ associated with cameras C_k and C_l in a stereo pair to reconstruct each pair of corresponding, or matching, points $(x_p^{C_k}, y_p^{C_k})$ and $(x_p^{C_l}, y_p^{C_l})$ from the two cameras, as determined by the 2D DIC in the prior step, to 3D coordinates (X, Y, Z), with $\vec{U} = \mathbf{A}\vec{P}$, where

$$\vec{U} = \begin{bmatrix} x_p^{C_k} - L_4^{C_k} \\ y_p^{C_k} - L_8^{C_k} \\ x_p^{C_l} - L_4^{C_l} \\ y_p^{C_l} - L_8^{C_l} \end{bmatrix}, \quad \vec{P} = \begin{bmatrix} X \\ Y \\ Z \end{bmatrix}, \text{ and}$$

$$\mathbf{A} = \begin{bmatrix} L_1^{C_k} - L_9^{C_k} x_p^{C_k} & L_2^{C_k} - L_10^{C_k} x_p^{C_k} & L_3^{C_k} - L_11^{C_k} x_p^{C_k} \\ L_5^{C_k} - L_9^{C_k} y_p^{C_k} & L_6^{C_k} - L_10^{C_k} y_p^{C_k} & L_7^{C_k} - L_11^{C_k} y_p^{C_k} \\ L_1^{C_l} - L_9^{C_l} x_p^{C_l} & L_2^{C_l} - L_10^{C_l} x_p^{C_l} & L_3^{C_l} - L_11^{C_l} x_p^{C_l} \\ L_5^{C_l} - L_9^{C_l} y_p^{C_l} & L_6^{C_l} - L_10^{C_l} y_p^{C_l} & L_7^{C_l} - L_11^{C_l} y_p^{C_l} \end{bmatrix}. \quad \text{(S3)}$$

The 3D coordinate $\vec{P}$ is then determined as the least squares solution $\vec{P} = [\mathbf{A}^T\mathbf{A}]^{-1}\mathbf{A}^T\vec{U}$. Repeating this procedure for all stereo pair images for all timesteps results in 3D point clouds, which form surfaces and capture the motion of points on the object over time. The MultiDIC process includes an option for stitching surfaces calculated from adjacent stereo pairs, but that option was not pursued in this study. Further details for the 3D reconstruction process can be found in the MultiDIC [40] paper.

A.1.4 S1d. Strain calculation

The 3D coordinates calculated in the previous step define the vertices of a triangular mesh surface. The triangular mesh defined at time $t = 0$ is set as the reference configuration, and the meshes at each subsequent timestep are the deformed configurations. As such, strain is assumed to be zero at time $t = 0$ and the triangular mesh coordinates at each time point are to derive the full-field displacement, deformation, and strain. For each triangular element and for each configuration, the deformation gradient tensor $\mathbf{F}$ is calculated using a variation of the triangular Cosserat point element method [44,45]. Assuming each element is characterized by a homogeneous deformation field, this method obtains the finite (nonlinear) deformation field with the same spatial resolution as the DIC measurement, and independently from adjacent data points and numerical derivatives. From the calculated strains and deformations, this work reports the Green-Lagrangian strains. The Green-Lagrangian strain tensor $\mathbf{E}$ is defined as $\mathbf{E} = \frac{1}{2}(\mathbf{C} - \mathbf{I})$, where $\mathbf{C} = \mathbf{F}^T\mathbf{F}$. Further details for strain calculations can be found in the MultiDIC [40] paper.

A2. Note S2: Calculation of neutral mechanical plane of the cFaCES

The neutral mechanical plane can be calculated using the following equation:

$$y_{neutral} = \frac{\sum_{i=1}^{n} \bar{E}_i t_i (2\sum_{j=1}^{i} t_j - t_i)}{2\sum_{i=1}^{n} \bar{E}_i t_i} \quad \text{(S4)},$$

where $\bar{E}_i$ and t_i are the plane-strain modulus and thickness of the i^{th} layer, respectively, and $\bar{E}_i = \frac{E_i}{(1-\nu^2)}$, where E_i is the Young's modulus and υ_i is the Poisson ratio of the i^{th} layer. Given the maximum allowable strain of the piezoelectric element in cFaCES (~0.09%[46] for wurtzite-phase AlN), the minimum radius of curvature that can be experienced by a cFaCES is determined. The relation between radius of curvature and strain is $\frac{z}{\rho} \leq \varepsilon_{allowable}$ where z =$\frac{t_p}{2}$ is the distance from location of the neutral mechanical plane to top of piezo surface, ρ is the radius of curvature (ROC), and $\varepsilon_{allowable}$ is the allowable strain. For maximum strain of 0.09%, the minimum allowable ROC is $\rho \geq 834\ \mu m$ which shows the device can operate on the nose. Concave areas like the nose have larger mean curvature while flatter areas such as cheek and forehead have mean curvature close to zero [97,103,104].

A.3 Note S3: Theoretical modeling of cFaCES mechanical behavior, model for axial displacements

The governing differential equations in equation (1) are valid when the axial load is controlled or known; however, in some of the tests, the axial deformation is controlled instead, for which the following governing equation is used:

$$m\frac{\partial^2 w}{\partial t^2} + c\frac{\partial w}{\partial t} + EI\frac{\partial^4 w}{\partial x^4} + [\frac{EA}{L}\Delta + P_c - \frac{EA}{2L}\int_0^L \frac{\partial w}{\partial x}dx]\frac{\partial^2 w}{\partial x^2} + \alpha[\frac{d\delta(x)}{dx} - \frac{d\delta(x-L)}{dx}]V(t) = 0 \quad \text{(S5)},$$

where the critical load is denoted by P_c. Equation (S5) can also be discretized using the assumed mode method, and the governing equation for the system becomes

$$\begin{cases} M\ddot{T} + c\dot{T} + (K - p_e)T + NT^3 + \beta V(t) = 0 \\ C_0\dot{V} + \frac{V}{R} = -\beta\dot{T} \end{cases} \quad \text{(S6)},$$

where the equivalent compressive force $p_e = A(\frac{EA}{L}\Delta + P_c)^2\frac{\pi^2}{2L}$.

A.4 Note S4: Theoretical modeling of the cFaCES mechanical behavior, buckling of bare sensor

Verifying the theoretical model for subjecting the bare sensors to buckling axial loads is challenging since the amplitude of axial deformations and axial loads are less than the minimum ratings of the testing system. The measured values for the applied load and deformation versus time are noisy. The results from the analytical model matches the average values of the experimental measurement, i.e. removing the noise from the experimental measurements results in a similar response to the analytical model predictions. This suggests the accuracy of the analytical models. The results from FEM follow the general trend of the experimental results. The significant level of variations of the axial force causes the FEM code to become unstable when attempting to refine the temporal resolution. The strain distributions calculated by the FEM for the buckling of the bare sensor are depicted in Fig. S14a, and that for stretching of the bare sensor, which are similarly modeled, as described in the Results and Discussion section, are depicted in Fig. S14b.

A.5 Note S5: Theoretical modeling of the cFaCES mechanical behavior, compression

During the compression tests, the cFaCES is loaded along the thickness direction. The multi-layered sensor can be modeled with the layers acting like different springs in series, as shown

in Fig. S16. The force at the two sides of the device is controlled by the Instron material testing system (one end is clamped and force is applied in the thickness direction). The frequency of longitudinal vibrations along the thickness direction is in the range of a few hertz, while the natural frequency of a cFaCES in the thickness direction is on the order of kilohertz. The excitation frequency of the compression tests is thus significantly lower than the natural frequency of the sensor in the thickness direction. We therefore assume a quasi-static force distribution in the cFaCES, which means that the force applied on all layers are the same. We use this force as the input in our piezoelectric models. The governing equations for a piezoelectric disk vibrating in the thickness direction can be approximated, therefore, by assuming that the first mode is the only active vibration mode. The unimodal mechanical and electrical equations of motion are [105]:

$$\frac{d^2u}{dt^2} + 2\zeta\omega_n\frac{du}{dt} + \omega_n^2 u - d_{33}\omega_n^2 V = \frac{F}{m_{eq}}$$

$$C\frac{dV}{dt} + \frac{V}{R} + m_{eq}d_{33}\omega_n^2\frac{du}{dt} = 0 \quad \text{(S7)},$$

where u is the deformation of the disk, ζ is the damping ratio, ω_n is the natural frequency of the first mode, d_{33} is the piezoelectric coefficient, V is the voltage, m_{eq} is the equivalent modal mass for the first mode, and F is the external force. The capacitance of the piezoelectric layer is *C* and the shunt resistance (the internal resistance of the DAQ) is *R*. The above equations can be simplified one step further by neglecting the inertial and damping terms in comparison to the stiffness term. In the frequency domain, the mechanical equation of motion becomes:

$$-\omega^2 u(\omega) + 2j\zeta\omega_n u(\omega) + \omega_n^2 U(\omega) - d_{33}\omega_n^2 V(\omega) = \frac{F(\omega)}{m_{eq}} \quad \text{(S8)}.$$

When the excitation frequency ω is small, the first (inertial) and second (damping) terms will be negligible compared to the other terms and can be ignored. This simplifies the governing equations to:

$$\begin{cases} u - d_{33}V = \frac{F}{k_{eq}} \\ C\frac{dV}{dt} + \frac{V}{R} + k_{eq}d_{33}\frac{du}{dt} = 0 \end{cases}$$

(S9),

where k_{eq} is the equivalent stiffness of the first mode and is equal to $\omega_n^2 m_{eq}$. The simplified equations are numerically integrated in time to identify the response of the piezoelectric sensor to the compressive excitation in the thickness direction. Comparison of the model predictions and experimental results confirms the accuracy of this assumption.

Compression tests involve compressing the specimen through the thickness direction and measuring the voltage output of one cFaCES piezoelectric element. The tests are designed to measure the d_{33} coefficient in the piezoelectric layer. Compression tests were conducted for bare sensors, sensors mounted on mock skin, and sensors mounted on mock skin and held in place by Tegaderm® tape. The results of the finite element model and analytical model predictions for compression testing have been illustrated in Fig. S15.

A.5.1 S5a. Bare sensor

There is a close match between the experimental results and theoretical model predictions for compression of a bare cFaCES. The small differences are attributed to the noise level and minimum sensitivity of the load sensor. The reversal of motion at the end of each deformation cycle creates small spikes in the experimental results, and correspond to the moment when the compressive force vanishes. These spikes are not captured by either analytical or FEMs. The voltage in piezoelectric sensors is proportional to deformation velocity, which means that the piezoelectric elements act as high pass filters and are sensitive to any sudden changes in either load or the rate of change of load in time. The load vanishing does not occur smoothly but is a sudden event, so it could cause the small spikes in the experimental results. The spikes could also be due to instantaneous shakings of the frame resulting from sudden discontinuation of the

applied force. We suspect these shakings are the source of the minor spikes since every force load applied through the jaws are measured and accounted for by the models. The closeness of the experimental and analytical modeling results indicates that the quasi-static approximation made in analytical modeling has been valid. The quasi-static models were applied since the dynamic forces are much less than the applied force, and the excitation frequency is significantly smaller than the natural frequency of the sensor in the thickness direction.

A.5.2 S5b. Sensor on mock skin

Comparison of the analytical results with finite element and theoretical models for sensor on a mock skin subjected to compressive loads identifies a close agreement. Similar to compression tests with bare sensors, a spike is observed in experiments at the moment of the sudden force removal. This spike is related to the vibrations of the instrument at the moment of motion reversal. Another feature observed in the plots for a cFaCES on mock skin is the effect of the viscoelasticity of mock skin on the experimental results. The damping is more significant in the plots associated with higher levels of the excitation force. This is because the amplitude of motion increases with the input force and thus magnifies energy dissipation. Both analytical and FEMs are in close match with the experimental results.

A.5.3 S5c. Sensor on mock skin with Tegaderm® tape

Finite element and analytical models are both successful in modeling the effect of Tegaderm® tape placed on top of the cFaCES-mock skin system, as demonstrated by the close agreement between the modeling and experimental results. Adding the tape increases the damping. One notable feature in modeling and experimental results is the difference between the depth of the drops in voltage in theoretical models as compared to experimental results. Both analytical and FEMs predict a more significant drop after the spikes than what is observed in the experiments. This translates to asymmetric orbit if one plots the phase portrait of response. The asymmetric

orbits could be caused by nonlinearities in a system [55,106–108]. It is likely that this difference between modeling and experimental results is due to nonlinearity of the test setup.

A.6 Note S6: Theoretical modeling of effect of cFaCES lamination on surface strain

After lamination of the cFaCES on the skin, the strain measured by the DIC method is not that of the skin. Instead, the measured strain is the strain at the top of the 3M Tegaderm tape securing the cFaCES to the skin. Our FEM model reveals that the strain at the top surface of the sensor is an order of magnitude smaller than that at the top of the skin. We have additionally performed a detailed stiffness analysis to ensure the cFaCES is not so stiff as to be disruptive to skin deformations. Therefore, the change in DIC-measured strain when cFaCES is laminated on the skin does not imply that the skin deformations have changed.

The strain distribution in the cFaCES varies significantly across the thickness. The cFaCES sensor is composed of soft layers such as the PDMS and the 3M Tegaderm tape layer as well as the much stiffer AlN layer in between. To better understand the strain distributions, we have conducted FEM analysis. In this analysis we have included a layer representing skin and we have included the cFaCES in full detail, including the PDMS layer, the AlN sensing elements, and the Tegaderm tape. We represent muscle motion by applying some strain (1%) to the skin and observe the resulting strain distribution in all layers. As illustrated qualitatively in Fig. S125a and quantitatively in Fig. S125b, the strain gradually decreases as we move up from the skin surface, which is adhered to the bottom of the PDMS substrate). Since the AlN layer is several orders of magnitude stiffer compared to the PDMS layer, the strain in the AlN layer is negligible. Looking at the top surface of the PDMS layer, the portions that connect to the AlN layer have minimal strain while the portions that directly connect to the 3M tape have notable strain.

Moving up in the Tegaderm tape, the strain increases, because the larger strain from the PDMS layer propagates over the AlN areas to the tape.

The quantified strain variation along the thickness of the cFaCES is illustrated in Fig. S125b. Due to the high stiffness of the AlN layer, the strain in that layer is significantly smaller than that at the skin surface. The strain is approximately uniform in the AlN layer, with variations on the order of 10^{-8} %. This verifies the strain uniformity assumption in our analytical model. Interestingly, the strain increases with the Z-coordinate when moving out of the piezoelectric and into the 3M Tegaderm tape layer. As a result, the strain at the surface of the Tegaderm tape is about twice the strain at the piezoelectric layer. Despite this increase, the strain at the top surface of the cFaCES + Tegaderm tape is significantly smaller (one order of magnitude less) than the strain at the skin level. This suggests that the reduction in the measured strain with cFaCES (Fig. 3) can be attributed to the decrease of the strain through the thickness of the sensor.

Similarly, the strain distribution in the X-coordinate along the top layer of the 3M Tegaderm tape varies significantly, depending on whether the location is above a piezoelectric element or above the area between two elements (Fig. S125c and S125d). The value of the strain is smallest over the AlN elements and is largest at half point between two elements. We can relate this back to the difference in values between the theoretically-predicted values and the DIC-measured values seen in Figure 4. The X-axis strain anisotropy combined with the fact that the AlN elements are not readily distinguishable from the 3D-DIC analysis, suggests that the location of the DIC-measured strain could be slightly off from over the AlN patches. This is because, after speckling, the camera cannot determine where the AlN elements are exactly located, and, additionally, the spatial resolution of the cameras and speckling setup is not high enough to identify if a surface location is above the AlN element or between them. Instead, due

to blinding, the locations picked for the 3D-DIC analysis are determined by measurements taken on the subject's face, without consulting the post-analysis 3D-DIC strain deformation pattern to determine if that location is exactly above the AlN element or not (measurements are taken by a person different from the one conducting the DIC experiment, and are taken at a time after lamination of the cFaCES on the skin and before camera images are taken). This causes variability in the magnitude of the measured strain by 3D-DIC and justifies the fact that the magnitude of discrepancy (1-7x) between the model predictions and 3D-DIC measurements are not the same for different motions (Fig. S123 and S124).

We further analyze whether placing the sensor on the skin could potentially result in reduction of the skin deformation itself. This phenomenon has multiple implications: it could (i) disrupt the facial gestures and (ii) make the sensor uncomfortable to wear. To ensure these side effects do not occur, we make sure the stiffness of the sensor is not significantly larger than that of the skin. The reasoning is as follows. The facial muscles cause motions in the skin, and which can propagate to the device laminated on top (Fig. S125e). The amplitude of the motion is approximately equal to the force applied by the muscle divided by its stiffness. Adding the sensor can be modeled as adding a spring in parallel to the system. This stiffness of the sensor is thus effectively added to the stiffness of the skin. If the stiffness of the sensor is of the same order as that of the skin we could conclude that adding the sensor does not disrupt facial gestures. An approximate closed form formula can be derived by assuming the piezoelectric layer covers the entire sensor. In that situation, the overall stiffness of the cFaCES-skin system is $k = \frac{(E_p t_p + E_s t_s + E_{skin} t_{skin})w}{L}$, where the subscripts *p*, *s,* and *skin* refer to piezoelectric, substrate, and skin layers, respectively, *E* is Young's Modulus, *t* is thickness, *w* is width, and *L* is the length.

An approximate value for the equivalent stiffness of the skin at the locations of lamination of cFaCES is calculated based on the approximate Young's modulus of the skin and its thickness. Considering the portion of the skin directly under the cFaCES sensor as the part affected by the sensor, we calculate its stiffness as $k_{skin} = E_{skin} w t_{skin} / L$. The skin Young's Modulus is assumed to be *E* ~31 kPa [91] and thickness ~6.39 mm (this corresponds to experimental average values from cheek skin) [92]. The resulting estimated value of the stiffness of the skin is 113 N/m. The current device design with 1.5 μm thick AlN has a stiffness of 166 N/m. Comparing this to the stiffness of the cFaCES sensor reveals that the stiffness of the sensor is of the same order as the skin. As a result, the lamination of cFaCES on the skin with Tegaderm tape will not significantly affect the skin deformations. Figures S125f and S125g show the variation of the compliance of the cFaCES-skin system ($(k_{skin} + k_{cFaCES})^{-1}$, where k_{skin} is the stiffness of the skin and k_{cFaCES} is the stiffness of the cFaCES) as a function of design parameters.

Appendix B: Supplementary Tables

Technology	A (%) / No	SRT (ms)	Size (cm³)	YM (MPa)	Wiring	VIC
cFaCES + RTD	75 - 87 / 3	~5	2.5 x 3.5 x 0.01	~2	Wired	yes
EMG-based	92 - 98 / 11+	~O(1)	15 x 15 x 5+**	>1000	Wired or BLE	no
camera-based	66 - 95+ / 2 - 6	10 - 66	not portable**	non-contact***	non-contact***	no

Technology	CT (hr)	SR (Hz)	TT (hr)	QTD (hr*elts)	PT (s)	CP
cFaCES + RTD	4-8*	100	0.5	0.16	1	RPi (1.4 GHz)
EMG-based	0.08*	128 - 250	NR	6.4 - 217	0.43 - 2.5	PC (2.5 GHz+)
camera-based	0 - NR*	15 - 100	0 - NR	0 - 0.75	NR	PC (2.5 GHz+)

Performance Interface Coupling Computational Load

Table S1. Comparison summary of nonverbal communication technologies based on performance, interface coupling and computational load.

Comparison of this work (conformable facial code extrapolation sensor (cFaCES) + real-time decoding (RTD)) with existing nonverbal communication technologies - electromyography (EMG)-based [8,9] or camera-based technologies [12,16] - via metrics for performance (yellow), interface coupling (orange), and computational load (green). Upon comparison to metrics available in the literature for EMG-based and camera-based nonverbal communication systems, this work represents a technology with significant improvements towards more seamless interface coupling and lower computational load, while maintaining modest accuracy levels. Performance metrics encompass accuracy (A) [average percentage of motions correctly identified], number of motions attempting to be distinguished (No), and sensor response time (SRT) [amount of time delay between the start of facial movement and the start of sensor capture of that movement]. O(1) indicates that the EMG response time is on the order of 1 ms. Higher accuracy over a larger number of motions and with faster signal response is generally

desired. Interface coupling metrics include interface size [size of the interface that couples directly with the face], Young's modulus (YM), wiring [wired connections or mode of wireless communication], and visual invisibility capability (VIC) [ability to camouflage the facial interface with the facial skin]. Generally, smaller size, lower modulus, wireless-enabled technologies with the ability for visual camouflage are desired. Computational load metrics include calibration time (CT) [amount of time required to calibrate the technology before usage], training time (TT) [amount of time required for training a machine learning model, if machine learning is involved], quantity of training data (QTD) [amount of training data used in training the model, measured in hours of facial motions data collected multiplied by the number of sensing elements used in the measurements], prediction time (PT) [amount of time the trained model requires for predicting the classification of a facial motion], and computing processor (CP) [computational platform on which training and testing occur, which is either a Raspberry Pi (RPi) or a personal computer (PC) with a certain processor frequency]. Lower computational load metrics coupled with slower and smaller processors are generally desired. A designation of NR indicates that a specific metric was not reported in studies involving a specific technology. Notes: *Calibration times for the cFaCES represents a one-time user calibration to determine sensor placement location that does not need to be repeated upon subsequent usage, even if the sensor is delaminated and re-laminated (Fig. S1). For EMG-based systems, calibration time of at least 5 min is required after each removal or change in environmental condition, due EMG's variability with humidity and temperature, which change skin capacitance [109,110]. For camera-based systems which are not based on machine learning models, calibration is sometimes not needed. In cases where digital image correlation (DIC) is utilized for facial motion prediction, the calibration time will consist of the time for speckling and adjusting the lighting and sharpness settings of the cameras. **Size of EMG-based systems represent the size of the headsets normally worn at the neck, with electrodes wrapping around the head and mounting on the face. Size of camera-based systems are large and vary widely, but since these systems are not portable, the range of

their sizes is not relevant. ***The non-contact nature of the optical measurements made by camera-based systems renders its Young's modulus and wiring method irrelevant, since the subject is not physically coupled to the technology.

Form Factor	Study	Materials	FWHM of XRD Rocking Curve
Rigid	Bi et al. (2014) [77]	AlN/Si (100)	1.63°
	Yang et al. (2014) [78]	AlN/Mo/Si (100)	2.40°
	Lu et al. (2018) [79]	AlN/Si (100)	1.77°
Flexible	Akiyama et al. (2007) [32]	AlN/PI	8.3°
	Jackson et al. (2013) [75]	AlN/PI	5.1°
	Li et al. (2016) [76]	AlN/PI	2.96°
Conformable	This work	PDMS/PI/Mo/AlN/Mo/SiO_2	1.69°

Table S2. Comparison summary of AlN crystallinity under different flexibilities.

Comparison of the full-width at half maximum (FWHM) of the XRD rocking curve performed on the AlN layer for different MEMS technologies shows that work's (pink) novel processing of AlN thin films in conformable form factors maintains high quality of AlN crystallinity, comparable to existing methods for AlN thin film processing on rigid substrates [77–79] (violet), and at least 1.5 times better than achievable by methods for AlN processing on flexible substrates [32,75,76] (blue). Material abbreviations: silicon (Si), molybdenum (Mo), polyimide (PI), polydimethylsiloxane (PDMS), silicon dioxide (SiO_2).

Motion	Total frames*	Total time (s)
Twitch #1	55	1.83
Twitch #2	55	1.83
Smile #1	49	1.63
Open Mouth	49	1.63
Smile #2	52	1.73
Pursed Lips	53	1.77
Vowel I	45	1.50
	Average	1.71
	St. Dev.	0.12

Table S3. Lag times in real-time decoding.

Analysis of continuous recorded sessions, similar to that depicted in Movie S8, of real-time decoding (RTD) on a healthy subject show that the lag time between the end of the user's performance of the motion and the display of the classification result has an average of ~1.71 ± 0.12 s. *Note: Footage was recorded at 30 frames per second.

Appendix C: Supplementary Figures

Fig. S1. Steps for repeatable lamination of a cFaCES in the facial location.

A) The subject's face is free of lotions, creams, and oils. B) A low-stretch fabric is held in place over the region of interest on the face upon which the sensor is to be placed. The fabric is fitted over facial features such as the chin and nose. C) to E) A thin marker is used to outline key features of the face, such as corners of the ear, nose, mouth, and eye, which can be used to re-align the fabric. F) The fabric is cut along the drawn lines and checked for alignment with facial features. G) to H) A 3 cm x 5 cm area is outlined and cut out of the fabric. This location is where the cFaCES and Tegaderm® will be placed. Two pieces of clear, pressure-sensitive tape are placed on the short sides of the cut-out rectangle to achieve adhesion with Tegaderm® tape. A pressure-sensitive tape with relatively low adhesion force to the non-sticky side of the Tegaderm® tape is preferred. This creates the alignment scaffold. I) The cFaCES is placed on Tegaderm® tape's sticky side and the non-sticky side of Tegaderm® tape is adhered onto the sticky side of the alignment scaffold and prepared for attachment to the face. J) to L) The alignment scaffold with the cFaCES attached is laminated on the face, starting from one edge and making sure that all previously marked key features are aligned. M) to O) Removal of the alignment scaffold leaves behind the cFaCES laminated on the skin in a particular region of interest. P) to Q) Paper backing on Tegaderm® tape is removed so the sensor can freely follow facial deformations. R) to T) Once experiments are completed, a tweezer can be used to remove the cFaCES from the facial skin. For the same subject, steps H) - Q) can be followed across different sessions of sensor usage to achieve placement in the same location in a repeatable manner. Before, during, and after lamination of cFaCES on facial skin, no observable inflammation occurs, as evidenced during five-hour trials on U) - W) a healthy subject and V) - Z) an ALS subject. The cFaCES thus permits soft, reversible lamination on facial skin without causing any inflammation and/or allergic reactions while remaining stable across a range of temperatures and humidities on the human skin [18,29–32].

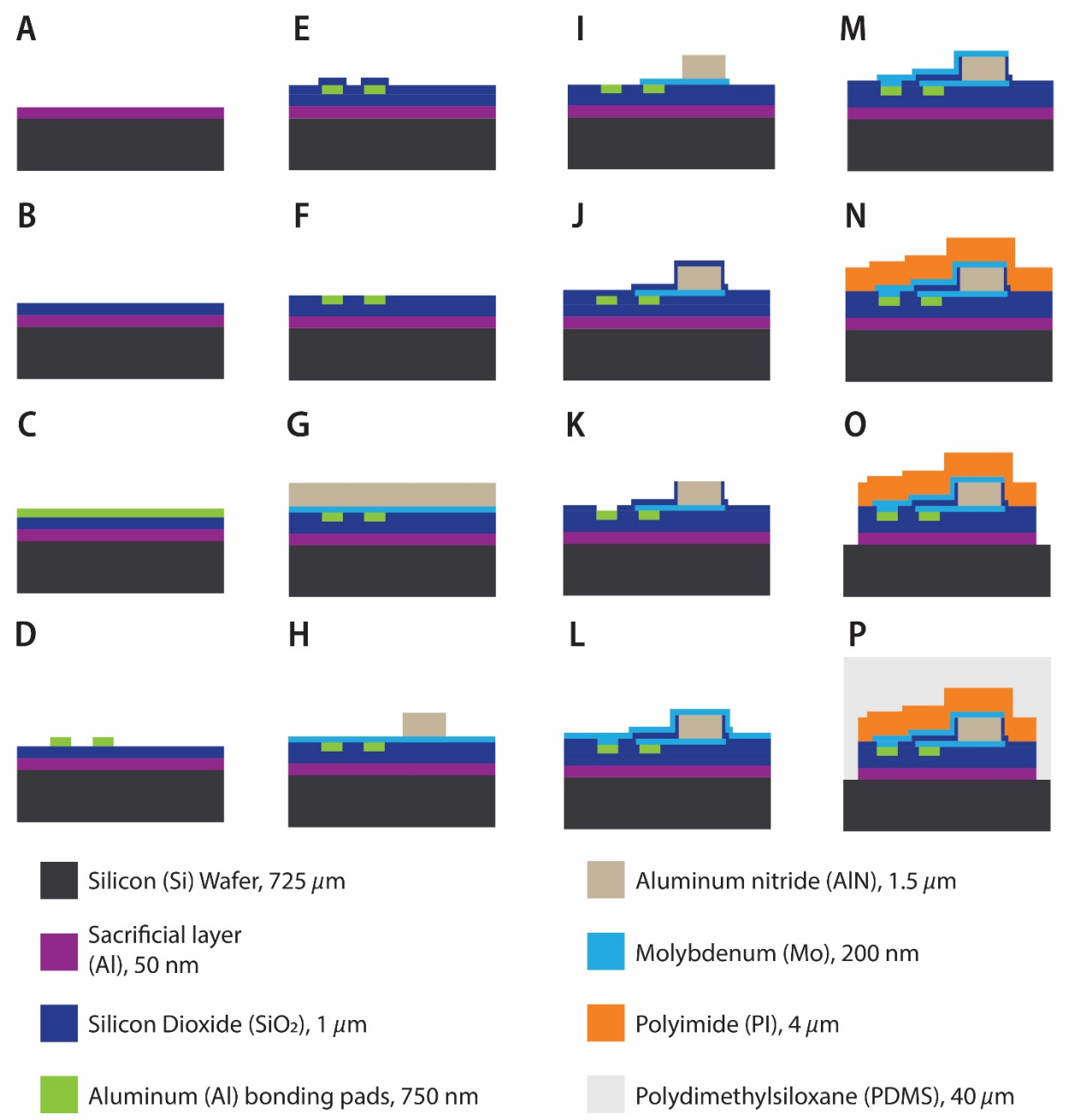

Fig. S2. Microfabrication steps for a cFaCES.

Each step of microfabrication of a cFaCES is represented by a depiction of the cross section of the device after that step. A) Deposition of sacrificial layer onto surface of cleaned Si wafer. B) Growth of SiO_2 layer using PECVD C) Deposition of aluminum layer and D) patterning to create bonding pads. E) Continued growth of SiO_2 layer using PECVD. F) Grinding of SiO_2 layer to

desired thickness. G) Sputtering of Mo electrode and of AlN layers. H) Patterning of AlN layer. I) Patterning of Mo electrode. J) Growth and K) patterning of oxide insulating layer. L) Sputtering and M) patterning of Mo electrode. N) Spin-coating and O) patterning of PI encapsulation layer. P) Spin-coating PDMS to create encapsulation layer. Subsequent anodization releases the final cFaCES device from the substrate, after which bonding pads are exposed by patterning the SiO_2 layer. Figure not to scale.

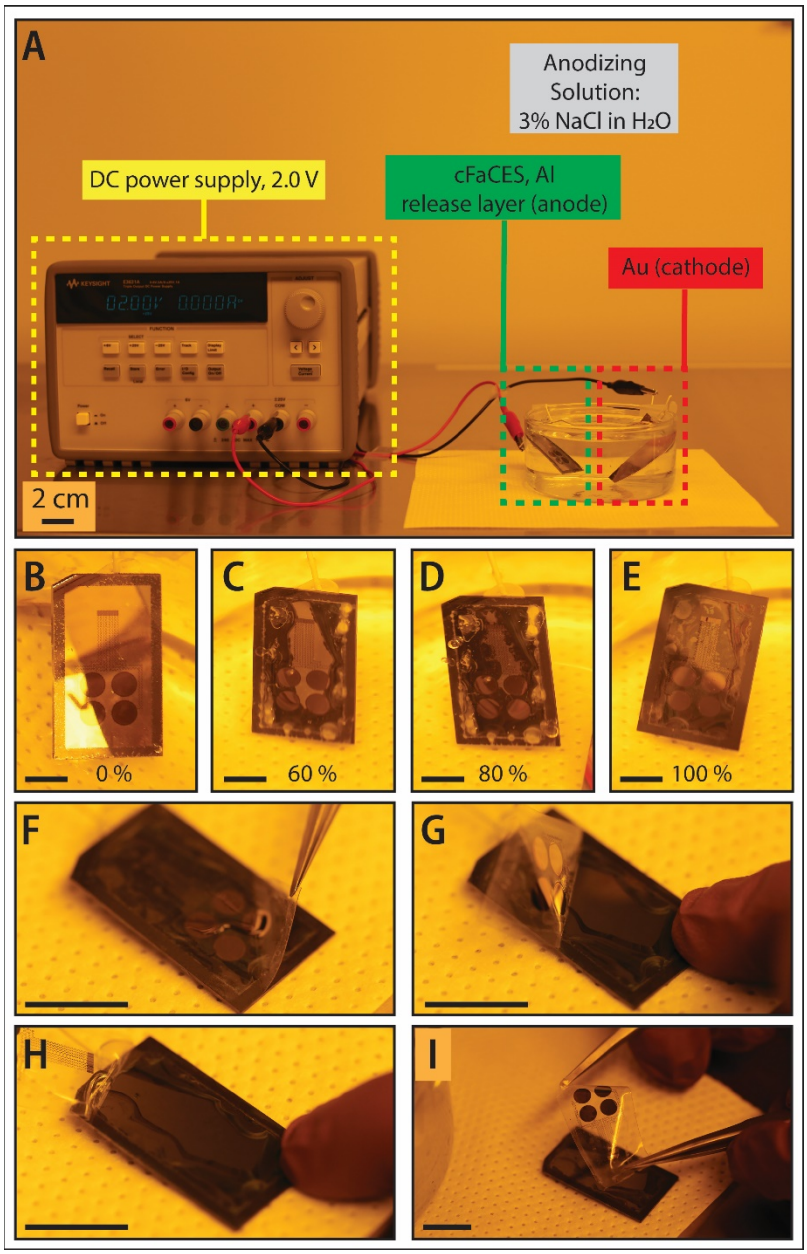

Fig. S3. Release process of a cFaCES from Si wafer in the cleanroom facility, YellowBox.

A) Experimental setup for the anodization process by which the cFaCES is released from the Si wafer. A direct current (dc) power supply provides energy for an anodization process, during which the sacrificial aluminum layer is etched and the gold at the cathode undergoes oxidation. B)-E) Release process, which happens over 48 hr, in varying stages. E) In a fully released

cFaCES, the shiny nickel layer visible in B) has been completely etched. F-H) Subsequent peeling of a cFaCES from the rigid substrate achieves its final conformable form factor. Scale bars for each subgraph correspond to 2 cm.

Fig. S4. Colorized SEM image of a cFaCES on a mock skin.

The SEM image of a cFaCES on a mock skin shows the intimate coupling of the sensor on a mock skin surface. The image is colorized to distinguish between layers of the sensor. The

orange color refers to the PI layer, the pink color represents the AlN layer, and the silver color represents the Mo bottom electrode and bonding pads.

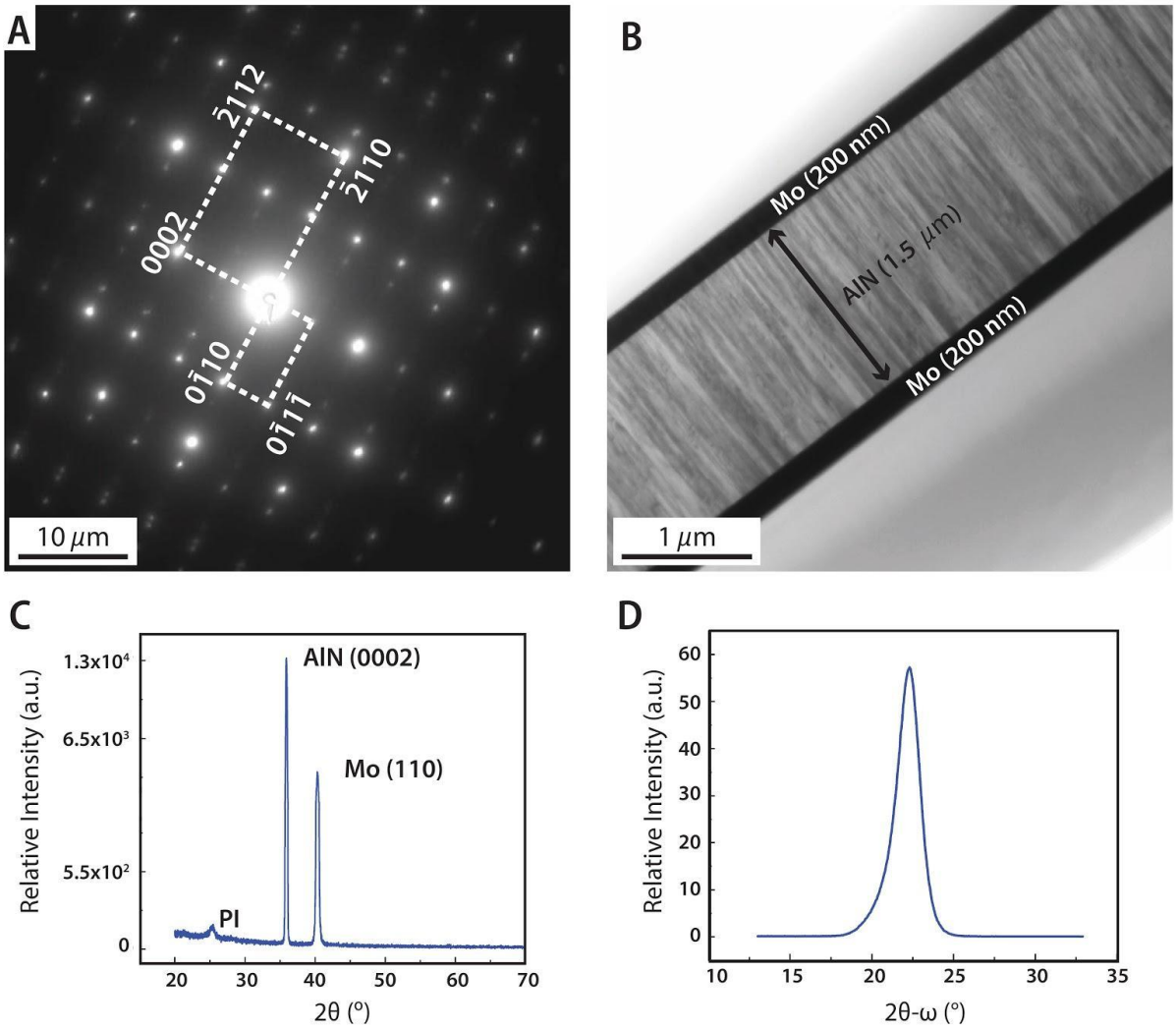

Fig. S5. Crystal structure of the AlN piezoelectric layer of a cFaCES.

A) Diffraction pattern observed from X-Ray diffraction (XRD) crystallography confirms wurtzite structure of AlN, with primary crystallographic planes labeled. B) Transmission electron microscopy (TEM) Brightfield image of the cross-section of the sputtered Mo-AlN-Mo capacitor-type structure demonstrates the anisotropic growth of the AlN layer by way of physical vapor deposition (PVD). C) Relative intensity of peaks from XRD analysis demonstrates crystallinity of AlN layer. Peaks from Mo and polyimide (PI) exist since these layers sandwich the AlN

piezoelectric element. D) XRD rocking curve confirms high degree of crystal perfection, showing minimal deviation from ideal Bragg diffraction even in the thin-film case (full-width at half maximum (FWHM) ~1.69°).

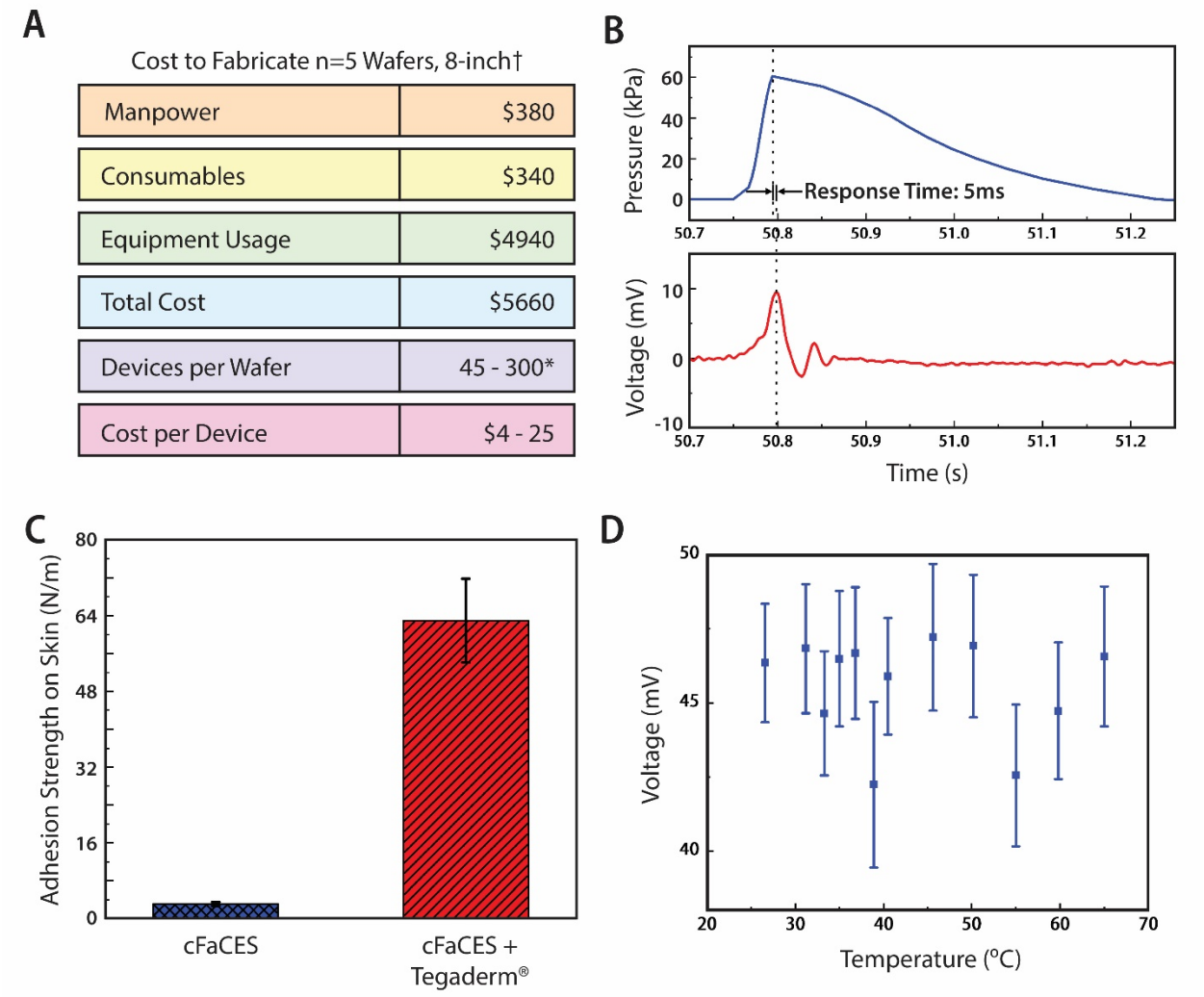

Fig. S6. Various characterizations of a cFaCES.

A) Cost analysis of fabrication reveals that the cost per cFaCES device can range from approximately $4 (1 cm^2 device area) to $25 (7 cm^2 device area), *depending on the size of the device, which depends on the number and size of the piezoelectric sensing elements desired on each device. †Calculations are shown for an 8-inch wafer process, but the price could decrease

even further if a 10-inch or 12-inch wafer process is undertaken for fabrication. The main cost derives from usage of equipment for materials processing, including plasma-enhanced chemical vapor deposition (PECVD), physical vapor deposition (PVD), lithography, electron-beam direct-write mask fabrication, and wet bench usage. B) Response time, i.e. time delay between mechanical impulse peak and voltage response peak of a cFaCES, is measured to be approximately 5 ms. C) Measurements of adhesion to the epidermis of the skin *in vivo* shows that the cFaCES adhesion strength is ~4 N/m, while the cFaCES with Tegaderm® tape adhesion strength is ~60 N/m. Error bar represents calculated standard error (n = 3). D) cFaCES demonstrates stability of voltage output across a wide range of temperatures (25 - 65°C). Voltage measured represents the voltage of the sensor with 0 mechanical input. Error bar represents calculated standard error (n = 5).

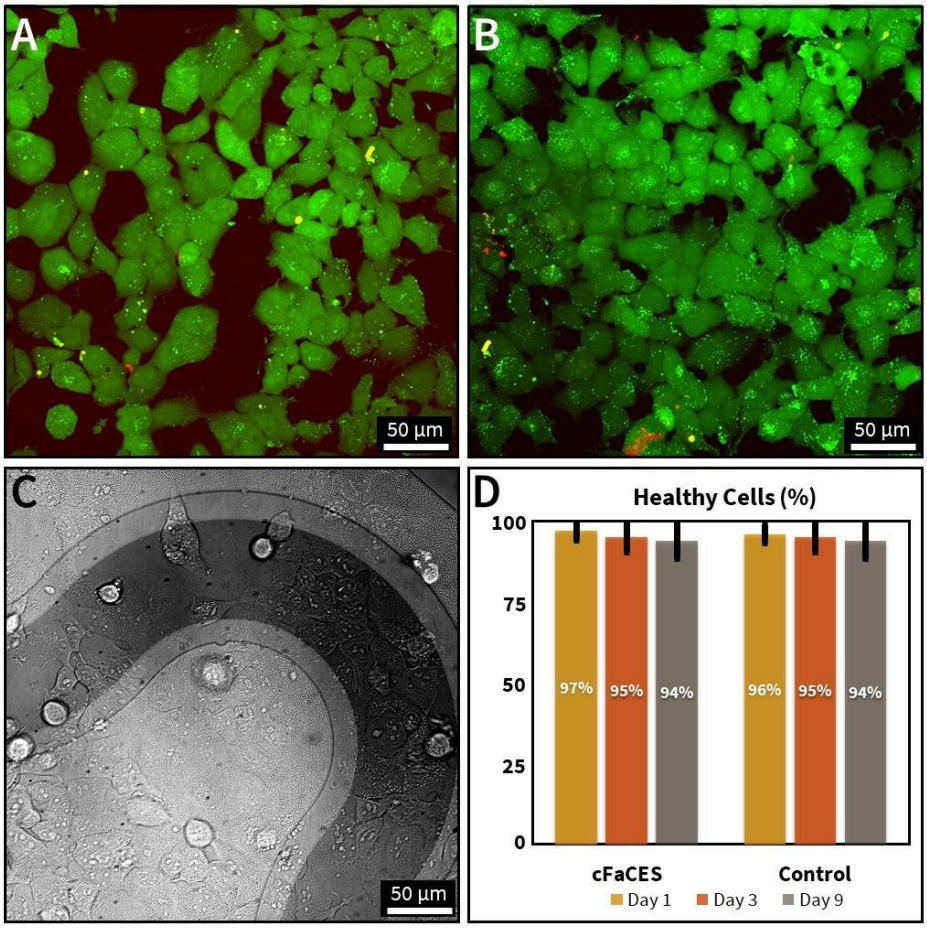

Fig. S7. Biocompatibility testing of a cFaCES.

Fluorescence microscopy images show live/dead viability assay with live human epidermal keratinocyte cells (green) and dead cells (red) after A) 3 days and B) 9 days of culturing on a cFaCES. Yellow regions denote overlapping live and dead staining artifacts. C) Brightfield microscopy image of cells on AlN interconnects, encapsulated by PDMS. D) Lactate dehydrogenase assay shows that there are no indications of toxicity for cells on a cFaCES substrate at day 9, and healthy cell percentage is comparable to that for the control. For this test, 6 cFaCES samples were cut to 1 cm^2 squares, which yielded 10 squares. Error bar is calculated standard error (n = 10).

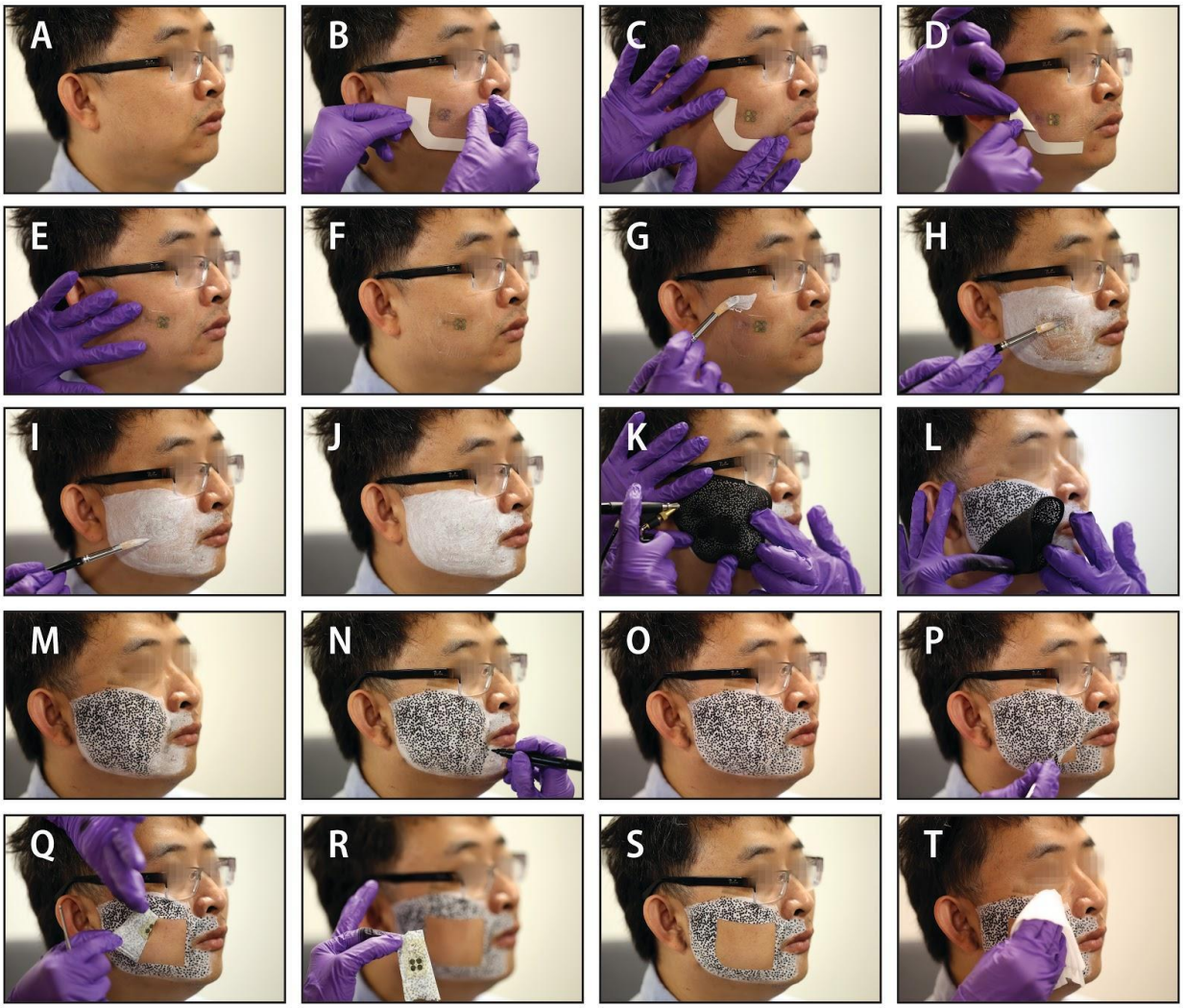

Fig. S8. Steps for speckling subject's face for 3D-DIC experiments.

Steps B) to F) and P) to R) apply only in cases for DIC experiments with the sensor laminated on the face. DIC experiments studying strain on the facial skin itself omits these steps. A) Subject's face is free of lotions, creams, and oils. B) to F) A cFaCES sensor is attached to Tegaderm® tape and lined up in the correct location for lamination onto the facial skin (Fig. S33). Experiments reported in these results all come for a cFaCES laminated on the right side of the face, whether on the cheek or temple area. Paper backing on Tegaderm® tape is removed so the sensor can freely follow facial deformations. G) to J) A thin layer of non-toxic white makeup paint is applied over the facial skin and sensor and allowed to dry fully.

Sometimes a second layer of paint is applied to achieve an even, solid coat. K) to M) An airbrush loaded with non-toxic black makeup paint and a laser-cut foam stencil is used to apply a random pattern of speckled dots on top of the skin. N) to O) Any areas in which strain characterization is desired but are not covered by the stencil pattern are filled in manually with a black liquid eyeliner pencil. P) to T) Once 3D-DIC experiments are over, the cFaCES can be delaminated from the skin, which is finally cleaned with a makeup-removing cloth.

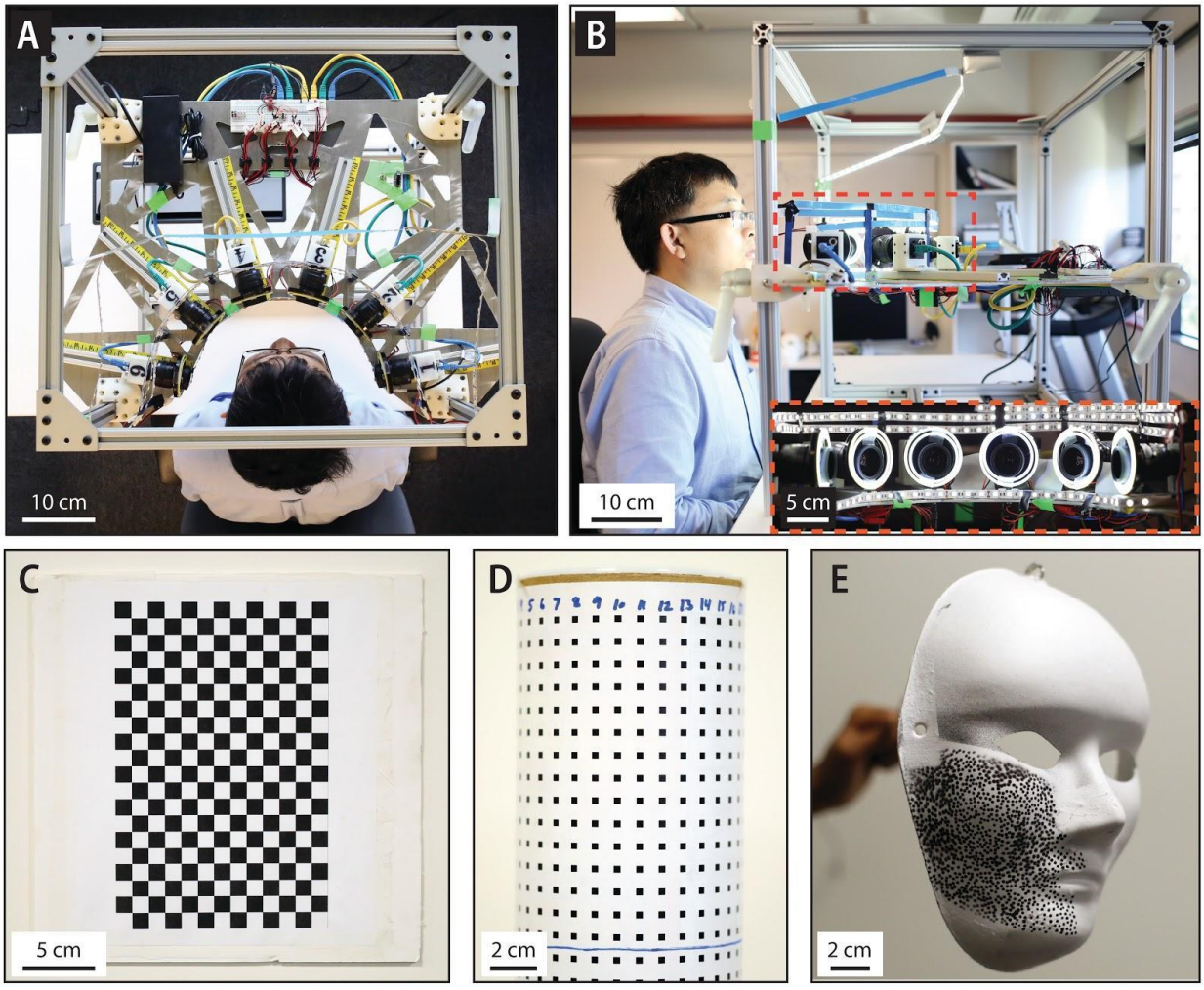

Fig. S9. Custom-built 3D-DIC setup and calibration objects.

A) Top view of DIC setup, which houses six cameras spaced radially around the subject's face in order to get full-field image capture during natural deformations of facial skin. The cameras

are connected to a network switch, which sends raw image data via ethernet to a host computer (not pictured). B) Right-side view of DIC setup, showing height adjustment knobs and LED string lights placed around the subject's face. Inset shows front view of cameras with ring lights around the camera lenses and extra LED strips placed around to increase the illumination of the subject's face. C) Distortion correction object, a flat piece of foam-core poster board cut to 27 cm x 27 cm, atop which is laminated a printed piece of paper with a black-and-white checkerboard. The checkerboard consists of a 13 x 20 grid of 1.15 mm side length squares. This object is used to determine the radial, tangential, and skew distortion parameters, as well as the focal length and principal point errors, of each of the cameras used in image capture, as guided by the batch adjustment (BA) model. D) Calibration object, a sturdy cylindrical object atop which is laminated a printed piece of paper with a uniform array of square dots. This object is used to determine the stereo calibration parameters for the DIC system, as guided by the direct linear transformation model (DLT), from which points in 2D-space are mapped onto 3D-space. E) Control object, which is a cardstock paper mask atop which is speckled the same random dot pattern used on the human subjects for *in vivo* measurement of skin strain. The control object is treated as a "subject" and used to determine and quantify potential sources of experimental error during image capture and photogrammetric strain calculation.

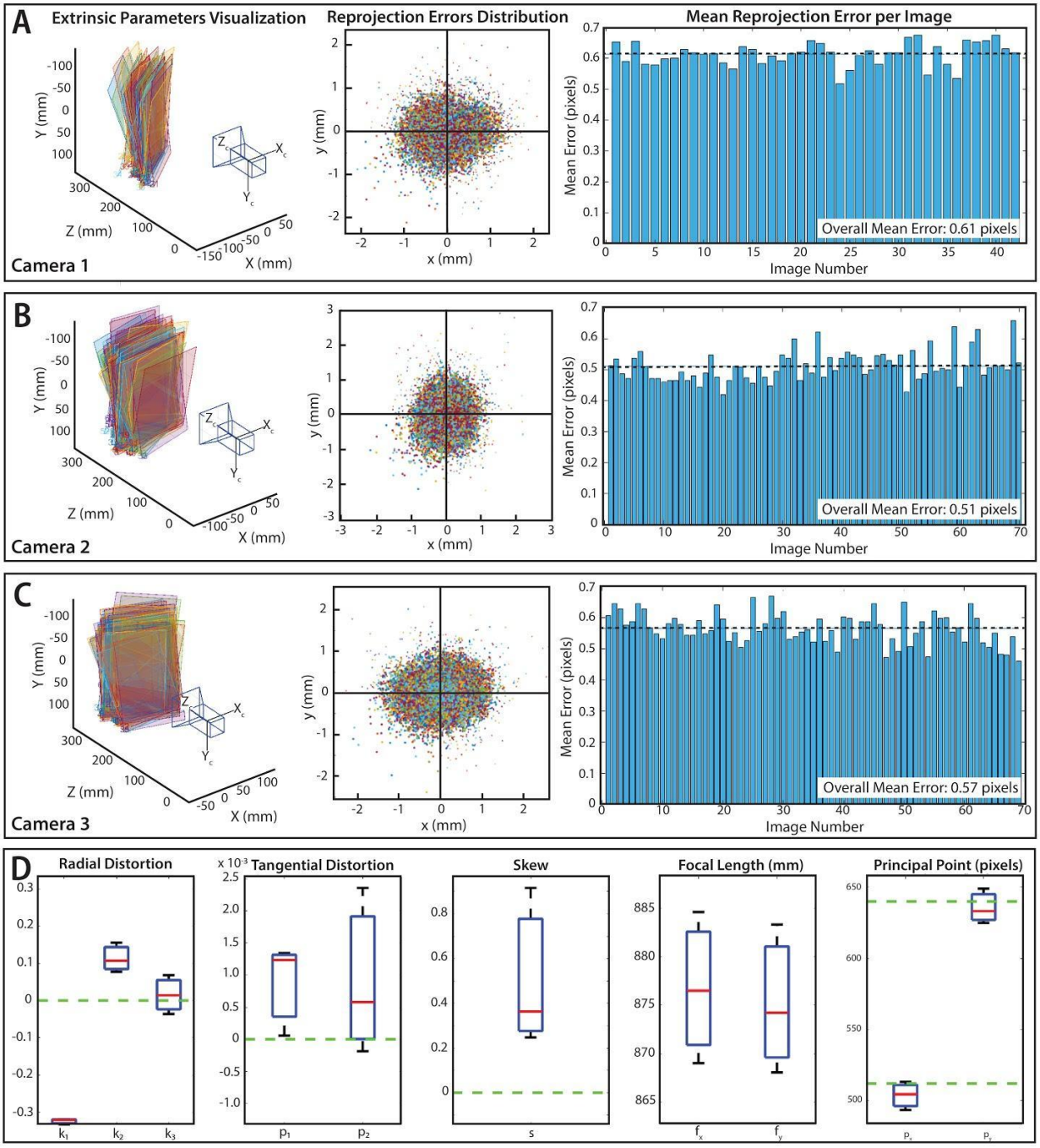

Fig. S10. 3D-DIC distortion correction (DC) results and calculation of camera parameters.

Three cameras (numbered 1, 2, and 3) were used to measure facial deformations. Images acquired from these three cameras of the distortion correction object were used to calculate intrinsic and extrinsic camera parameters, as well as 2D reprojection errors. a), b), and c)

Reprojection errors in cameras 1, 2, and 3 respectively show mean deviations from true points after application of distortion correction. 3D graph, left, visualizes the calculated orientation and placement of the distortion correction object with respect to each camera. 2D box graph, middle, reprojection errors plotted after distortion correction batch adjustment (BA) algorithm applied to acquired images of DC object. Reprojected points from which errors are determined are the internal corners of the checkerboard pattern. Histogram, right, shows the distribution of mean errors in pixels. d) Resultant analysis determines the radial distortion, tangential distortion, skew, focal length, and principal point parameters of each camera, and depicted graphs show box-and-whisker plot of these parameters from all of the cameras.

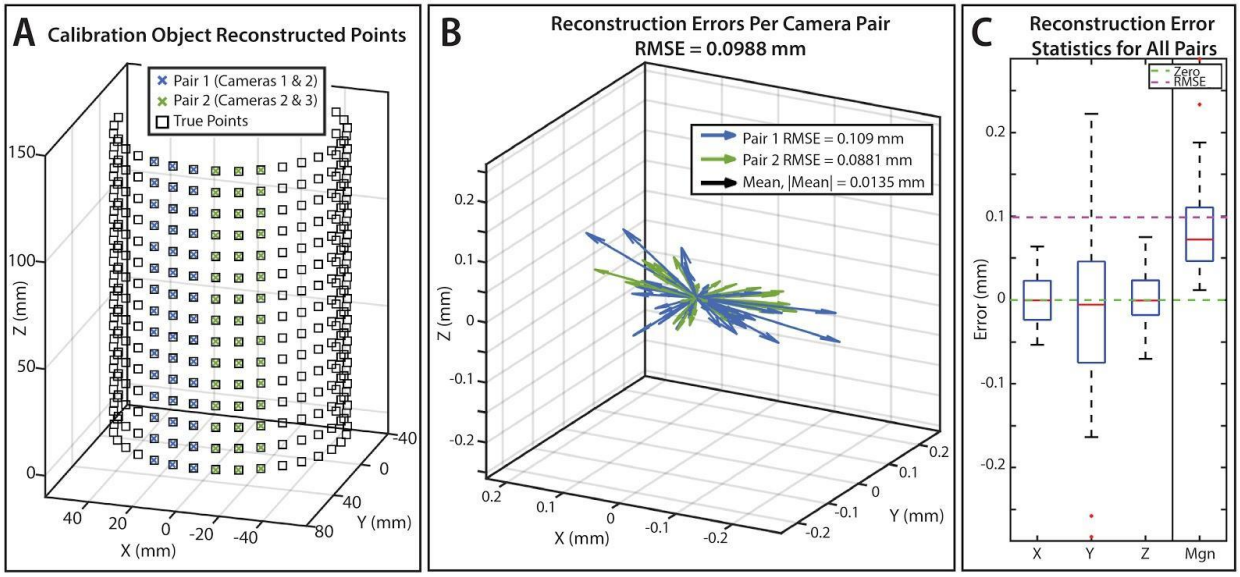

Fig. S11. 3D-DIC system calibration and calculation of reconstruction errors.

Images of the calibration object were used to calculate direct linear transformation (DLT) coefficients for projecting 2D image points into 3D space. A) The reconstructed 3D points (blue and green crosses) from each of two pairs of cameras (Pair 1: camera 1 and 2, Pair 2: camera 2 and 3) are overlaid on the true location of the 3D points (black boxes). B) Offset of the centroids of reconstructed 3D points from true 3D points are plotted and used to calculate the root mean-square error (RMSE) for 3D reconstruction using the custom DIC setup. RMSE ~ 100 μm. C) Reconstruction errors are shown for each axis. Y-axis errors, which correspond to depth information, presents the highest source of error. However, the RMSE error is low compared to the ~mm - cm scale of deformations studied by the DIC setup.

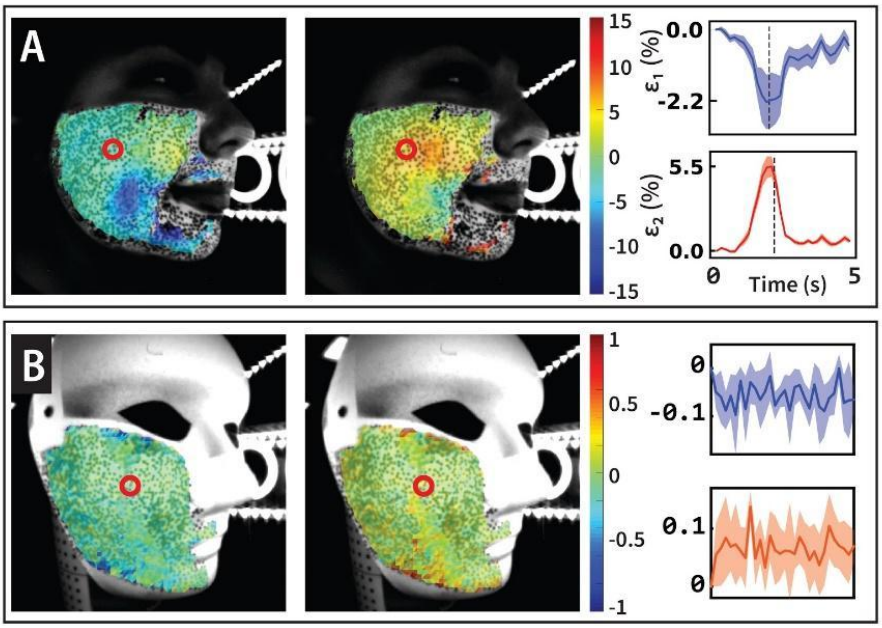

Fig. S12. Control (null strain) tests for 3D-DIC experiments.

Control tests were conducted to determine potential sources of experimental error during DIC data collection and measurements. A) For comparison, results for a twitch medium magnitude deformation for the healthy subject are shown. B) Results of DIC-calculated strain for the control object when it was held in front of the cameras by metal wire, with no human intervention. Strain (%) map scale bars for each trial are given immediately to the right of each pair of principal strain maps. Graph labels for B) are the same as shown in A). The location from which the strain was pulled is represented by the red circle, which corresponds to the same location on the speckle pattern for both cases. This constitutes a null strain test. Edges of the speckle pattern or areas of low lighting (bottom chin area of face mask) show higher strains (~1%) and are expected. The majority of the speckled control object is shown by DIC to experience strains of within 0.1% of zero. The difference in strain between A) and B) demonstrate that measured *in vivo* facial strains are at least an order of magnitude larger than potential sources of error, which establish the reliability of the DIC setup for calculating strains due to facial motions. Naturally, motions such as blink, which involve smaller facial deformations (< 1%) will have less reliable results in the current setup. The time scale is the same for all graphs.

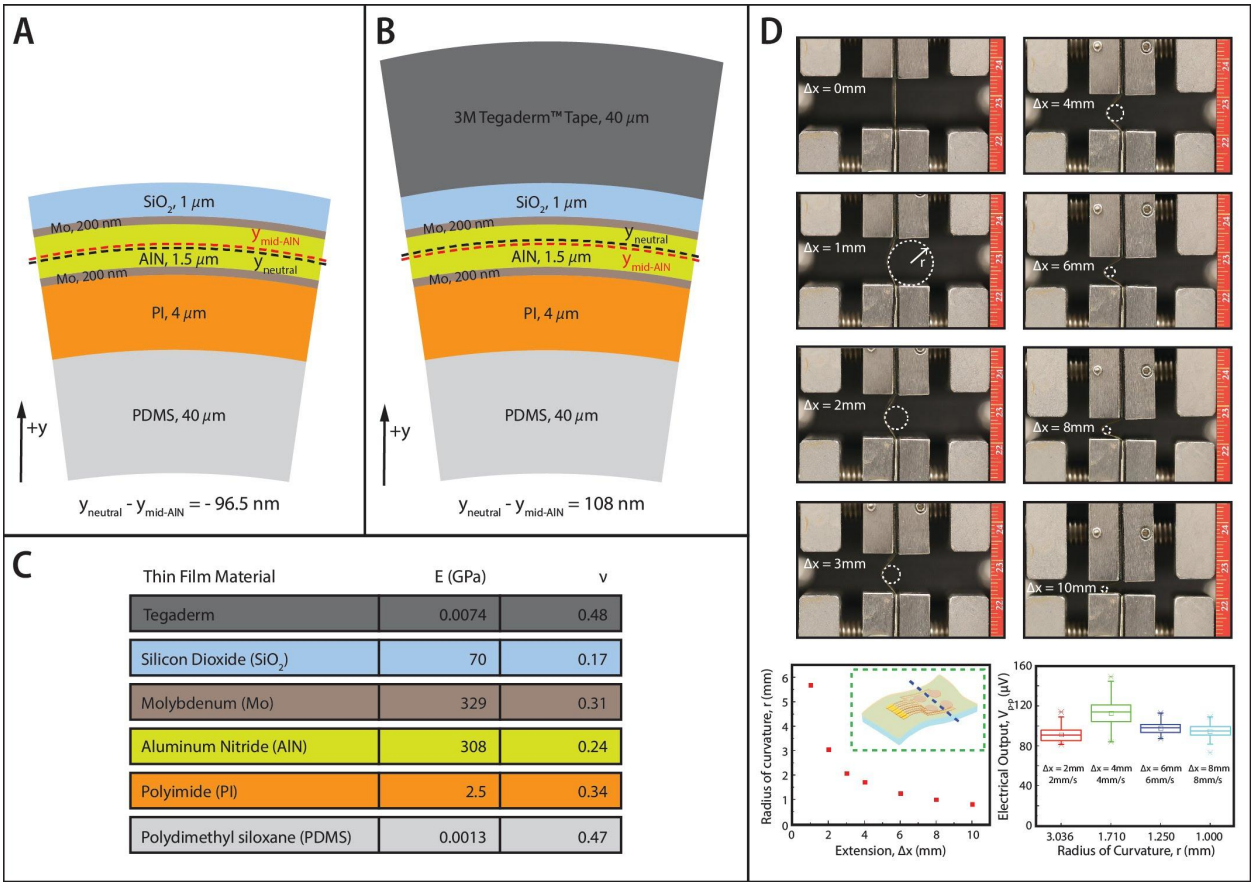

Fig. S13. Neutral mechanical plane (NMP) of the cFaCES.

A) Cross section of a cFaCES shows that its NMP without an adhesive layer on top is 96.5 nm below the midplane of the active piezoelectric layer, which is the AlN layer. B) The use of 3M Tegaderm® tape as an adhesive layer shifts the NMP to 107 nm above the midplane of the active layer, likely due to its low value of elastic modulus. Both cases keep the NMP within 150 nm (10%) of the midplane of the active layer. C) Elastic (Young's) modulus (E) and Poisson ratio (ν) for each material, which are used in the NMP calculation (Note S5). D) Radius of curvature (ROC) of a bare cFaCES with increasing buckling extension length. Each image inset depicts a cFaCES clamped and buckled with extension length (Δx), which leads to a certain radius of curvature. The radius of curvature decreases inversely with the increase in extension length (bottom left graph). The centerline of the buckling is in the middle of the cFaCES

piezoelectric element array (green dashed box). The sensor remained functional over 100 cycles and exhibited no more than 160 μV peak-to-peak voltage (V_{p-p}) at each radius of curvature when cyclic bending tests were conducted at 0.5 Hz for each of 2 mm (ROC = 3.036mm, orange), 4 mm (ROC = 1.710 mm, green), 6 mm (ROC = 1.250 mm, dark blue), and 8 mm (ROC = 1.000 mm, light blue) extensions with extension rates of 2 mm/s, 4 mm/s, 6 mm/s, and 8 mm/s respectively. Box plots are constructed with one-way ANOVA (n=3), which show no statistical difference in voltage output for each radius of curvature.

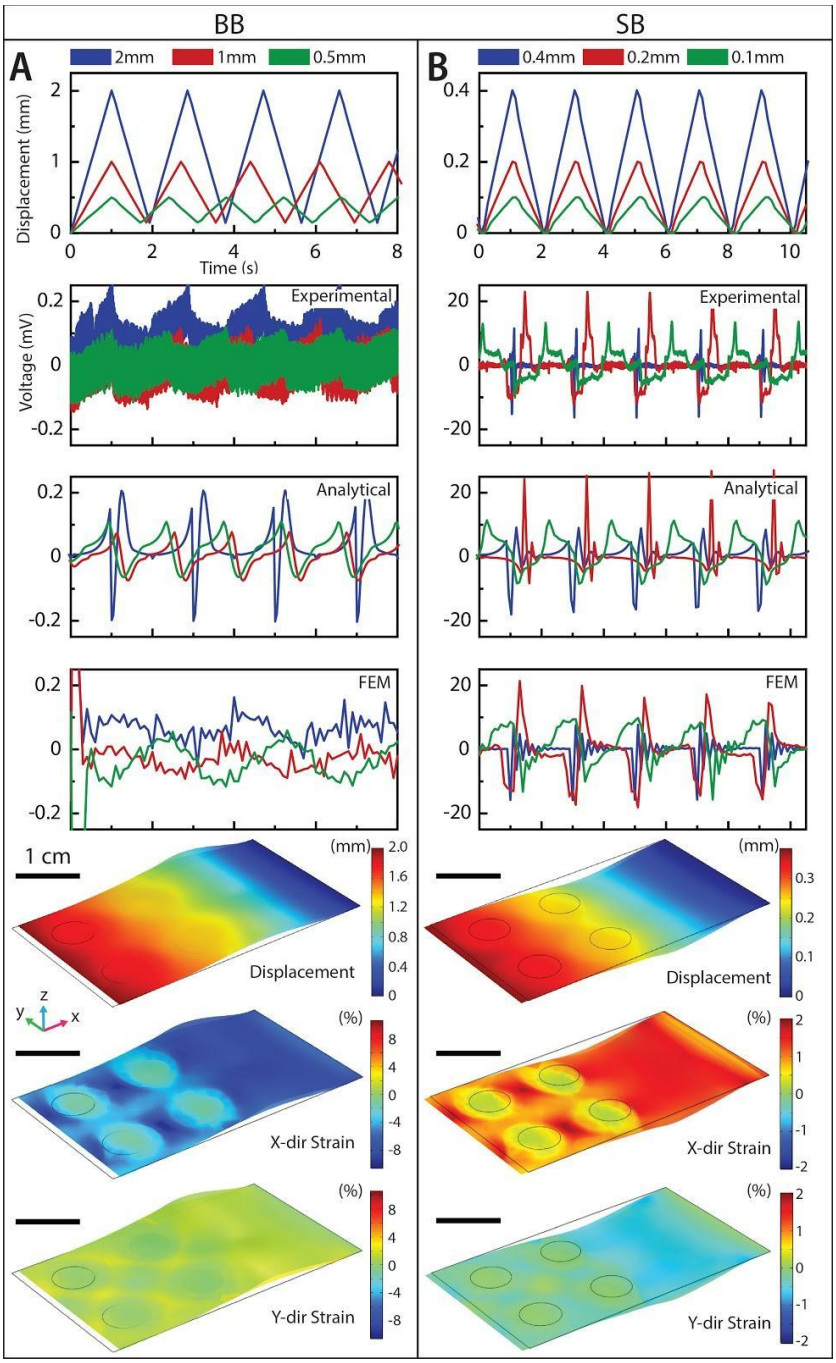

Fig. S14. *In vitro* mechanical characterization of the bare cFaCES during buckling and stretching.

Voltage output resulting from A) uniaxial buckling (BB) and B) uniaxial stretching (SB) of the bare cFaCES, not laminated on any external surface. Voltage outputs from one sensing element as observed experimentally and predicted via analytical and FEMs, in addition to strain fields

predicted by the FEM, are shown. Deformation and strain fields are shown in the deformed configuration for the highest axial displacements for BB (2 mm) and SB (0.4 mm). The outline of the undeformed cFaCES is shown by the thin gray wireframe in each strain map. The deformation (mm) and strain (%) scale bar for each strain map is given directly to its right side. Length scale bars for a) and b) are the same. The time scale is the same for all graphs.

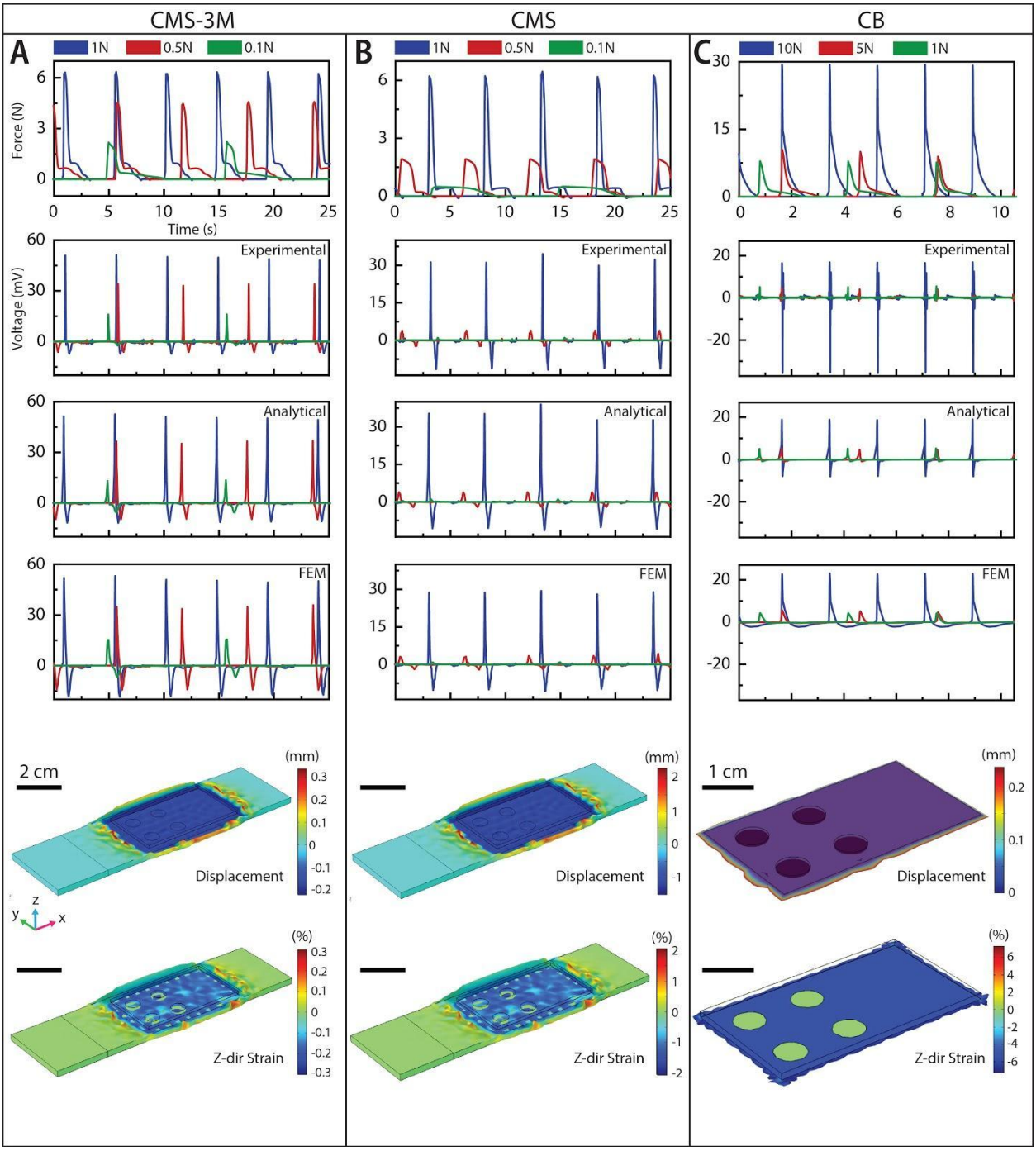

Fig. S15. *In vitro* mechanical characterization of the cFaCES during compression.

Voltage output resulting from uniaxial compression of the cFaCES A) secured onto mock skin with 3M Tegaderm® tape (CMS-3M), B) laminated on mock skin without Tegaderm® tape (CMS), and C) without lamination on any external surface (CB). Voltage outputs from one sensing element as observed experimentally and predicted via analytical and FEMs, in addition

to strain fields predicted by the FEM, are shown. Deformation and strain fields are shown in the deformed configuration for the highest axial forces for CMS-3M (1 N), CMS (1 N), and CB (10 N). The outline of the undeformed cFaCES or cFaCES-mock skin system is shown by the thin gray wireframe in each strain map. The deformation (mm) and strain (%) scale bar for each strain map is given directly to its right side. Length scale bars for a) and b) are the same. The time scale is the same for all graphs.

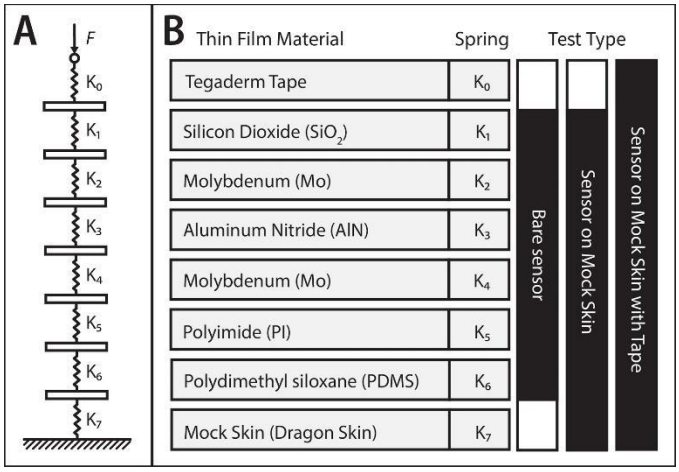

Fig. S16. The cFaCES stack-up used for theoretical modeling of compression.

A) Stiffness model of a cFaCES as used for compression testing. B) Correspondence between spring constants in stiffness model and layers in the cFaCES.

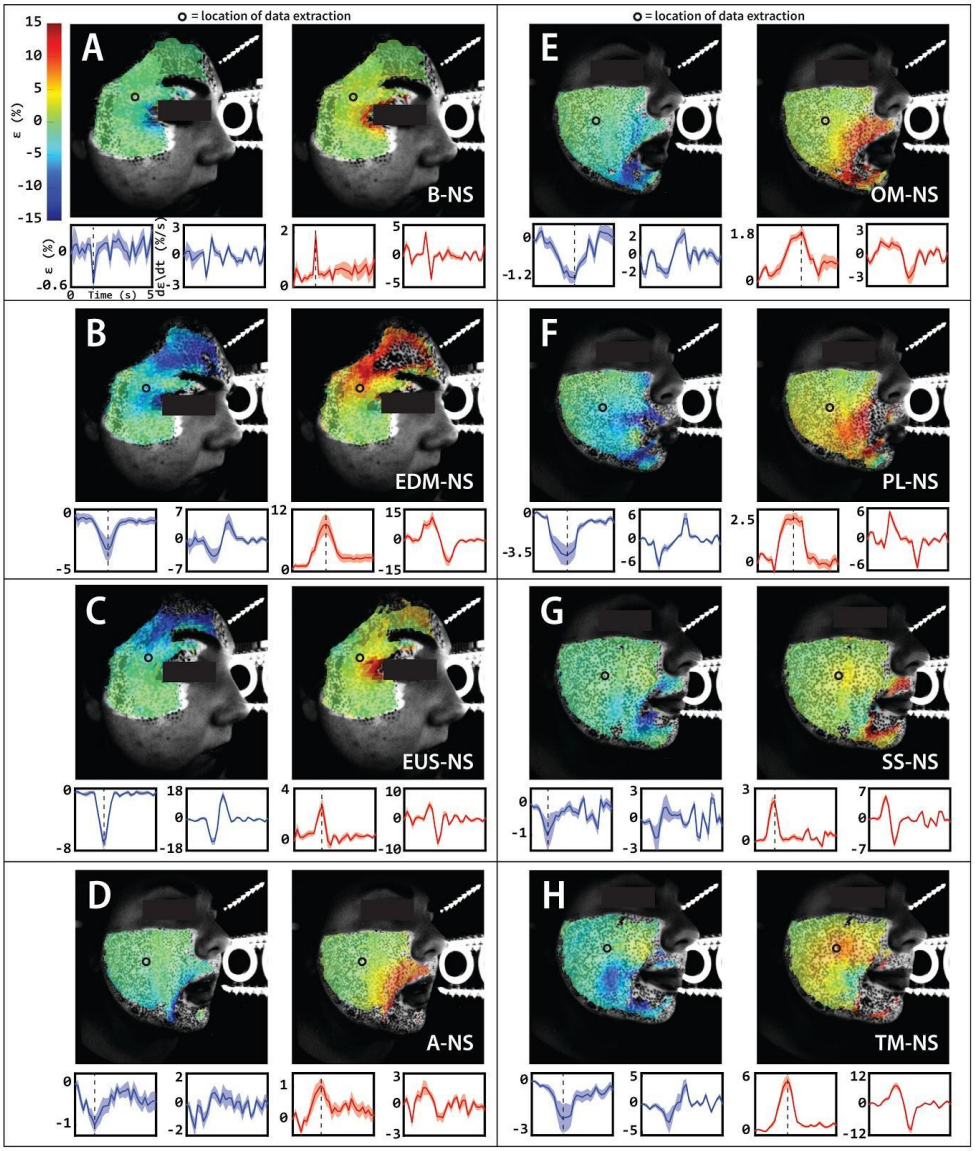

Fig. S17. Representative 3D-DIC Results, Healthy Subject 1, No Sensor (NS), Motions 1-8

Photogrammetric evaluation of facial skin *in vivo* characterizes the mechanical character of human skin undergoing natural deformations. Analyses for eight of the following representative motions are shown (B = blink; EDM and EDS = eyebrow down medium magnitude and small magnitude, respectively; EUM and EUS = eyebrow up medium magnitude and small magnitude, respectively; A, E, I, O, U = saying vowel “A,” “E,” “I,” “O,” and “U,” respectively; OM = open mouth; PL = pursed lips, SM and SS = smile medium magnitude and small magnitude,

respectively; TM and TS = twitch medium magnitude and small magnitude, respectively). Images depict strain maps in which strains calculated via DIC algorithms run on two pairs of cameras are overlaid on the raw images captured by PG. The strain maps shown come from the frame in which peak strain occurred in the area of the sensor (S) or in the area of the skin directly underneath where the sensor was placed (NS). The strain scale bar (%) applying to all strain maps is given in the top left corner. Line drawings atop the strain maps from DIC trials with the sensor indicate the location of cFaCES (solid box) and its four active elements (solid circles) and Tegaderm® tape (dashed). The sensing element or area of the skin from which voltage data and/or atop which strain data was collected is marked by the red circle. For NS cases, the area from which strain data was collected is marked by a black circle. For each of the displayed cells, the left-side images and blue graphs (left: strain, ϵ (%), right: strain rate $\frac{\partial \epsilon}{\partial t}$ (%/s)) display results for minimal principal strain, and the right side the same for maximal principal strain (red graphs). For each five-second period, averaged strain across the DIC-generated triangles ($n \geq 12$) corresponding to the sensing element from which voltage is measured is represented as a solid line, and the shaded band indicates standard deviation. Note that the strain on the top layer of the sensor Tegaderm® tape is not exactly the same as that directly experienced by the piezoelectric layer, but the trend is expected to be the same. The peak strain is denoted in each of the strain graphs by the dashed black line. Voltage (top) and voltage rate (bottom) graphs (black) display the output of the denoted sensing element. Results of five repeats of the same motion for each subject and each motion are available in Figs. S29-122. Axes titles and units as given in A) are the same for all like graphs. Strain maps and graphs include only triangles for which the correlation coefficient was lower than 0.4. The time axis for all subgraphs are the same.

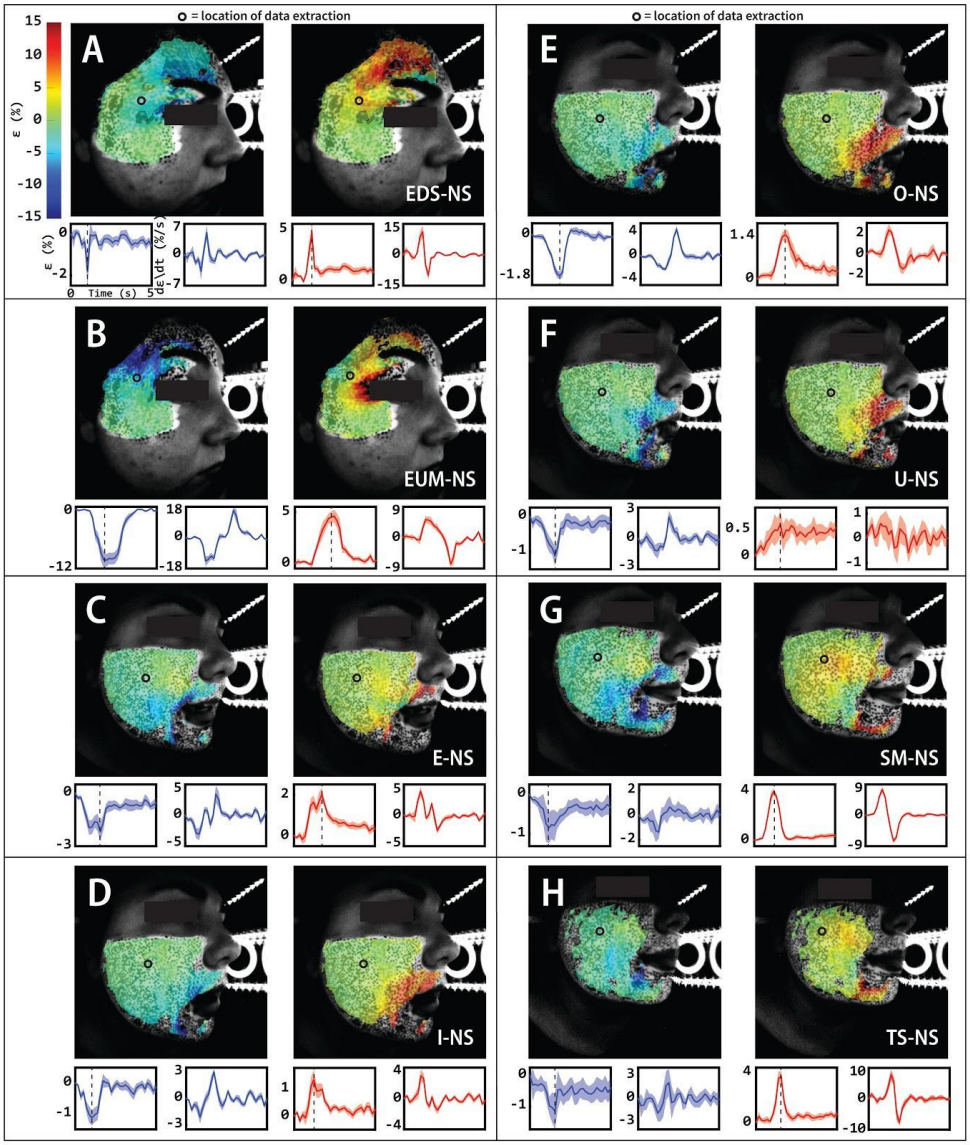

Fig. S18. Representative 3D-DIC Results, Healthy Subject 1, No Sensor (NS), Motions 9-16

Photogrammetric evaluation of facial skin *in vivo* characterizes the mechanical character of human skin undergoing natural deformations. Analyses for eight of the following representative motions are shown (B = blink; EDM and EDS = eyebrow down medium magnitude and small magnitude, respectively; EUM and EUS = eyebrow up medium magnitude and small magnitude, respectively; A, E, I, O, U = saying vowel “A,” “E,” “I,” “O,” and “U,” respectively; OM = open mouth; PL = pursed lips, SM and SS = smile medium magnitude and small magnitude,

respectively; TM and TS = twitch medium magnitude and small magnitude, respectively). Images depict strain maps in which strains calculated via DIC algorithms run on two pairs of cameras are overlaid on the raw images captured by PG. The strain maps shown come from the frame in which peak strain occurred in the area of the sensor (S) or in the area of the skin directly underneath where the sensor was placed (NS). The strain scale bar (%) applying to all strain maps is given in the top left corner. Line drawings atop the strain maps from DIC trials with the sensor indicate the location of cFaCES (solid box) and its four active elements (solid circles) and Tegaderm® tape (dashed). The sensing element or area of the skin from which voltage data and/or atop which strain data was collected is marked by the red circle. For NS cases, the area from which strain data was collected is marked by a black circle. For each of the displayed cells, the left-side images and blue graphs (left: strain, ϵ (%), right: strain rate $\frac{\partial \epsilon}{\partial t}$ (%/s)) display results for minimal principal strain, and the right side the same for maximal principal strain (red graphs). For each five-second period, averaged strain across the DIC-generated triangles ($n \geq 12$) corresponding to the sensing element from which voltage is measured is represented as a solid line, and the shaded band indicates standard deviation. Note that the strain on the top layer of the sensor Tegaderm® tape is not exactly the same as that directly experienced by the piezoelectric layer, but the trend is expected to be the same . The peak strain is denoted in each of the strain graphs by the dashed black line. Voltage (top) and voltage rate (bottom) graphs (black) display the output of the denoted sensing element. Results of five repeats of the same motion for each subject and each motion are available in Figs. S29-122. Axes titles and units as given in A) are the same for all like graphs. Strain maps and graphs include only triangles for which the correlation coefficient was lower than 0.4. The time axis for all subgraphs are the same.

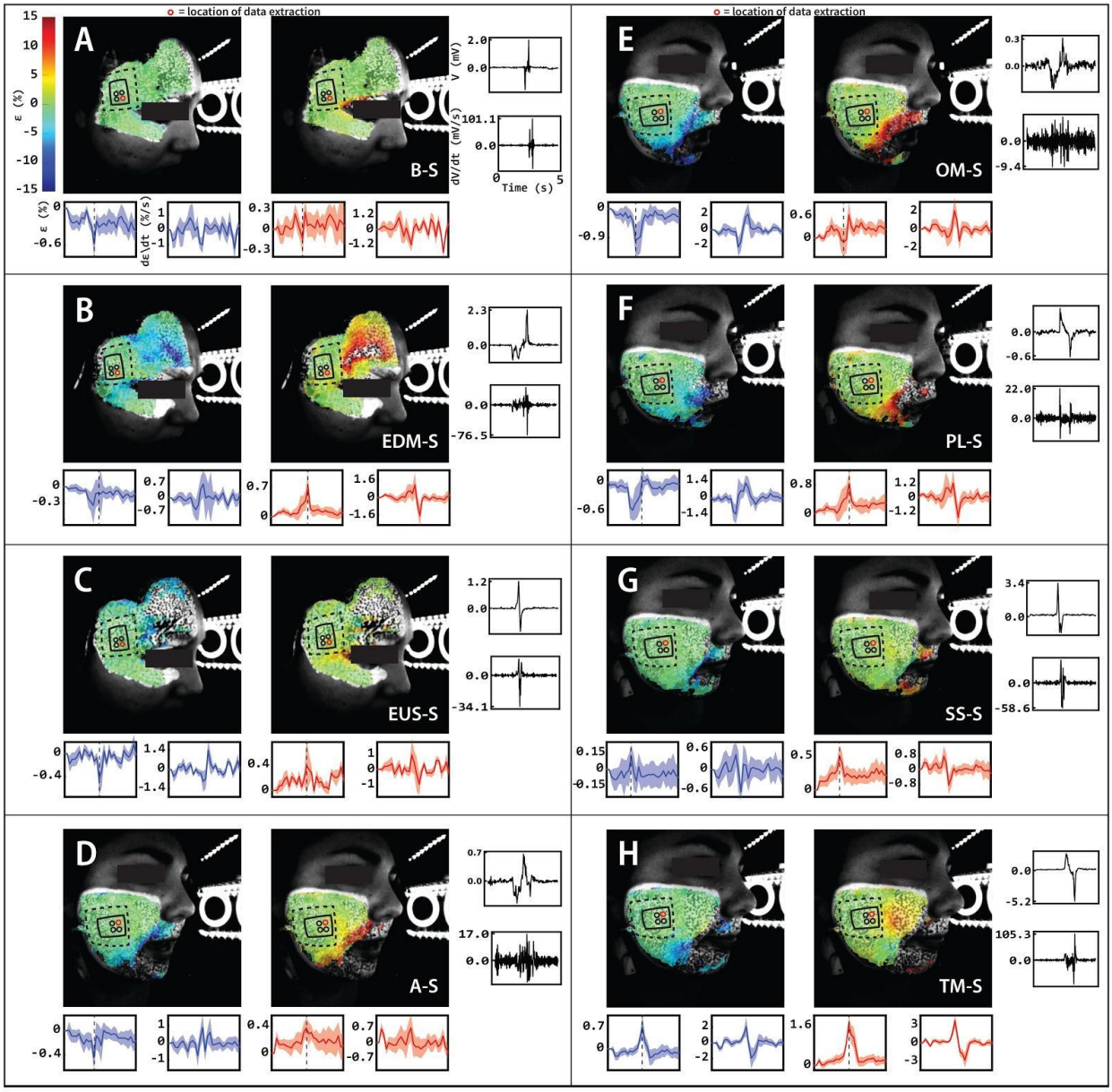

Fig. S19. Representative 3D-DIC Results, Healthy Subject 1, Sensor (S), Motions 1-8

Photogrammetric evaluation of facial skin *in vivo* characterizes the mechanical character of human skin undergoing natural deformations. Analyses for eight of the following representative motions are shown (B = blink; EDM and EDS = eyebrow down medium magnitude and small magnitude, respectively; EUM and EUS = eyebrow up medium magnitude and small magnitude, respectively; A, E, I, O, U = saying vowel “A,” “E,” “I,” “O,” and “U,” respectively; OM = open

mouth; PL = pursed lips, SM and SS = smile medium magnitude and small magnitude, respectively; TM and TS = twitch medium magnitude and small magnitude, respectively). Images depict strain maps in which strains calculated via DIC algorithms run on two pairs of cameras are overlaid on the raw images captured by PG. The strain maps shown come from the frame in which peak strain occurred in the area of the sensor (S) or in the area of the skin directly underneath where the sensor was placed (NS). The strain scale bar (%) applying to all strain maps is given in the top left corner. Line drawings atop the strain maps from DIC trials with the sensor indicate the location of cFaCES (solid box) and its four active elements (solid circles) and Tegaderm® tape (dashed). The sensing element or area of the skin from which voltage data and/or atop which strain data was collected is marked by the red circle. For NS cases, the area from which strain data was collected is marked by a black circle. For each of the displayed cells, the left-side images and blue graphs (left: strain, ϵ (%), right: strain rate $\frac{\partial \epsilon}{\partial t}$ (%/s)) display results for minimal principal strain, and the right side the same for maximal principal strain (red graphs). For each five-second period, averaged strain across the DIC-generated triangles ($n \geq 12$) corresponding to the sensing element from which voltage is measured is represented as a solid line, and the shaded band indicates standard deviation. Note that the strain on the top layer of the sensor Tegaderm® tape is not exactly the same as that directly experienced by the piezoelectric layer, but the trend is expected to be the same . The peak strain is denoted in each of the strain graphs by the dashed black line. Voltage (top) and voltage rate (bottom) graphs (black) display the output of the denoted sensing element. Results of five repeats of the same motion for each subject and each motion are available in Figs. S29-122. Axes titles and units as given in A) are the same for all like graphs. Strain maps and graphs include only triangles for which the correlation coefficient was lower than 0.4. The time axis for all subgraphs are the same.

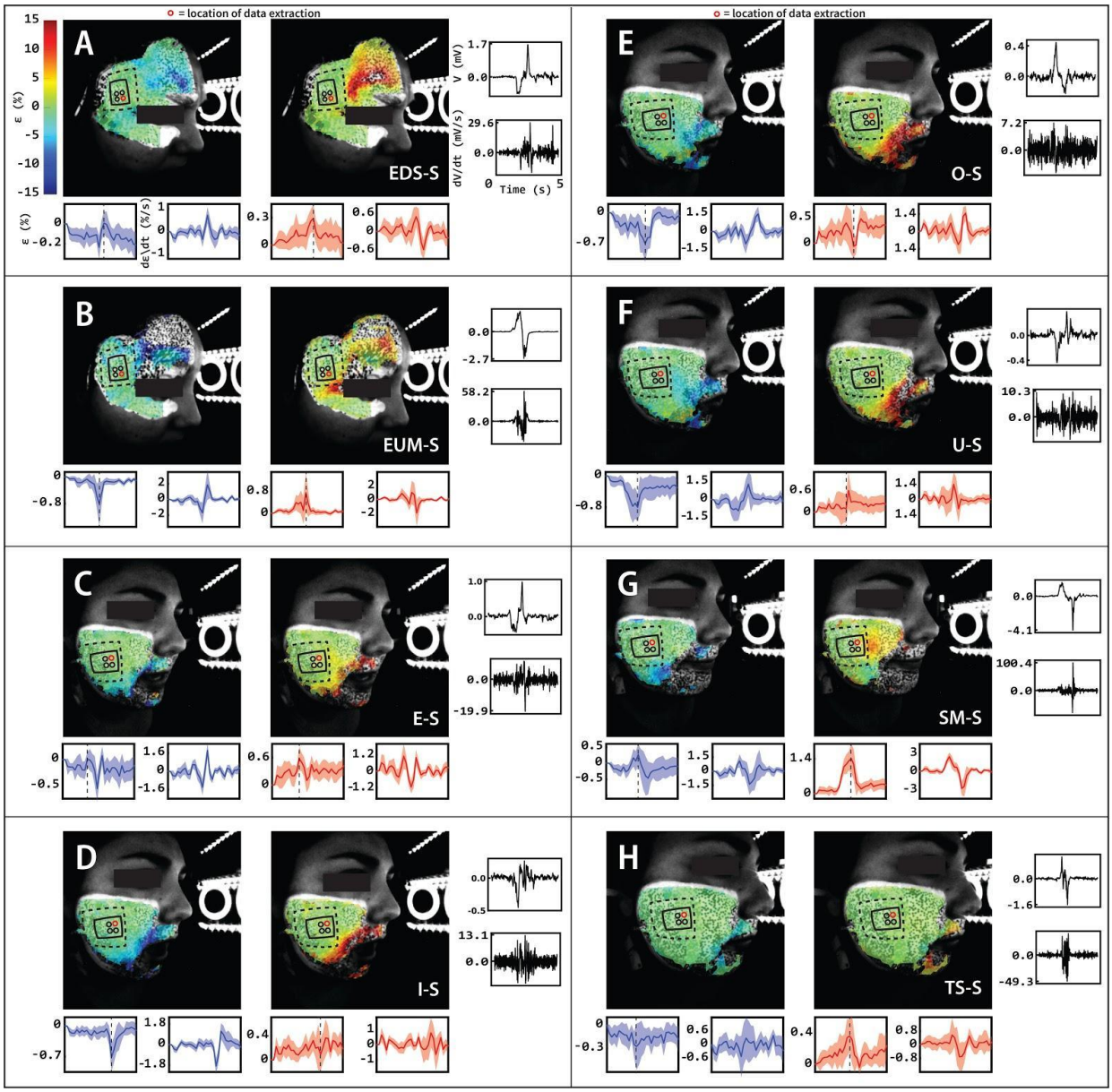

Fig. S20. Representative 3D-DIC Results, Healthy Subject 1, Sensor (S), Motions 9-16

Photogrammetric evaluation of facial skin *in vivo* characterizes the mechanical character of human skin undergoing natural deformations. Analyses for eight of the following representative motions are shown (B = blink; EDM and EDS = eyebrow down medium magnitude and small magnitude, respectively; EUM and EUS = eyebrow up medium magnitude and small magnitude, respectively; A, E, I, O, U = saying vowel “A,” “E,” “I,” “O,” and “U,” respectively; OM = open

mouth; PL = pursed lips, SM and SS = smile medium magnitude and small magnitude, respectively; TM and TS = twitch medium magnitude and small magnitude, respectively). Images depict strain maps in which strains calculated via DIC algorithms run on two pairs of cameras are overlaid on the raw images captured by PG. The strain maps shown come from the frame in which peak strain occurred in the area of the sensor (S) or in the area of the skin directly underneath where the sensor was placed (NS). The strain scale bar (%) applying to all strain maps is given in the top left corner. Line drawings atop the strain maps from DIC trials with the sensor indicate the location of cFaCES (solid box) and its four active elements (solid circles) and Tegaderm® tape (dashed). The sensing element or area of the skin from which voltage data and/or atop which strain data was collected is marked by the red circle. For NS cases, the area from which strain data was collected is marked by a black circle. For each of the displayed cells, the left-side images and blue graphs (left: strain, ϵ (%), right: strain rate $\frac{\partial \epsilon}{\partial t}$ (%/s)) display results for minimal principal strain, and the right side the same for maximal principal strain (red graphs). For each five-second period, averaged strain across the DIC-generated triangles ($n \geq 12$) corresponding to the sensing element from which voltage is measured is represented as a solid line, and the shaded band indicates standard deviation. Note that the strain on the top layer of the sensor Tegaderm® tape is not exactly the same as that directly experienced by the piezoelectric layer, but the trend is expected to be the same . The peak strain is denoted in each of the strain graphs by the dashed black line. Voltage (top) and voltage rate (bottom) graphs (black) display the output of the denoted sensing element. Results of five repeats of the same motion for each subject and each motion are available in Figs. S29-122. Axes titles and units as given in A) are the same for all like graphs. Strain maps and graphs include only triangles for which the correlation coefficient was lower than 0.4. The time axis for all subgraphs are the same.

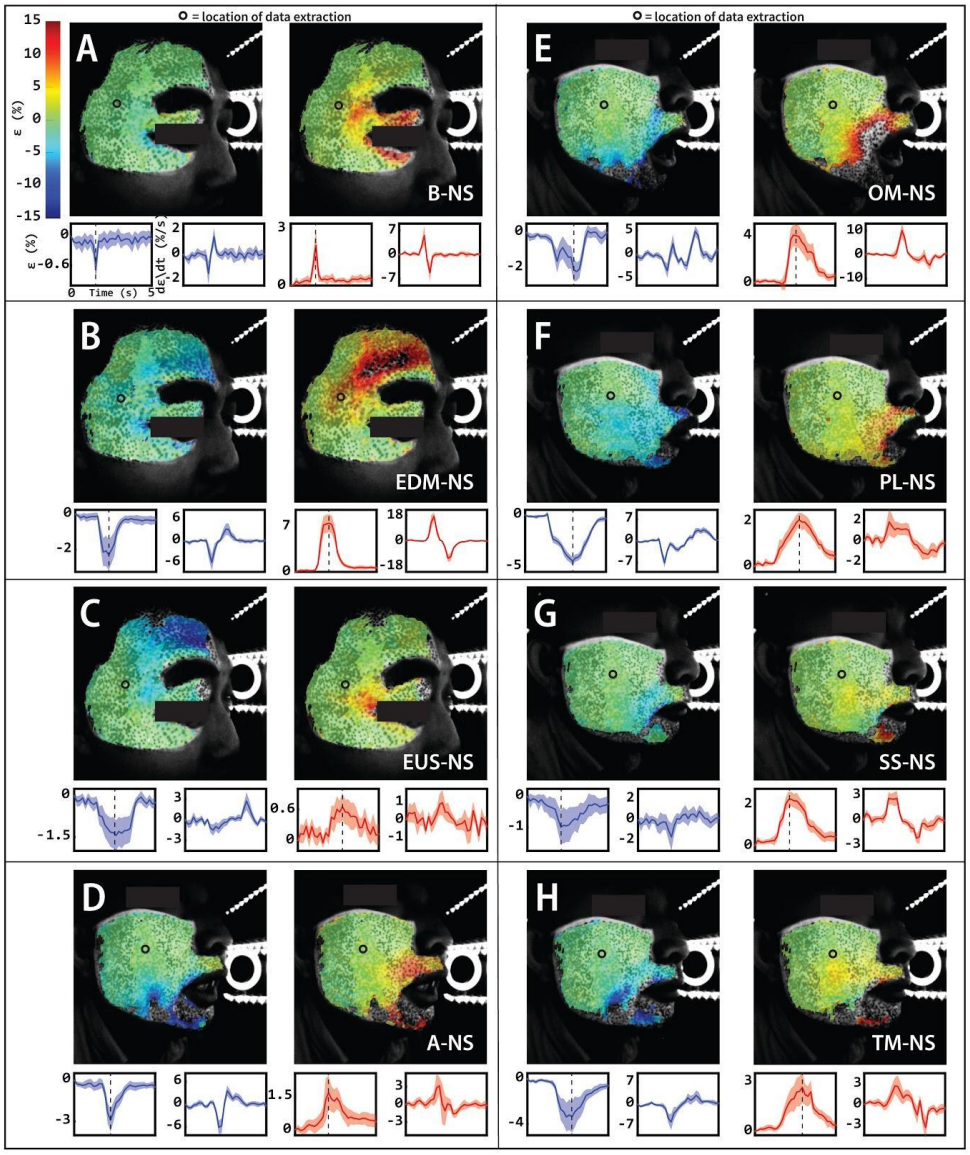

Fig. S21. Representative 3D-DIC Results, Healthy Subject 2, No Sensor (NS), Motions 1-8

Photogrammetric evaluation of facial skin *in vivo* characterizes the mechanical character of human skin undergoing natural deformations. Analyses for eight of the following representative motions are shown (B = blink; EDM and EDS = eyebrow down medium magnitude and small magnitude, respectively; EUM and EUS = eyebrow up medium magnitude and small magnitude, respectively; A, E, I, O, U = saying vowel “A,” “E,” “I,” “O,” and “U,” respectively; OM = open mouth; PL = pursed lips, SM and SS = smile medium magnitude and small magnitude,

respectively; TM and TS = twitch medium magnitude and small magnitude, respectively). Images depict strain maps in which strains calculated via DIC algorithms run on two pairs of cameras are overlaid on the raw images captured by PG. The strain maps shown come from the frame in which peak strain occurred in the area of the sensor (S) or in the area of the skin directly underneath where the sensor was placed (NS). The strain scale bar (%) applying to all strain maps is given in the top left corner. Line drawings atop the strain maps from DIC trials with the sensor indicate the location of cFaCES (solid box) and its four active elements (solid circles) and Tegaderm® tape (dashed). The sensing element or area of the skin from which voltage data and/or atop which strain data was collected is marked by the red circle. For NS cases, the area from which strain data was collected is marked by a black circle. For each of the displayed cells, the left-side images and blue graphs (left: strain, ϵ (%), right: strain rate $\frac{\partial \epsilon}{\partial t}$ (%/s)) display results for minimal principal strain, and the right side the same for maximal principal strain (red graphs). For each five-second period, averaged strain across the DIC-generated triangles ($n \geq 12$) corresponding to the sensing element from which voltage is measured is represented as a solid line, and the shaded band indicates standard deviation. Note that the strain on the top layer of the sensor Tegaderm® tape is not exactly the same as that directly experienced by the piezoelectric layer, but the trend is expected to be the same . The peak strain is denoted in each of the strain graphs by the dashed black line. Voltage (top) and voltage rate (bottom) graphs (black) display the output of the denoted sensing element. Results of five repeats of the same motion for each subject and each motion are available in Figs. S29-122. Axes titles and units as given in A) are the same for all like graphs. Strain maps and graphs include only triangles for which the correlation coefficient was lower than 0.4. The time axis for all subgraphs are the same.

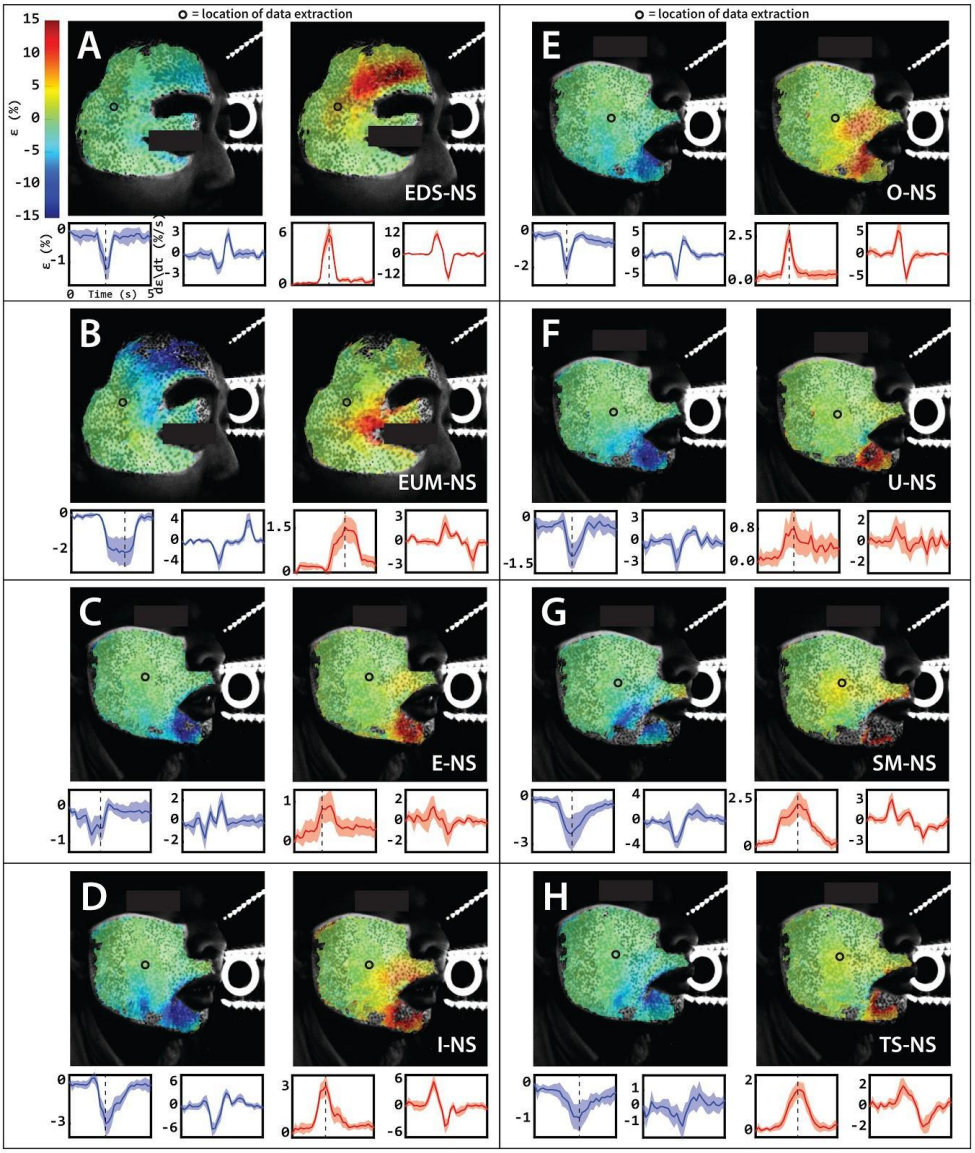

Fig. S22. Representative 3D-DIC Results, Healthy Subject 2, No Sensor (NS), Motions 9-16

Photogrammetric evaluation of facial skin *in vivo* characterizes the mechanical character of human skin undergoing natural deformations. Analyses for eight of the following representative motions are shown (B = blink; EDM and EDS = eyebrow down medium magnitude and small magnitude, respectively; EUM and EUS = eyebrow up medium magnitude and small magnitude, respectively; A, E, I, O, U = saying vowel “A,” “E,” “I,” “O,” and “U,” respectively; OM = open mouth; PL = pursed lips, SM and SS = smile medium magnitude and small magnitude,

respectively; TM and TS = twitch medium magnitude and small magnitude, respectively). Images depict strain maps in which strains calculated via DIC algorithms run on two pairs of cameras are overlaid on the raw images captured by PG. The strain maps shown come from the frame in which peak strain occurred in the area of the sensor (S) or in the area of the skin directly underneath where the sensor was placed (NS). The strain scale bar (%) applying to all strain maps is given in the top left corner. Line drawings atop the strain maps from DIC trials with the sensor indicate the location of cFaCES (solid box) and its four active elements (solid circles) and Tegaderm® tape (dashed). The sensing element or area of the skin from which voltage data and/or atop which strain data was collected is marked by the red circle. For NS cases, the area from which strain data was collected is marked by a black circle. For each of the displayed cells, the left-side images and blue graphs (left: strain, ϵ (%), right: strain rate $\frac{\partial \epsilon}{\partial t}$ (%/s)) display results for minimal principal strain, and the right side the same for maximal principal strain (red graphs). For each five-second period, averaged strain across the DIC-generated triangles ($n \geq 12$) corresponding to the sensing element from which voltage is measured is represented as a solid line, and the shaded band indicates standard deviation. Note that the strain on the top layer of the sensor Tegaderm® tape is not exactly the same as that directly experienced by the piezoelectric layer, but the trend is expected to be the same . The peak strain is denoted in each of the strain graphs by the dashed black line. Voltage (top) and voltage rate (bottom) graphs (black) display the output of the denoted sensing element. Results of five repeats of the same motion for each subject and each motion are available in Figs. S29-122. Axes titles and units as given in A) are the same for all like graphs. Strain maps and graphs include only triangles for which the correlation coefficient was lower than 0.4. The time axis for all subgraphs are the same.

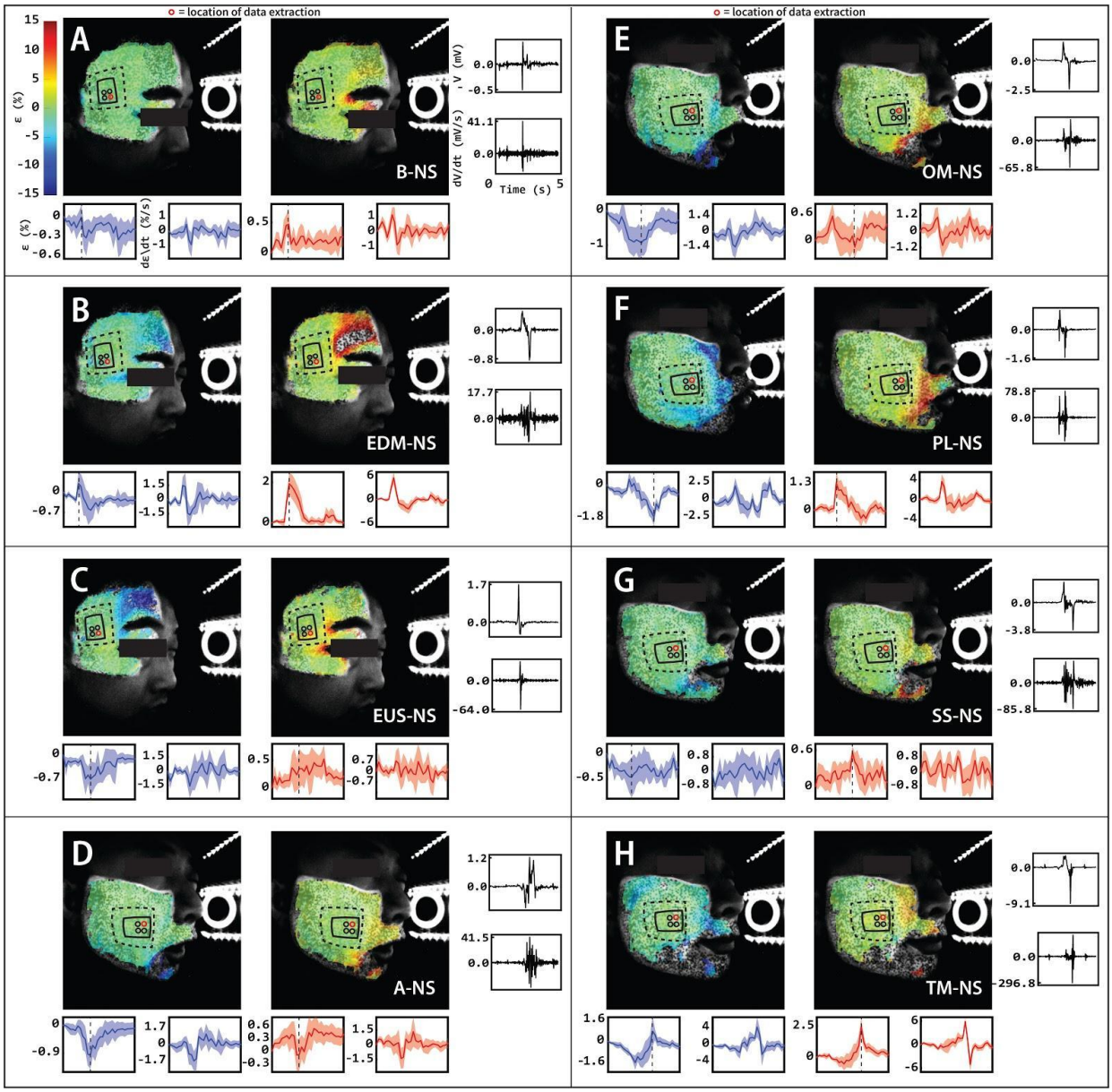

Fig. S23. Representative 3D-DIC Results, Healthy Subject 2, Sensor (S), Motions 1-8

Photogrammetric evaluation of facial skin *in vivo* characterizes the mechanical character of human skin undergoing natural deformations. Analyses for eight of the following representative motions are shown (B = blink; EDM and EDS = eyebrow down medium magnitude and small magnitude, respectively; EUM and EUS = eyebrow up medium magnitude and small magnitude, respectively; A, E, I, O, U = saying vowel “A,” “E,” “I,” “O,” and “U,” respectively; OM = open

mouth; PL = pursed lips, SM and SS = smile medium magnitude and small magnitude, respectively; TM and TS = twitch medium magnitude and small magnitude, respectively). Images depict strain maps in which strains calculated via DIC algorithms run on two pairs of cameras are overlaid on the raw images captured by PG. The strain maps shown come from the frame in which peak strain occurred in the area of the sensor (S) or in the area of the skin directly underneath where the sensor was placed (NS). The strain scale bar (%) applying to all strain maps is given in the top left corner. Line drawings atop the strain maps from DIC trials with the sensor indicate the location of cFaCES (solid box) and its four active elements (solid circles) and Tegaderm® tape (dashed). The sensing element or area of the skin from which voltage data and/or atop which strain data was collected is marked by the red circle. For NS cases, the area from which strain data was collected is marked by a black circle. For each of the displayed cells, the left-side images and blue graphs (left: strain, ϵ (%), right: strain rate $\frac{\partial \epsilon}{\partial t}$ (%/s)) display results for minimal principal strain, and the right side the same for maximal principal strain (red graphs). For each five-second period, averaged strain across the DIC-generated triangles ($n \geq 12$) corresponding to the sensing element from which voltage is measured is represented as a solid line, and the shaded band indicates standard deviation. Note that the strain on the top layer of the sensor Tegaderm® tape is not exactly the same as that directly experienced by the piezoelectric layer, but the trend is expected to be the same . The peak strain is denoted in each of the strain graphs by the dashed black line. Voltage (top) and voltage rate (bottom) graphs (black) display the output of the denoted sensing element. Results of five repeats of the same motion for each subject and each motion are available in Figs. S29-122. Axes titles and units as given in A) are the same for all like graphs. Strain maps and graphs include only triangles for which the correlation coefficient was lower than 0.4. The time axis for all subgraphs are the same.

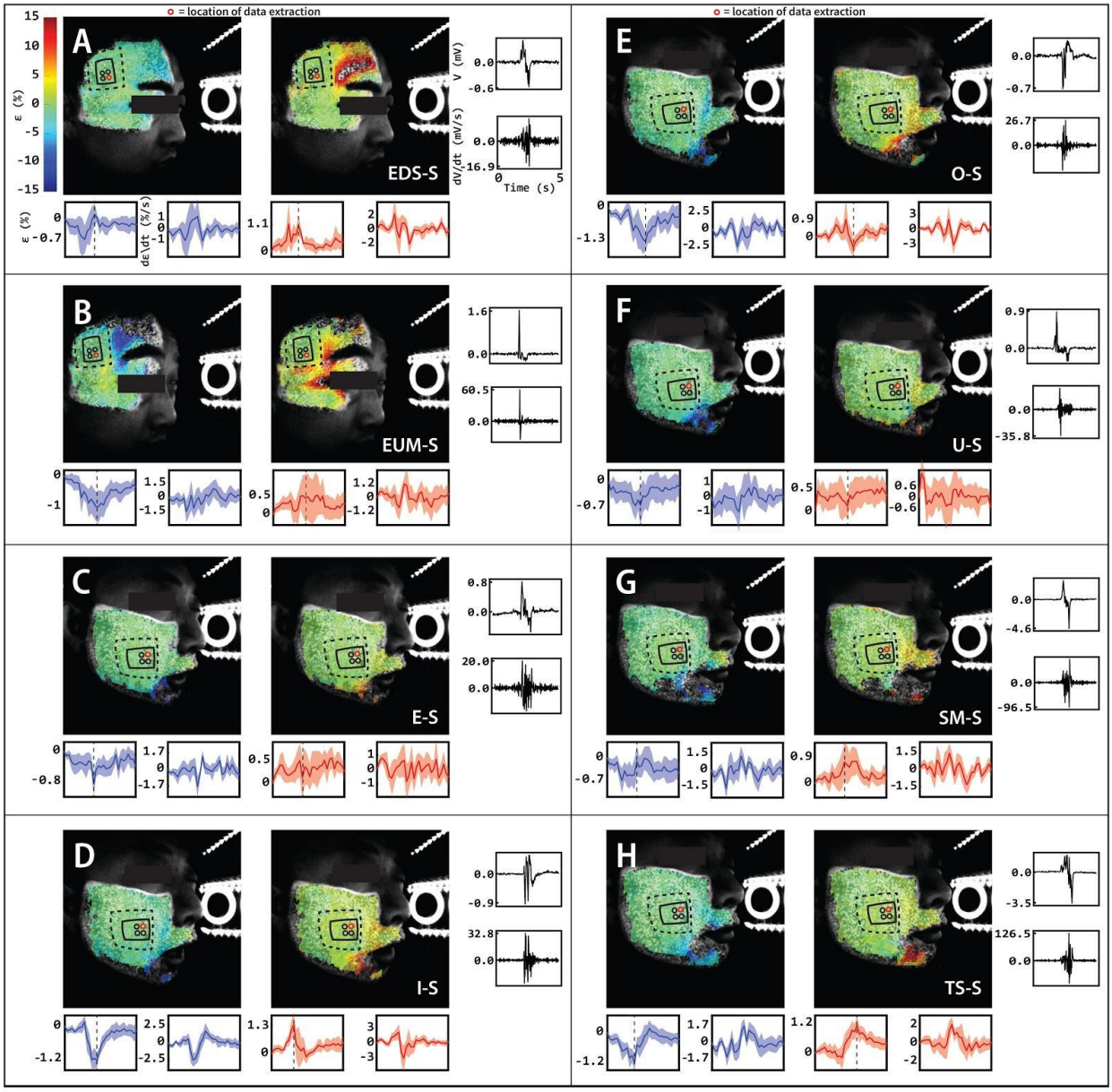

Fig. S24. Representative DIC Results, Healthy Subject 2, Sensor (S), Motions 9-16

Photogrammetric evaluation of facial skin *in vivo* characterizes the mechanical character of human skin undergoing natural deformations. Analyses for eight of the following representative motions are shown (B = blink; EDM and EDS = eyebrow down medium magnitude and small magnitude, respectively; EUM and EUS = eyebrow up medium magnitude and small magnitude, respectively; A, E, I, O, U = saying vowel “A,” “E,” “I,” “O,” and “U,” respectively; OM = open mouth; PL = pursed lips, SM and SS = smile medium magnitude and small magnitude,

respectively; TM and TS = twitch medium magnitude and small magnitude, respectively). Images depict strain maps in which strains calculated via DIC algorithms run on two pairs of cameras are overlaid on the raw images captured by PG. The strain maps shown come from the frame in which peak strain occurred in the area of the sensor (S) or in the area of the skin directly underneath where the sensor was placed (NS). The strain scale bar (%) applying to all strain maps is given in the top left corner. Line drawings atop the strain maps from DIC trials with the sensor indicate the location of cFaCES (solid box) and its four active elements (solid circles) and Tegaderm® tape (dashed). The sensing element or area of the skin from which voltage data and/or atop which strain data was collected is marked by the red circle. For NS cases, the area from which strain data was collected is marked by a black circle. For each of the displayed cells, the left-side images and blue graphs (left: strain, ϵ (%), right: strain rate $\frac{\partial \epsilon}{\partial t}$ (%/s)) display results for minimal principal strain, and the right side the same for maximal principal strain (red graphs). For each five-second period, averaged strain across the DIC-generated triangles ($n \geq 12$) corresponding to the sensing element from which voltage is measured is represented as a solid line, and the shaded band indicates standard deviation. Note that the strain on the top layer of the sensor Tegaderm® tape is not exactly the same as that directly experienced by the piezoelectric layer, but the trend is expected to be the same . The peak strain is denoted in each of the strain graphs by the dashed black line. Voltage (top) and voltage rate (bottom) graphs (black) display the output of the denoted sensing element. Results of five repeats of the same motion for each subject and each motion are available in Figs. S29-122. Axes titles and units as given in A) are the same for all like graphs. Strain maps and graphs include only triangles for which the correlation coefficient was lower than 0.4. The time axis for all subgraphs are the same.

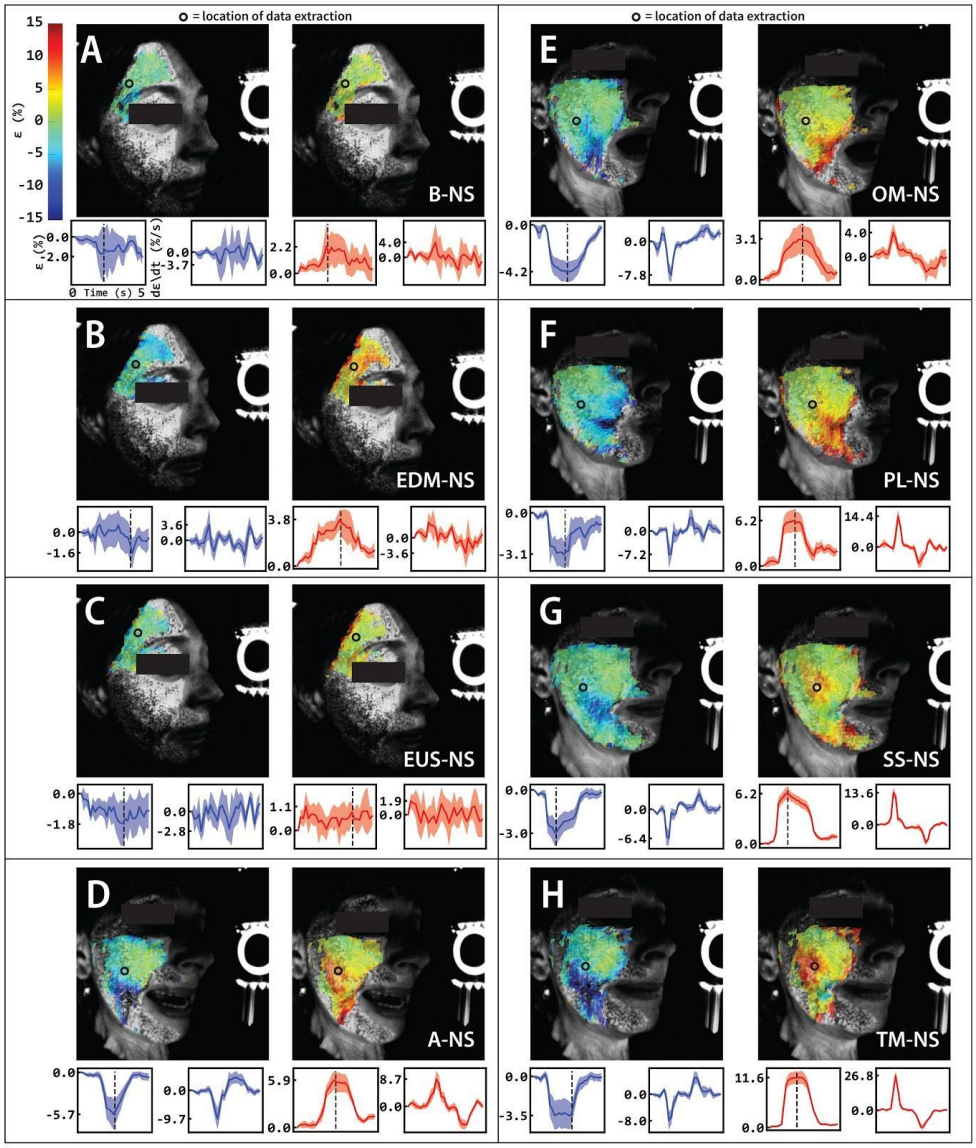

Fig. S25. Representative 3D-DIC Results, ALS Subject 1, No Sensor (NS), Motions 1-8

Photogrammetric evaluation of facial skin *in vivo* characterizes the mechanical character of human skin undergoing natural deformations. Analyses for eight of the following representative motions are shown (B = blink; EDM and EDS = eyebrow down medium magnitude and small magnitude, respectively; EUM and EUS = eyebrow up medium magnitude and small magnitude, respectively; A, E, I, O, U = saying vowel “A,” “E,” “I,” “O,” and “U,” respectively; OM = open mouth; PL = pursed lips, SM and SS = smile medium magnitude and small magnitude,

respectively; TM and TS = twitch medium magnitude and small magnitude, respectively). Images depict strain maps in which strains calculated via DIC algorithms run on two pairs of cameras are overlaid on the raw images captured by PG. The strain maps shown come from the frame in which peak strain occurred in the area of the sensor (S) or in the area of the skin directly underneath where the sensor was placed (NS). The strain scale bar (%) applying to all strain maps is given in the top left corner. Line drawings atop the strain maps from DIC trials with the sensor indicate the location of cFaCES (solid box) and its four active elements (solid circles) and Tegaderm® tape (dashed). The sensing element or area of the skin from which voltage data and/or atop which strain data was collected is marked by the red circle. For NS cases, the area from which strain data was collected is marked by a black circle. For each of the displayed cells, the left-side images and blue graphs (left: strain, ϵ (%), right: strain rate $\frac{\partial \epsilon}{\partial t}$ (%/s)) display results for minimal principal strain, and the right side the same for maximal principal strain (red graphs). For each five-second period, averaged strain across the DIC-generated triangles ($n \geq 9$) corresponding to the sensing element from which voltage is measured is represented as a solid line, and the shaded band indicates standard deviation. Note that the strain on the top layer of the sensor Tegaderm® tape is not exactly the same as that directly experienced by the piezoelectric layer, but the trend is expected to be the same . The peak strain is denoted in each of the strain graphs by the dashed black line. Voltage (top) and voltage rate (bottom) graphs (black) display the output of the denoted sensing element. Results of five repeats of the same motion for each subject and each motion are available in Figs. S29-122. Axes titles and units as given in A) are the same for all like graphs. Strain maps and graphs include only triangles for which the correlation coefficient was lower than 0.4. The time axis for all subgraphs are the same.

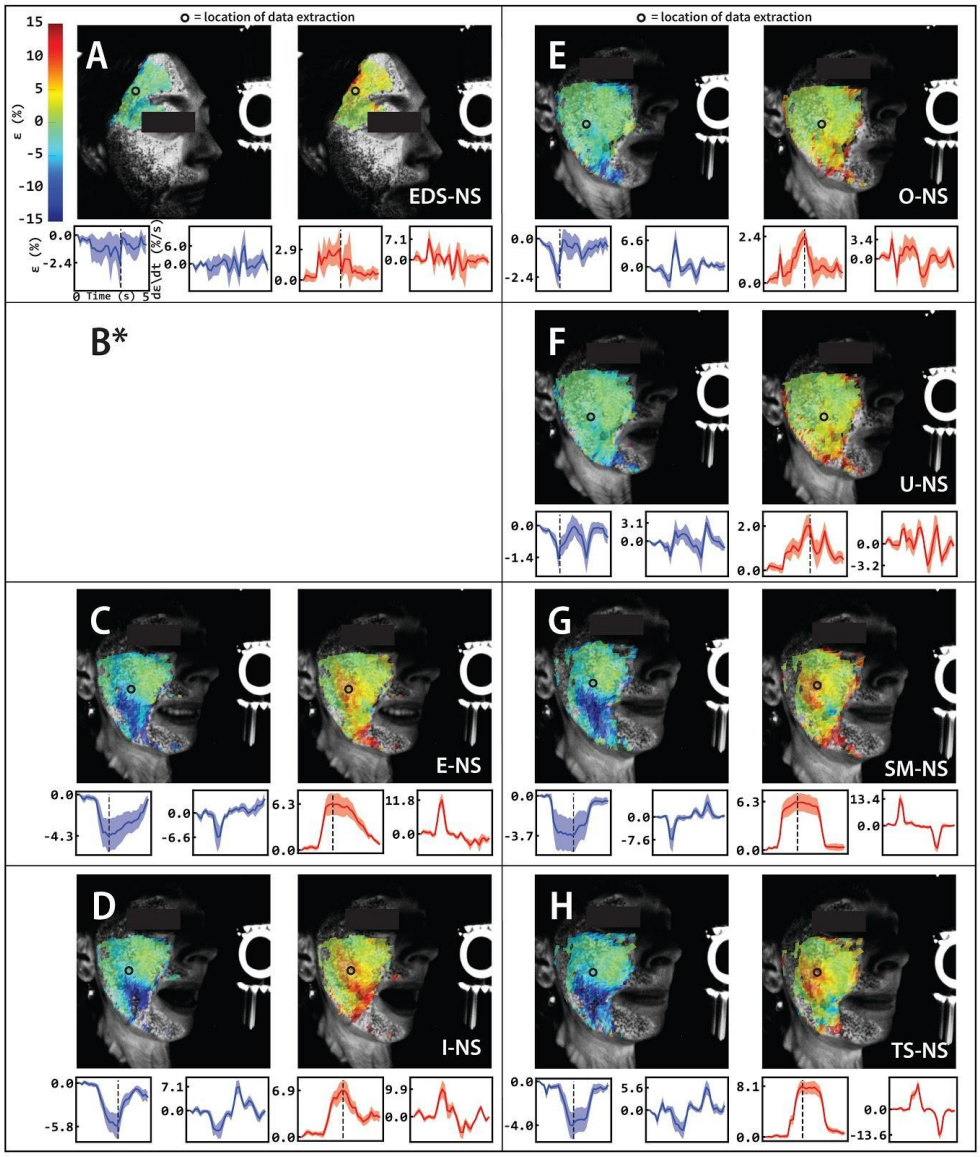

Fig. S26. Representative 3D-DIC Results, ALS Subject 1, No Sensor (NS), Motions 9-16. *The subject could not perform the motion EUM.

Photogrammetric evaluation of facial skin *in vivo* characterizes the mechanical character of human skin undergoing natural deformations. Analyses for eight of the following representative motions are shown (B = blink; EDM and EDS = eyebrow down medium magnitude and small magnitude, respectively; EUM and EUS = eyebrow up medium magnitude and small magnitude, respectively; A, E, I, O, U = saying vowel “A,” “E,” “I,” “O,” and “U,” respectively; OM = open mouth; PL = pursed lips, SM and SS = smile medium magnitude and small magnitude,

respectively; TM and TS = twitch medium magnitude and small magnitude, respectively). Images depict strain maps in which strains calculated via DIC algorithms run on two pairs of cameras are overlaid on the raw images captured by PG. The strain maps shown come from the frame in which peak strain occurred in the area of the sensor (S) or in the area of the skin directly underneath where the sensor was placed (NS). The strain scale bar (%) applying to all strain maps is given in the top left corner. Line drawings atop the strain maps from DIC trials with the sensor indicate the location of cFaCES (solid box) and its four active elements (solid circles) and Tegaderm® tape (dashed). The sensing element or area of the skin from which voltage data and/or atop which strain data was collected is marked by the red circle. For NS cases, the area from which strain data was collected is marked by a black circle. For each of the displayed cells, the left-side images and blue graphs (left: strain, ϵ (%), right: strain rate $\frac{\partial \epsilon}{\partial t}$ (%/s)) display results for minimal principal strain, and the right side the same for maximal principal strain (red graphs). For each five-second period, averaged strain across the DIC-generated triangles ($n \geq 9$) corresponding to the sensing element from which voltage is measured is represented as a solid line, and the shaded band indicates standard deviation. Note that the strain on the top layer of the sensor Tegaderm® tape is not exactly the same as that directly experienced by the piezoelectric layer, but the trend is expected to be the same . The peak strain is denoted in each of the strain graphs by the dashed black line. Voltage (top) and voltage rate (bottom) graphs (black) display the output of the denoted sensing element. Results of five repeats of the same motion for each subject and each motion are available in Figs. S29-122. Axes titles and units as given in A) are the same for all like graphs. Strain maps and graphs include only triangles for which the correlation coefficient was lower than 0.4. The time axis for all subgraphs are the same.

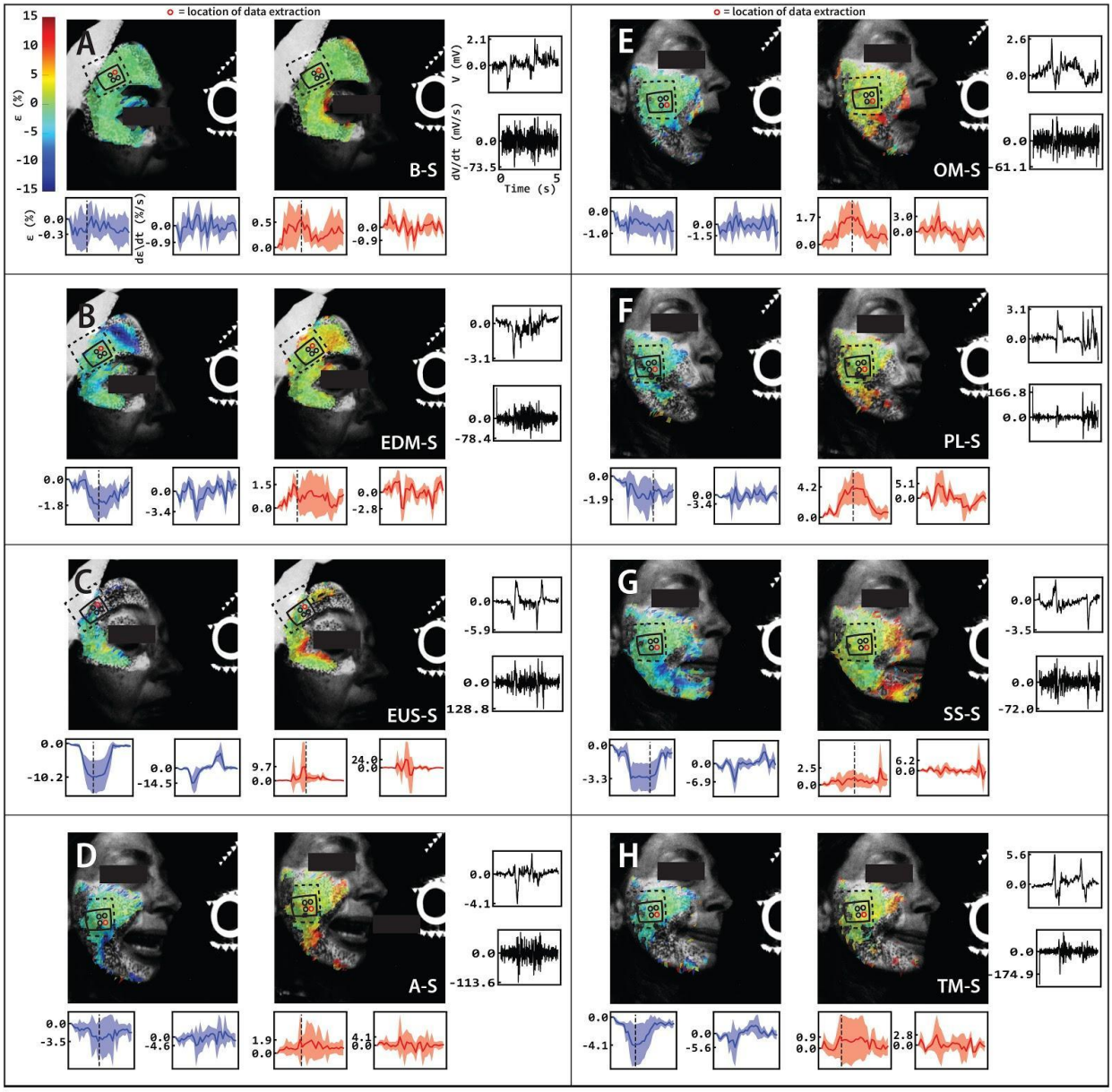

Fig. S27. Representative 3D-DIC Results, ALS Subject 1, Sensor (S), Motions 1-8

Photogrammetric evaluation of facial skin *in vivo* characterizes the mechanical character of human skin undergoing natural deformations. Analyses for eight of the following representative motions are shown (B = blink; EDM and EDS = eyebrow down medium magnitude and small magnitude, respectively; EUM and EUS = eyebrow up medium magnitude and small magnitude, respectively; A, E, I, O, U = saying vowel “A,” “E,” “I,” “O,” and “U,” respectively; OM = open mouth; PL = pursed lips, SM and SS = smile medium magnitude and small magnitude,

respectively; TM and TS = twitch medium magnitude and small magnitude, respectively). Images depict strain maps in which strains calculated via DIC algorithms run on two pairs of cameras are overlaid on the raw images captured by PG. The strain maps shown come from the frame in which peak strain occurred in the area of the sensor (S) or in the area of the skin directly underneath where the sensor was placed (NS). The strain scale bar (%) applying to all strain maps is given in the top left corner. Line drawings atop the strain maps from DIC trials with the sensor indicate the location of cFaCES (solid box) and its four active elements (solid circles) and Tegaderm® tape (dashed). The sensing element or area of the skin from which voltage data and/or atop which strain data was collected is marked by the red circle. For NS cases, the area from which strain data was collected is marked by a black circle. For each of the displayed cells, the left-side images and blue graphs (left: strain, ϵ (%), right: strain rate $\frac{\partial \epsilon}{\partial t}$ (%/s)) display results for minimal principal strain, and the right side the same for maximal principal strain (red graphs). For each five-second period, averaged strain across the DIC-generated triangles ($n \geq 9$) corresponding to the sensing element from which voltage is measured is represented as a solid line, and the shaded band indicates standard deviation. Note that the strain on the top layer of the sensor Tegaderm® tape is not exactly the same as that directly experienced by the piezoelectric layer, but the trend is expected to be the same . The peak strain is denoted in each of the strain graphs by the dashed black line. Voltage (top) and voltage rate (bottom) graphs (black) display the output of the denoted sensing element. Results of five repeats of the same motion for each subject and each motion are available in Figs. S29-S122. Axes titles and units as given in A) are the same for all like graphs. Strain maps and graphs include only triangles for which the correlation coefficient was lower than 0.4. The time axis for all subgraphs are the same.

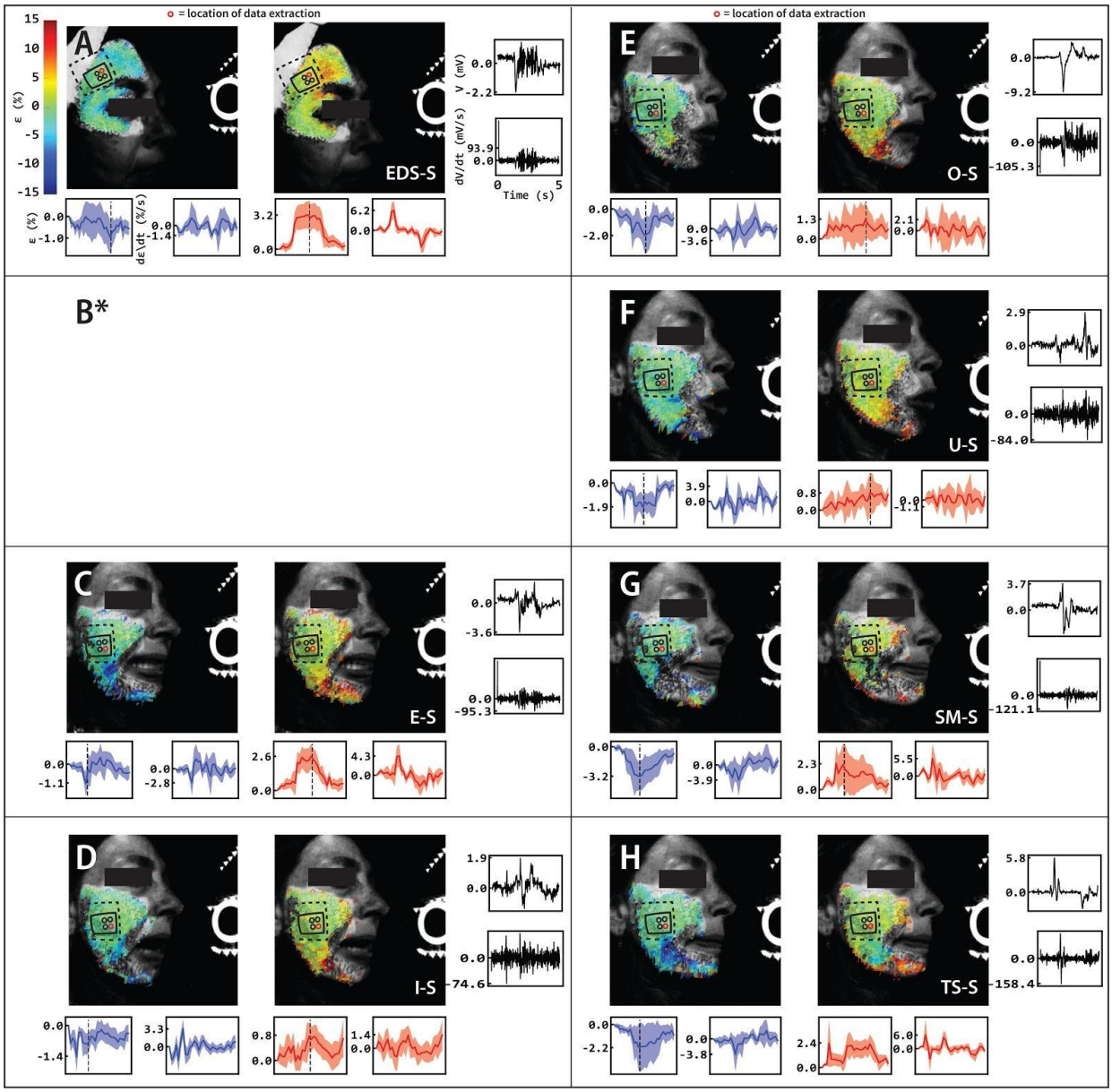

Fig. S28. Representative DIC Results, ALS Subject 1, Sensor (S), Motions 9-16.

***The subject could not perform the motion EUM.**

Photogrammetric evaluation of facial skin *in vivo* characterizes the mechanical character of human skin undergoing natural deformations. Analyses for eight of the following representative motions are shown (B = blink; EDM and EDS = eyebrow down medium magnitude and small magnitude, respectively; EUM and EUS = eyebrow up medium magnitude and small magnitude, respectively; A, E, I, O, U = saying vowel “A,” “E,” “I,” “O,” and “U,” respectively; OM = open

mouth; PL = pursed lips, SM and SS = smile medium magnitude and small magnitude, respectively; TM and TS = twitch medium magnitude and small magnitude, respectively). Images depict strain maps in which strains calculated via DIC algorithms run on two pairs of cameras are overlaid on the raw images captured by PG. The strain maps shown come from the frame in which peak strain occurred in the area of the sensor (S) or in the area of the skin directly underneath where the sensor was placed (NS). The strain scale bar (%) applying to all strain maps is given in the top left corner. Line drawings atop the strain maps from DIC trials with the sensor indicate the location of cFaCES (solid box) and its four active elements (solid circles) and Tegaderm® tape (dashed). The sensing element or area of the skin from which voltage data and/or atop which strain data was collected is marked by the red circle. For NS cases, the area from which strain data was collected is marked by a black circle. For each of the displayed cells, the left-side images and blue graphs (left: strain, ϵ (%), right: strain rate $\frac{\partial \epsilon}{\partial t}$ (%/s)) display results for minimal principal strain, and the right side the same for maximal principal strain (red graphs). For each five-second period, averaged strain across the DIC-generated triangles ($n \geq 9$) corresponding to the sensing element from which voltage is measured is represented as a solid line, and the shaded band indicates standard deviation. Note that the strain on the top layer of the sensor Tegaderm® tape is not exactly the same as that directly experienced by the piezoelectric layer, but the trend is expected to be the same . The peak strain is denoted in each of the strain graphs by the dashed black line. Voltage (top) and voltage rate (bottom) graphs (black) display the output of the denoted sensing element. Results of five repeats of the same motion for each subject and each motion are available in Figs. S29-122. Axes titles and units as given in A) are the same for all like graphs. Strain maps and graphs include only triangles for which the correlation coefficient was lower than 0.4. The time axis for all subgraphs are the same.

Fig. S29-S122. Dropbox Link to Repeatability Figures (There are 64 Figures for Healthy Subjects and 30 Figures for ALS Subjects, for a total of 94 Figures):

https://www.dropbox.com/sh/rgkbu96wq2kzpk8/AACHDxswLCjPxUWW-k_G-AJya?dl=0

For each of these figures, the following caption applies:

Minimal (ϵ_1) and maximal (ϵ_2) principal spatiotemporal strain (%) maps (left two images) as well as their graphs at the location on the Tegaderm tape right on top of the sensing element (for cases with a cFaCES laminated on the face - S) or right underneath where the sensing element was placed on the facial skin (for cases without a cFaCES laminated on the face - NS) are depicted for each of trials (rows 1 - 5) repeated five times for each of sixteen motions performed by healthy subjects (n = 2) and ALS subjects (n = 1). For each five-second period, averaged strain across the DIC-generated triangles ($n \geq 9$) corresponding to the sensing element from which voltage is measured is represented as a solid line, and the shaded band indicates standard deviation. Note that the strain on the top layer of the sensor Tegaderm® tape is not exactly the same as that directly experienced by the piezoelectric layer, but the trend is expected to be the same . The peak strain is denoted in each of the strain graphs by the dashed black line. For cases with the sensor laminated on the face, the voltage graph (black) is also displayed. The scale bar for the strain maps is the same as in Fig. 3. Strain maps and graphs include only triangles for which the correlation coefficient was lower than 0.4. Strain maps and graphs include only triangles for which the correlation coefficient was lower than 0.4. The time scale for all graphs is the same.

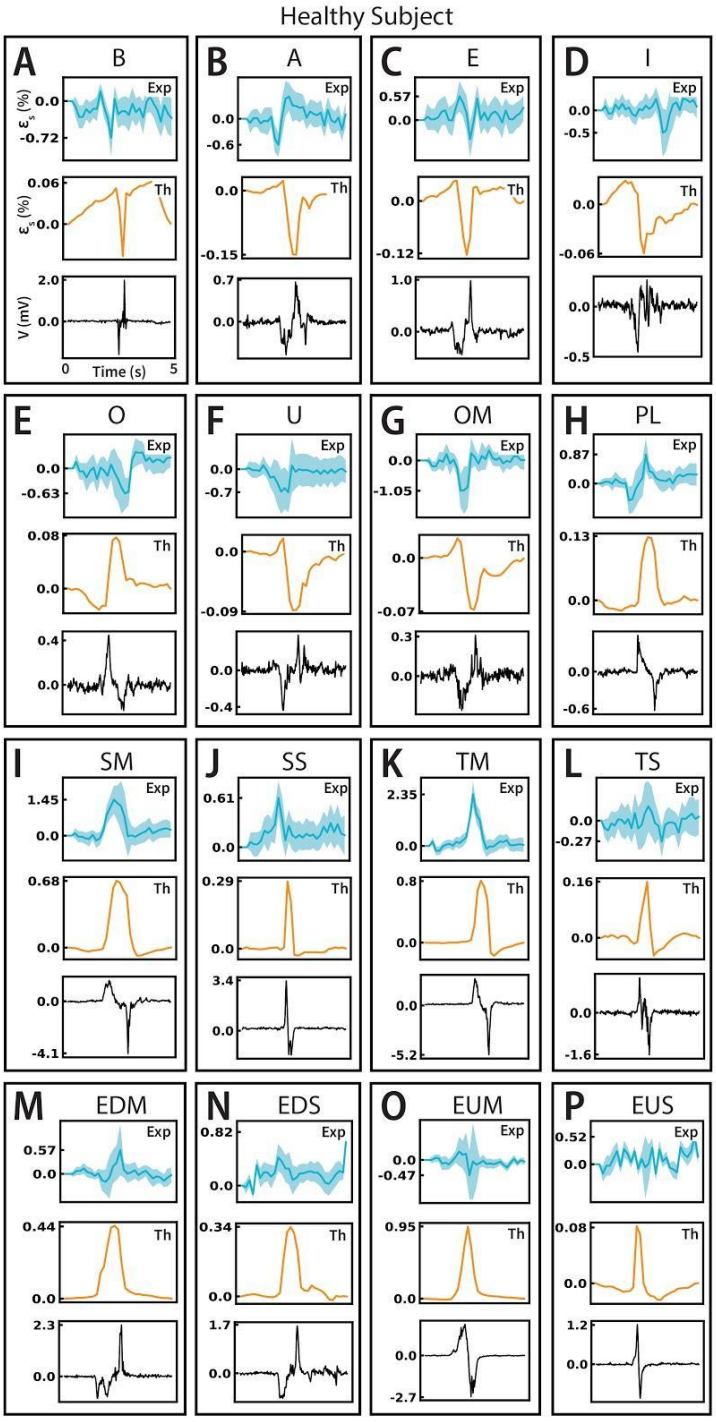

Fig. S123. Comparison of theoretical predictions and experimental measurements for sensor strain trace (ϵ_s) during facial deformations, healthy subject.

Theoretical calculations and experimental measurements suggest that cFaCES behavior is invariant between subjects, and can accurately capture strain experienced on the skin

regardless of subject. For each subfigure (A - P), the top graph (light blue) represents the experimental strain trace (%) on the top surface of the Tegaderm tape layer as measured by 3D-DIC, the middle graph (orange) represents the strain trace (%) as predicted by the theoretical model of cFaCES behavior *in vivo*, and the bottom graph (black) represents the voltage (mV) measured from one cFaCES element during the facial deformation. For each five-second period, averaged strain across the DIC-generated triangles ($n \geq 12$) band indicates standard deviation. Asynchronous timing of voltage and strain measurements may result in slight time offsets between experimental observations and theoretical predictions. Analyses for sixteen representative motions are shown (B = blink; EDM and EDS = eyebrow down medium magnitude and small magnitude, respectively; EUM and EUS = eyebrow up medium magnitude and small magnitude, respectively; A, E, I, O, U = saying vowel “A,” “E,” “I,” “O,” and “U,” respectively; OM = open mouth; PL = pursed lips, SM and SS = smile medium magnitude and small magnitude, respectively; TM and TS = twitch medium magnitude and small magnitude, respectively).

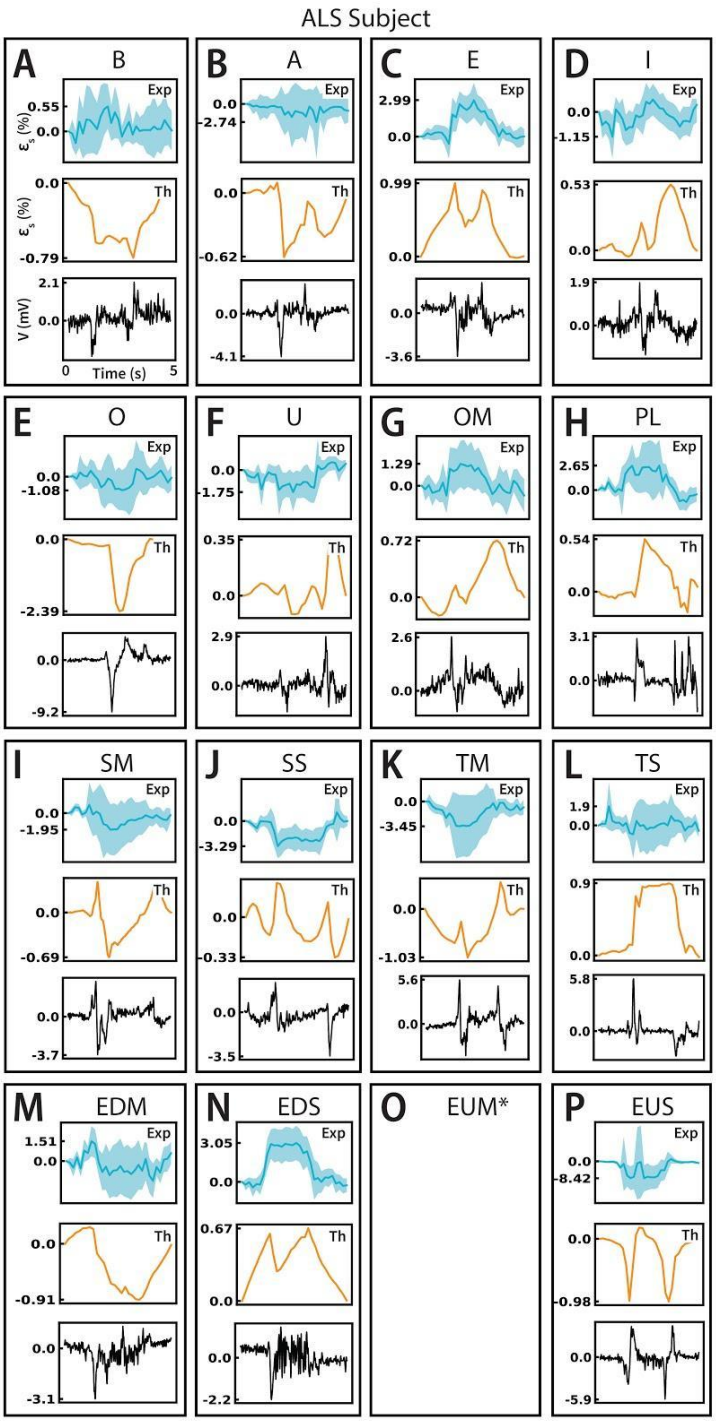

Fig. S124. Comparison of theoretical predictions and experimental measurements for sensor strain trace (ϵ_s) during facial deformations, ALS subject.

Theoretical calculations and experimental measurements suggest that cFaCES behavior is invariant between subjects, and can accurately capture strain experienced on the skin

regardless of subject. For each subfigure (A - P), the top graph (light blue) represents the experimental strain trace (%) on the top surface of the Tegaderm tape layer as measured by 3D-DIC, the middle graph (orange) represents the strain trace (%) as predicted by the theoretical model of cFaCES behavior *in vivo*, and the bottom graph (black) represents the voltage (mV) measured from one cFaCES element during the facial deformation. For each five-second period, averaged strain across the DIC-generated triangles ($n \geq 9$) corresponding to the sensing element from which voltage is measured is represented as a solid line, and the shaded band indicates standard deviation. Asynchronous timing of voltage and strain measurements may result in slight time offsets between experimental observations and theoretical predictions. Analyses for sixteen representative motions are shown (B = blink; EDM and EDS = eyebrow down medium magnitude and small magnitude, respectively; EUM and EUS = eyebrow up medium magnitude and small magnitude, respectively; A, E, I, O, U = saying vowel “A,” “E,” “I,” “O,” and “U,” respectively; OM = open mouth; PL = pursed lips, SM and SS = smile medium magnitude and small magnitude, respectively; TM and TS = twitch medium magnitude and small magnitude, respectively). *The subject could not perform the EUM motion.

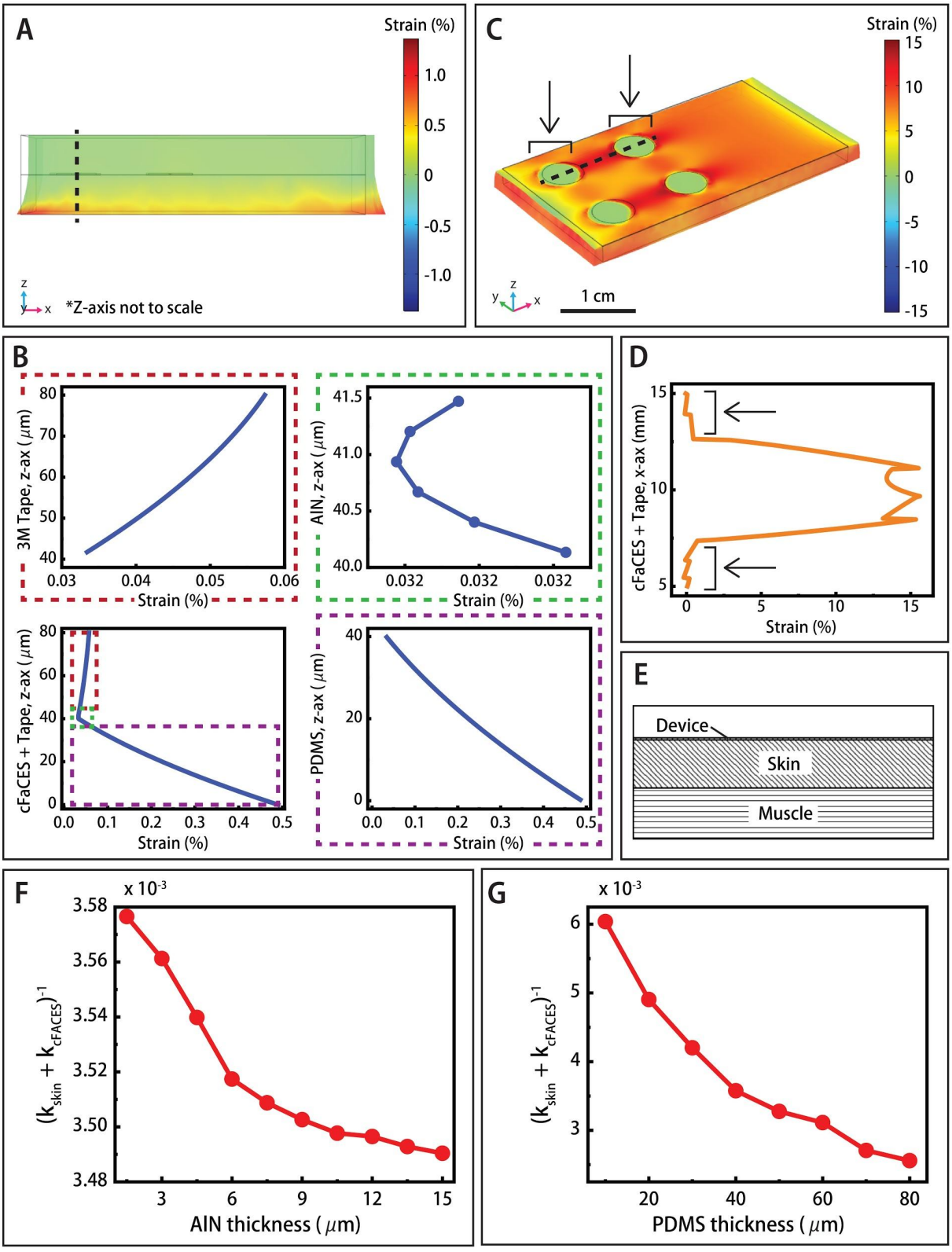

Fig. S125. Anisotropic mechanical response within cFaCES to external deformations.

FEM modeling of the cFaCES demonstrates the inherent anisotropy of the strain distribution in the composite sensor. A) FEM modeling of the cFaCES under 1% uniaxial strain (the strain is applied to the skin; here, the skin is directly underneath the cFaCES with and is not pictured) shows the variation of the strain along the thickness of the sensor (*Z-axis magnified 100x for clear visualization), showing the strain anisotropy in the substrate PDMS (bottom), AlN piezoelectric elements (middle), and 3M Tegaderm tape (top). B) Corresponding to the black dashed line in A), the respective values of the strain value along the thickness of the cFaCES (bottom left) and each respective layer - PDMS substrate (bottom right, violet dashed box), AlN piezoelectric element (top right, green dashed box [the strain differences in this layer are on the order of 10^{-8} %]), and 3M Tegaderm tape (top left, red dashed box) are shown. C) FEM modeling of the cFaCES under 10% uniaxial strain, showing variation of the strain along the X-axis lateral dimension on the top of the 3M Tegaderm tape. Unlike A), this strain map is to-scale, and depicts the thin cFaCES + 3M Tegaderm tape on top of a skin layer. D) Corresponding to the black dashed line in C), the strain value along the X-axis of the top of the 3M Tegaderm tape is displayed. Black arrows and brackets in C) and D) represent the locations directly above the piezoelectric element, which demonstrate less strain due to the high stiffness and elastic modulus of the underlying ceramic material. Between two piezoelectric elements in the direction of the strain, the strain on the top surface of the Tegaderm tape reaches a maximum value. E) A representative diagram of the cFaCES interaction with skin and muscle. Force generated in the muscle causes mechanical deformations in the skin and cFaCES. Theoretical modeling display how the compliance of the cFaCES-skin system ($(k_{skin} + k_{cFaCES})^{-1}$, where k_{skin} is the stiffness of the skin and k_{cFaCES} is the stiffness of the cFaCES) varies with F) the thickness of the AlN elements and G) the thickness of the PDMS substrate.

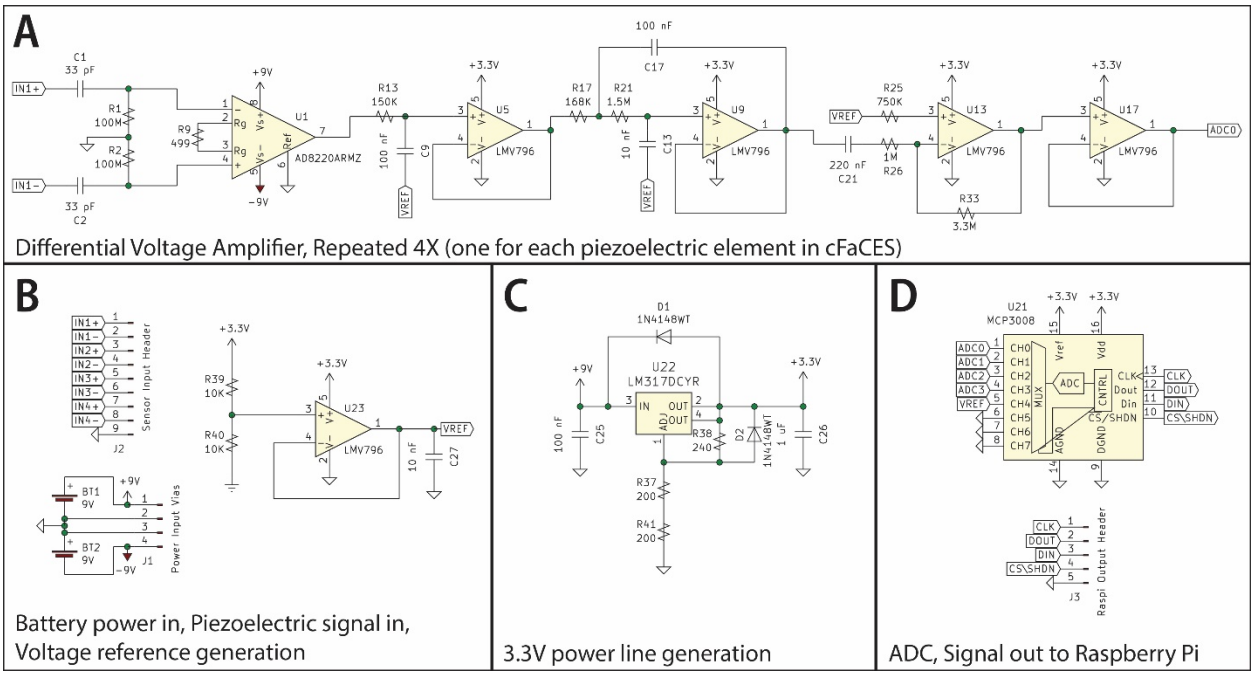

Fig. S126. Real Time Decoding Signal Processing Board circuit schematic

A) Circuit schematic for differential voltage amplifier for and second order active bandpass filter for signal extraction from cFaCES. This circuit is replicated four times to capture signals from all four elements of cFaCES simultaneously. B) Battery power (+9V and -9V) and signal inputs as well as voltage reference (1.65V) generation circuits. C) 3.3V power line generation from 9V battery power with voltage regulator circuit. D) Analog-to-digital converter (ADC) circuit and output to Raspberry Pi.

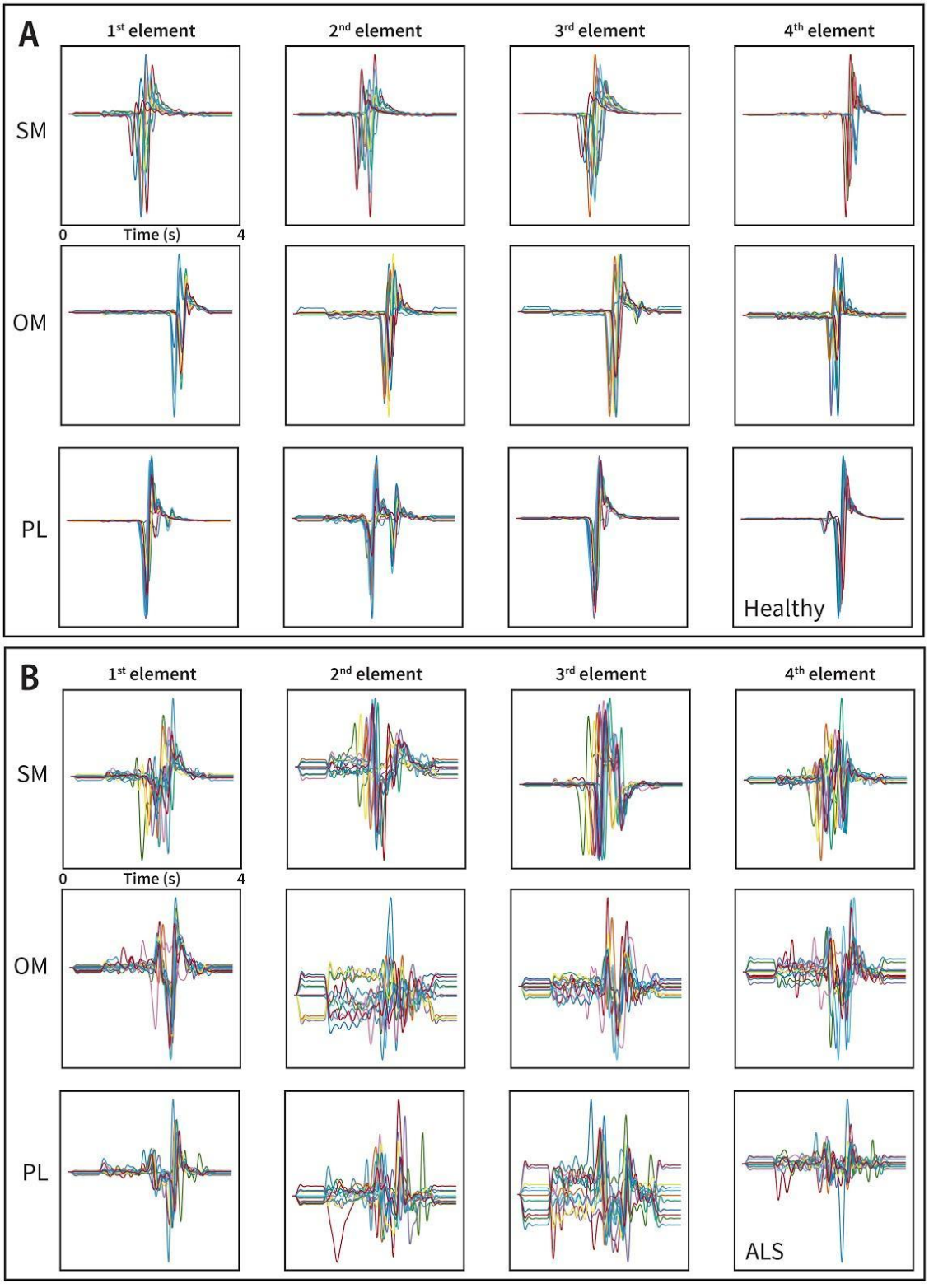

Fig. S127. Real Time Decoding 4-element sensor motions overlayed

Example of voltage waveforms (normalized) for facial motions smile medium (SM), open mouth (OM), and pursed lips (PL) recorded from the four elements of cFaCES simultaneously for A) healthy subject and B) ALS subject. The time scale is the same for all graphs. Each colored line represents one recorded motion. The KNN-DTW algorithm allows for classification even when the voltage waveforms for a given motion label are shifted in time or warped, i.e. motion is performed slower or faster.

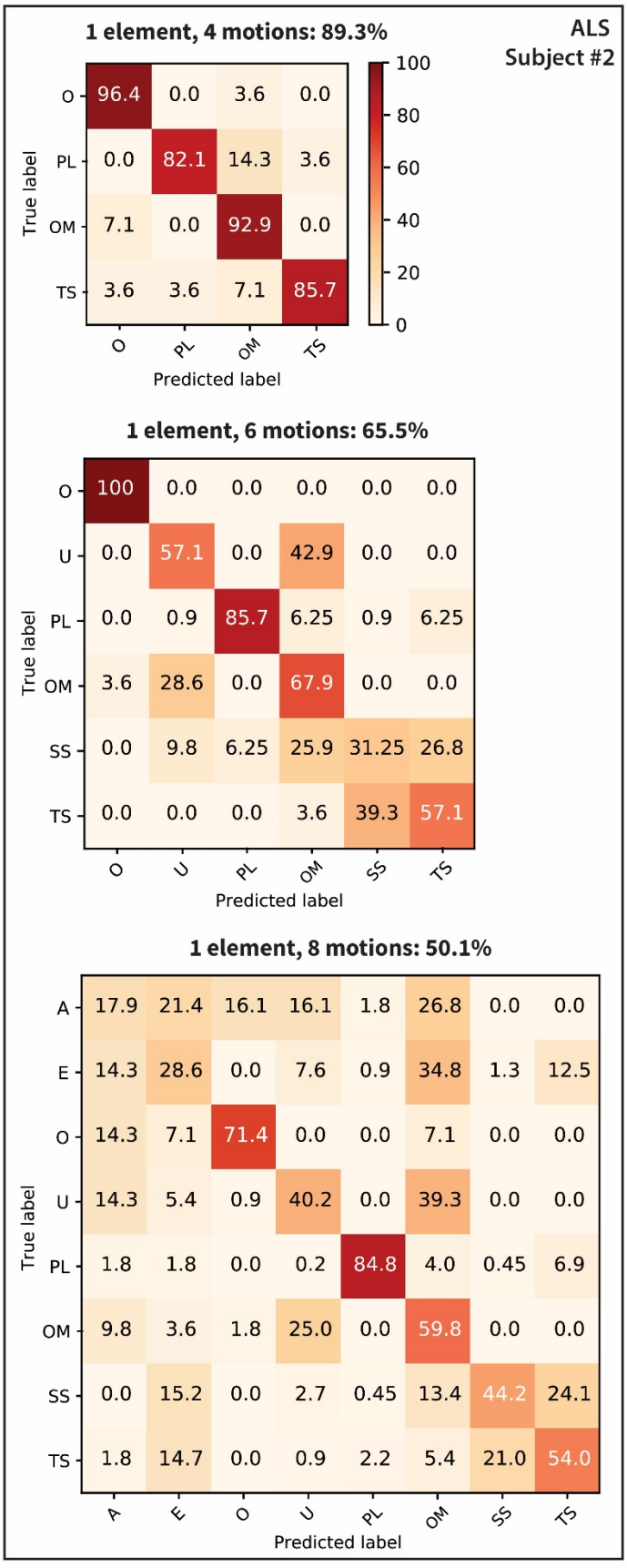

Figure S128. Post-recorded cFaCES single-element signals input into the KNN-DTW algorithm show viability for system use on a wider range of motions.

Confusion matrices show the accuracy of the KNN-DTW algorithm with input of post-recorded single-element cFaCES voltage signals from ALS subject #2 across a wider range of motions. The training set consisted of 7 distinct waveforms, of which 3 waveforms were randomly chosen for determination of testing accuracy in a stratified cross validation scheme. For four motions, the accuracy was 89.3% ± 18.5% (n = 16). For six motions, the accuracy was 65.5% ± 16.6% (n = 64). For eight motions, the accuracy was 50.1% ± 23.9% (n = 256). Random guessing would result in an accuracy of 25%, 16.7%, and 12.5% for each of the cases of four, six, and eight motions, respectively. The color refers to the percentage of motions with a given true label which were classified as a

given predicted label, and the scale bar for the top confusion matrix applies to all of the matrices. We should note that these results are not from real-time decoding, but rather uses the classification algorithm to determine accuracies on the various motions. Motions are as follows: vowel A (A), vowel E (E), vowel O (O), vowel U (U), pursed lips (PL), open mouth (OM), smile small (SS), and twitch small (TS).

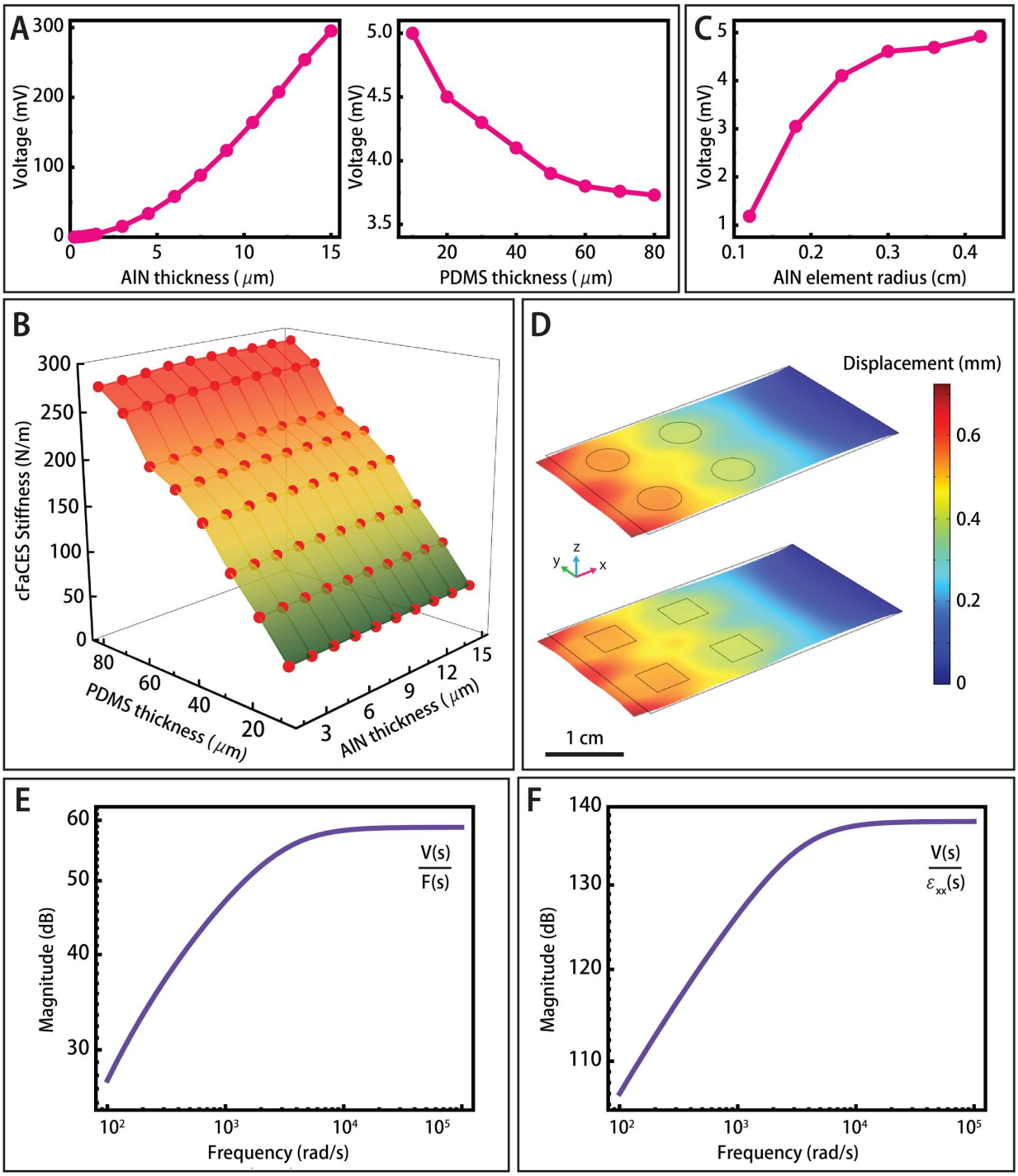

Fig. S129. Design considerations for the cFaCES.

Theoretical studies demonstrate the effect of thickness, size, and shape on the voltage sensitivity and stiffness of a cFaCES. Final values for these parameters in the fabricated cFaCES were chosen to balance the tradeoff between sensitivity and stiffness. A) Parametric

study via FEM modeling of the cFaCES under 1% uniaxial strain demonstrates that increasing the thickness of the piezoelectric AlN element significantly increases the voltage sensitivity of the sensor (left), whereas increasing the thickness of the substrate, PDMS, decreases the sensitivity of the sensor. Both effects are nonlinear. B) Increasing the thickness of the substrate PDMS layer or the AlN piezoelectric elements increases the stiffness of the cFaCES. C) Changing the size, parametrized by radius, of the piezoelectric element in cFaCES results in increased voltage sensitivity, but with diminishing returns. D) FEM modeling of the cFaCES under 0.1N uniaxial loading demonstrates that the displacement fields generated by cFaCES with square elements of same area as circular elements results in the same equivalent stiffness. Voltage sensitivity is necessarily the same for both shapes since the lateral area and thickness of the elements remained constant. Analytical modeling of a simplified cFaCES enables a E) voltage-force ($\frac{V(s)}{F(s)}$) transfer function and a F) voltage-strain ($\frac{V(s)}{\epsilon_{xx}(s)}$) transfer function.

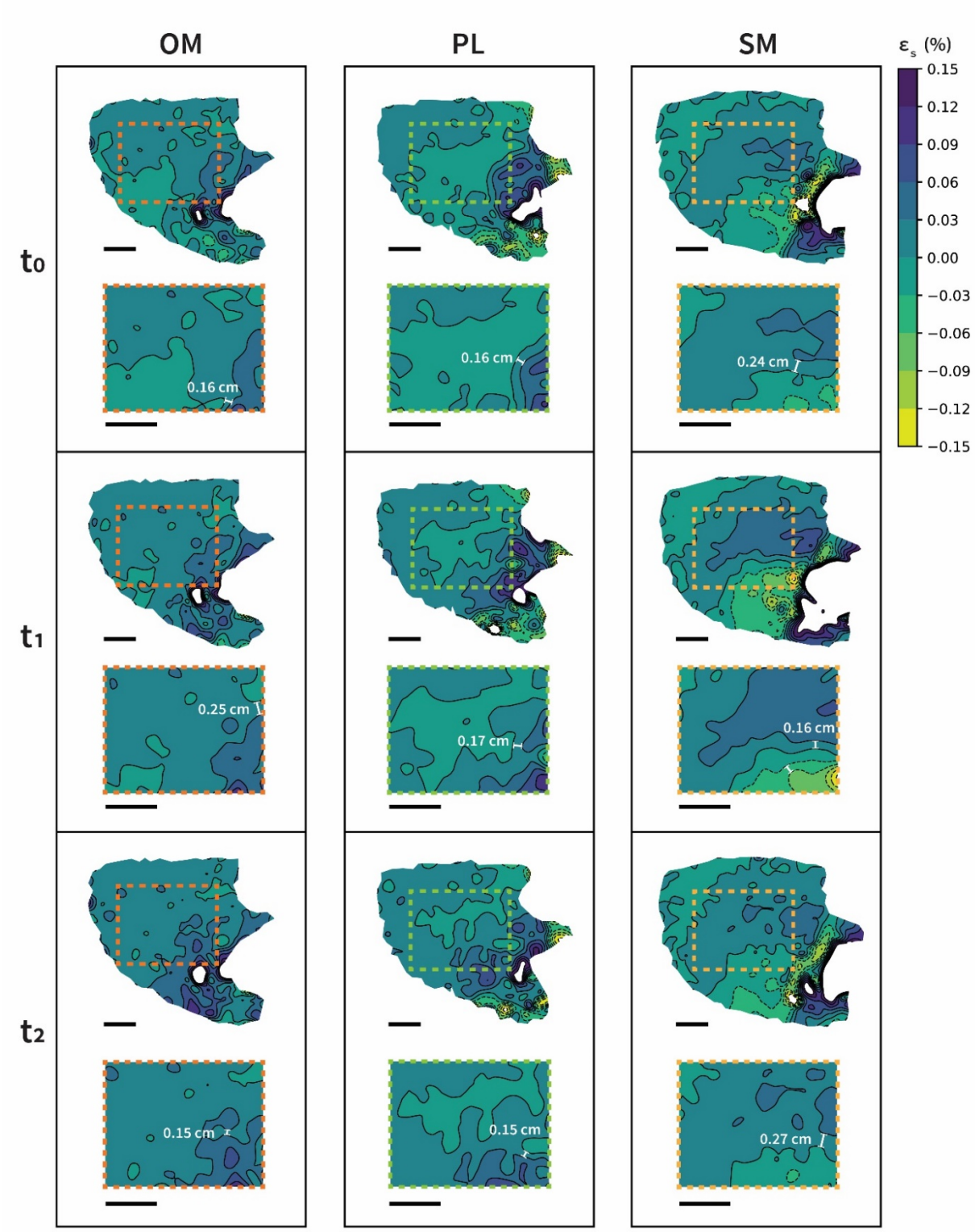

Figure S130. Strain gradation spacings for various motions from 3D-DIC contour maps.

Analysis of contour maps of measured ϵ_s of a healthy subject performing the motions open mouth (OM), pursed lips (PL), and smile medium (SM) can be used to determine the minimum spacings between successive isostrain lines, which can then be used as a guidance, along with considerations in Fig. S129c, for the choice of the size and spacing of the AlN piezoelectric elements in cFaCES. In this work, we have studied isostrain lines spaced apart by 3% strain gradations. For each motion and time point, the dashed box represents the region in which the sensor may be placed. This region's contour features are then analyzed spatially. For these gradations, analyzing the three motions over three different time points (t_0, t_1, t_2) shows that the minimum spacings (indicated by white lines) between strain isolines are between 0.15 cm and 0.27 cm. Scale bar on top right represents surface skin strain trace ϵ_s (%). All spatial scale bars (indicated by horizontal black lines) are 1 cm.

Appendix D: Captions for Supplementary Movies

Supplementary Movies can be found online at https://doi.org/10.1038/s41551-020-00612-w

Movie S1. Method to make cFaCES visually invisible with the facial skin

A cFaCES can be made visually invisible after lamination on the face. The facial skin and sensor are coated with silicone-based makeup primer. The facial skin is coated with a layer of foundation, and the sensor is painted using Silc Pig™ silicone pigment (Smooth-On, Macungie, PA, United States) (mixture of flesh tone, red, yellow, and white to match foundation tone).

Movie S2. 3D-DIC Setup and example of results of trial for motion OM without the sensor

Example of 3D-DIC experiment and results (represented by overlayed spatiotemporal maps of minimal principal strain ϵ_1 and maximal principal strain ϵ_2). This example is for an ALS subject performing the open mouth motion with no sensor laminated on the face.

Movie S3. 3D-DIC Setup and example of results of trial for motion PL without the sensor

Example of 3D-DIC experiment and results (represented by overlayed spatiotemporal maps of minimal principal strain ϵ_1 and maximal principal strain ϵ_2). This example is for an ALS subject performing the pursed lips motion with no sensor laminated on the face.

Movie S4. 3D-DIC Setup and example of results of trial for motion SM without the sensor

Example of 3D-DIC experiment and results (represented by overlayed spatiotemporal maps of minimal principal strain ϵ_1 and maximal principal strain ϵ_2). This example is for an ALS subject performing the smile medium magnitude motion with no sensor laminated on the face.

Movie S5. 3D-DIC Setup and example of results of trial for motion OM with the sensor

Example of 3D-DIC experiment and results (represented by overlayed spatiotemporal maps of minimal principal strain ϵ_1 and maximal principal strain ϵ_2). This example is for an ALS subject performing the open mouth motion with a cFaCES laminated on the face.

Movie S6. 3D-DIC Setup and example of results of trial for motion PL with the sensor

Example of 3D-DIC experiment and results (represented by overlayed spatiotemporal maps of minimal principal strain ϵ_1 and maximal principal strain ϵ_2). This example is for an ALS subject performing the open mouth motion with a cFaCES laminated on the face.

Movie S7. 3D-DIC Setup and example of results of trial for motion SM with the sensor

Example of 3D-DIC experiment and results (represented by overlayed spatiotemporal maps of minimal principal strain ϵ_1 and maximal principal strain ϵ_2). This example is for an ALS subject performing the smile medium magnitude motion with a cFaCES laminated on the face.

Movie S8. Real-Time Decoding setup, trials, and example of usage

Example of real time decoding experiment with an ALS subject, during which a KNN-DTW model is trained and tested (“calibrated”), and used in real-time for classification.

References

1. Asheber, W. T., Lin, C.-Y. & Yen, S. H. Humanoid Head Face Mechanism with Expandable Facial Expressions. *Int. J. Adv. Rob. Syst.* **13**, 29 (2016).

2. Blow, M., Dautenhahn, K., Appleby, A., Nehaniv, C. L. & Lee, D. The art of designing robot faces: Dimensions for human-robot interaction. in *HRI* vol. 6 331–332 (2006).

3. Yagi, M. Mathematical Modeling of Aging Effects in Adulthood on the Basis of Smiling Motions with Skin Mechanical Properties. in *2013 4th International Conference on Intelligent Systems, Modelling and Simulation* 182–185 (2013).

4. Shaw, P. J. Molecular and cellular pathways of neurodegeneration in motor neurone disease. *J. Neurol. Neurosurg. Psychiatry* **76**, 1046–1057 (2005).

5. GBD 2016 Motor Neuron Disease Collaborators. Global, regional, and national burden of motor neuron diseases 1990-2016: a systematic analysis for the Global Burden of Disease Study 2016. *Lancet Neurol.* **17**, 1083–1097 (2018).

6. Rong, P. *et al.* Predicting Speech Intelligibility Decline in Amyotrophic Lateral Sclerosis Based on the Deterioration of Individual Speech Subsystems. *PLoS One* **11**, e0154971 (2016).

7. Bandini, A. *et al.* Automatic Detection of Amyotrophic Lateral Sclerosis (ALS) from Video-Based Analysis of Facial Movements: Speech and Non-Speech Tasks. in *2018 13th IEEE International Conference on Automatic Face Gesture Recognition (FG 2018)* 150–157 (2018).

8. Kapur, A., Kapur, S. & Maes, P. AlterEgo: A Personalized Wearable Silent Speech Interface. in *23rd International Conference on Intelligent User Interfaces* 43–53 (ACM, 2018).

9. Shao, L. Facial Movements Recognition Using Multichannel EMG Signals. in *2019 IEEE Fourth International Conference on Data Science in Cyberspace (DSC)* 561–566 (2019).

10. Essa, I. A. & Pentland, A. P. Facial expression recognition using a dynamic model and motion energy. in *Proceedings of IEEE International Conference on Computer Vision* 360–367 (1995).

11. Essa, I., Basu, S., Darrell, T. & Pentland, A. Modeling, tracking and interactive animation of faces and heads//using input from video. in *Proceedings Computer Animation '96* 68–79 (1996).

12. La Cascia, M., Valenti, L. & Sclaroff, S. Fully automatic, real-time detection of facial gestures from generic video. in *IEEE 6th Workshop on Multimedia Signal Processing, 2004.* 175–178 (2004).

13. Wilson, A. J., Chin, B. C., Hsu, V. M., Mirzabeigi, M. N. & Percec, I. Digital Image Correlation: A Novel Dynamic Three-Dimensional Imaging Technique for Precise Quantification of the Dynamic Rhytid and Botulinum Toxin Type A Efficacy. *Plast. Reconstr. Surg.* **135**, 869e (2015).

14. Miura, N., Sakamoto, T., Aoyagi, Y. & Yoneyama, S. Visualizing surface strain distribution of facial skin using stereovision. *Theoretical and Applied Mechanics Letters* vol. 6 167–170 (2016).

15. Chen, Z. *et al.* Noninvasive, three-dimensional full-field body sensor for surface deformation monitoring of human body in vivo. *J. Biomed. Opt.* **22**, 1–10 (2017).

16. Dagnes, N. *et al.* Optimal marker set assessment for motion capture of 3D mimic facial movements. *J. Biomech.* **93**, 86–93 (2019).

17. de Lucena, J. O., Lima, J. P., Thomas, D. & Teichrieb, V. Real-Time Facial Motion Capture Using RGB-D Images Under Complex Motion and Occlusions. in *2019 21st Symposium on Virtual and Augmented Reality (SVR)* 120–129 (2019).

18. Dagdeviren, C. *et al.* Conformal piezoelectric systems for clinical and experimental characterization of soft tissue biomechanics. *Nat. Mater.* **14**, 728–736 (2015).

19. Yuan, J. *et al.* Computational models for the determination of depth-dependent mechanical properties of skin with a soft, flexible measurement device. *Proc. Math. Phys. Eng. Sci.* **472**, 20160225 (2016).

20. Feng, X. *et al.* Stretchable ferroelectric nanoribbons with wavy configurations on elastomeric substrates. *ACS Nano* **5**, 3326–3332 (2011).

21. Dong, G. *et al.* Super-elastic ferroelectric single-crystal membrane with continuous electric dipole rotation. *Science* **366**, 475–479 (2019).

22. Dagdeviren, C. *et al.* Transient, biocompatible electronics and energy harvesters based on ZnO. *Small* **9**, 3398–3404 (2013).

23. Persano, L. *et al.* High performance piezoelectric devices based on aligned arrays of nanofibers of poly(vinylidenefluoride-co-trifluoroethylene). *Nature Communications* vol. 4 (2013).

24. Persano, L. *et al.* Shear Piezoelectricity in Poly(vinylidenefluoride-co-trifluoroethylene): Full Piezotensor Coefficients by Molecular Modeling, Biaxial Transverse Response, and Use in Suspended Energy-Harvesting Nanostructures. *Advanced Materials* vol. 28 7633–7639 (2016).

25. Dagdeviren, C. *et al.* Recent progress in flexible and stretchable piezoelectric devices for mechanical energy harvesting, sensing and actuation. *Extreme Mechanics Letters* **9**, 269–281 (2016).

26. Dagdeviren, C., Li, Z. & Wang, Z. L. Energy Harvesting from the Animal/Human Body for Self-Powered Electronics. *Annu. Rev. Biomed. Eng.* **19**, 85–108 (2017).

27. Dagdeviren, C. *et al.* Conformal piezoelectric energy harvesting and storage from motions of the heart, lung, and diaphragm. *Proc. Natl. Acad. Sci. U. S. A.* **111**, 1927–1932 (2014).

28. Dagdeviren, C. *et al.* Flexible piezoelectric devices for gastrointestinal motility sensing. *Nat Biomed Eng* **1**, 807–817 (2017).

29. Niu, S. *et al.* A wireless body area sensor network based on stretchable passive tags. *Nature Electronics* **2**, 361–368 (2019).

30. Dagdeviren, C. *et al.* Conformable amplified lead zirconate titanate sensors with enhanced piezoelectric response for cutaneous pressure monitoring. *Nat. Commun.* **5**, 4496 (2014).

31. Yeo, W.-H. *et al.* Multifunctional epidermal electronics printed directly onto the skin. *Adv. Mater.* **25**, 2773–2778 (2013).

32. Akiyama, M. *et al.* Preparation of Oriented Aluminum Nitride Thin Films on Polyimide Films and Piezoelectric Response with High Thermal Stability and Flexibility. *Adv. Funct. Mater.* **17**, 458–462 (2007).

33. Fei, C. *et al.* AlN piezoelectric thin films for energy harvesting and acoustic devices. *Nano Energy* **51**, 146–161 (2018).

34. Doll, J. C., Petzold, B. C., Ninan, B., Mullapudi, R. & Pruitt, B. L. Aluminum nitride on titanium for CMOS compatible piezoelectric transducers. *J. Micromech. Microeng.* **20**, 025008 (2009).

35. Shelton, S. *et al.* CMOS-compatible AlN piezoelectric micromachined ultrasonic transducers. in *2009 IEEE International Ultrasonics Symposium* 402–405 (2009).

36. Rödel, J. *et al.* Transferring lead-free piezoelectric ceramics into application. *J. Eur. Ceram. Soc.* **35**, 1659–1681 (2015).

37. Priya, S. & Nahm, S. *Lead-Free Piezoelectrics*. (Springer Science & Business Media, 2011).

38. Wang, S. *et al.* Mechanics of Epidermal Electronics. *J. Appl. Mech.* **79**, (2012).

39. Kim, D.-H. *et al.* Epidermal electronics. *Science* **333**, 838–843 (2011).

40. Solav, D., Moerman, K. M., Jaeger, A. M., Genovese, K. & Herr, H. M. MultiDIC: An Open-Source Toolbox for Multi-View 3D Digital Image Correlation. *IEEE Access* **6**, 30520–30535 (2018).

41. Solav, D., Moerman, K. M., Jaeger, A. M. & Herr, H. A framework for measuring the time-varying shape and full-field deformation of residual limbs using 3D digital image correlation. *IEEE Trans. Biomed. Eng.* (2019) doi:10.1109/TBME.2019.2895283.

42. Blaber, J., Adair, B. & Antoniou, A. Ncorr: Open-Source 2D Digital Image Correlation Matlab Software. *Exp. Mech.* **55**, 1105–1122 (2015).

43. Pan, B., Qian, K., Xie, H. & Asundi, A. Two-dimensional digital image correlation for in-plane displacement and strain measurement: a review. *Meas. Sci. Technol.* **20**, 062001 (2009).

44. Solav, D., Rubin, M. B., Cereatti, A., Camomilla, V. & Wolf, A. Bone Pose Estimation in the Presence of Soft Tissue Artifact Using Triangular Cosserat Point Elements. *Ann. Biomed. Eng.* **44**, 1181–1190 (2016).

45. Solav, D. *et al.* Chest Wall Kinematics Using Triangular Cosserat Point Elements in Healthy and Neuromuscular Subjects. *Ann. Biomed. Eng.* **45**, 1963–1973 (2017).

46. Zhao, Y. *et al.* Investigation of mechanical behaviour of amorphous aluminium nitride. *Materialia* **2**, 148–156 (2018).

47. Ansari, M. & Amin Karami, M. Experimental study on nonlinear thermally buckled piezoelectric energy harvesters for leadless pacemakers. *Active and Passive Smart Structures and Integrated Systems XII* (2018) doi:10.1117/12.2300899.

48. Ansari, M. H. & Amin Karami, M. Energy harvesting from controlled buckling of piezoelectric beams. *Smart Materials and Structures* vol. 24 115005 (2015).

49. Ansari, M. H. & Amin Karami, M. Nonlinear Thermally Buckled Piezoelectric Energy Harvester. *Volume 6: 12th International Conference on Multibody Systems, Nonlinear Dynamics, and Control* (2016) doi:10.1115/detc2016-60476.

50. Karami, M. A., Inman, D. J. & Ansari, M. H. Energy harvesting from constrained buckling of piezoelectric beams. *US Patent* (2019).

51. Ansari, M. H. & Karami, M. A. Energy Harvesting From Controlled Buckling of a Horizontal Piezoelectric Beam. in *ASME 2014 International Design Engineering Technical Conferences and Computers and Information in Engineering Conference* (American Society of Mechanical Engineers Digital Collection, 2015). doi:10.1115/DETC2014-35217.

52. Karami, M. A. & Inman, D. J. Controlled Buckling of Piezoelectric Beams for Direct Energy Harvesting From Passing Vehicles. in *ASME 2012 International Design Engineering Technical Conferences and Computers and Information in Engineering Conference* 1231–1236 (American Society of Mechanical Engineers Digital Collection, 2013).

53. Abou-Rayan, A. M., Nayfeh, A. H., Mook, D. T. & Nayfeh, M. A. Nonlinear response of a parametrically excited buckled beam. *Nonlinear Dyn.* (1993).

54. Erturk, A. & Inman, D. J. An experimentally validated bimorph cantilever model for piezoelectric energy harvesting from base excitations. *Smart Mater. Struct.* **18**, 025009 (2009).

55. Karami, M. A. & Inman, D. J. Equivalent damping and frequency change for linear and nonlinear hybrid vibrational energy harvesting systems. *J. Sound Vib.* **330**, 5583–5597 (2011).

56. Nayfeh, A. H. & Frank Pai, P. Linear and Nonlinear Structural Mechanics. (2004) doi:10.1002/9783527617562.

57. Virgin, L. N. Vibration of Axially Loaded Structures. (2007) doi:10.1017/cbo9780511619236.

58. Sirohi, J. & Chopra, I. Fundamental understanding of piezoelectric strain sensors. *Smart Structures and Materials 1999: Smart Structures and Integrated Systems* (1999) doi:10.1117/12.350731.

59. Varatharajan, R., Manogaran, G., Priyan, M. K. & Sundarasekar, R. Wearable sensor devices for early detection of Alzheimer disease using dynamic time warping algorithm. *Cluster Comput.* **21**, 681–690 (2018).

60. Zhang, Z. *et al.* Dynamic Time Warping under limited warping path length. *Inf. Sci.* **393**, 91–107 (2017).

61. Wan, Y., Chen, X.-L. & Shi, Y. Adaptive cost dynamic time warping distance in time series analysis for classification. *J. Comput. Appl. Math.* **319**, 514–520 (2017).

62. Salvador, S. & Chan, P. FastDTW: Toward Accurate Dynamic Time Warping in Linear Time and Space. 3rd Wkshp. on Mining Temporal and Sequential Data. *ACM KDD '04* (2004).

63. Aristidou, A., Cohen-Or, D. & Hodgins, J. K. Self-similarity Analysis for Motion Capture Cleaning. *Comput. Graph.* (2018).

64. Zhao, W. *et al.* Real-Time Vehicle Motion Detection and Motion Altering for Connected Vehicle: Algorithm Design and Practical Applications. *Sensors* **19**, (2019).

65. Tait, R. N. & Mirfazli, A. Low temperature aluminum nitride deposition on aluminum by rf reactive sputtering. *J. Vac. Sci. Technol. A* **19**, 1586–1590 (2001).

66. Iqbal, A. & Mohd-Yasin, F. Reactive Sputtering of Aluminum Nitride (002) Thin Films for Piezoelectric Applications: A Review. *Sensors* **18**, (2018).

67. Zhang, Q. M. & Zhao, J. Electromechanical properties of lead zirconate titanate piezoceramics under the influence of mechanical stresses. *IEEE Trans. Ultrason. Ferroelectr. Freq. Control* **46**, 1518–1526 (1999).

68. Jiang, X. *et al.* Monolithic ultrasound fingerprint sensor. *Microsyst Nanoeng* **3**, 17059 (2017).

69. Tadigadapa, S. & Mateti, K. Piezoelectric MEMS sensors: state-of-the-art and perspectives. *Meas. Sci. Technol.* **20**, 092001 (2009).

70. Ruby, R. The 'how & why' a deceptively simple acoustic resonator became the basis of a multi-billion dollar industry. *2017 IEEE 30th International Conference on Micro Electro Mechanical Systems (MEMS)* (2017) doi:10.1109/memsys.2017.7863403.

71. Chen, G. & Rinaldi, M. Aluminum Nitride Combined Overtone Resonators for the 5G High Frequency Bands. *J. Microelectromech. Syst.* 1–12 (2020).

72. Petroni, S. *et al.* Tactile multisensing on flexible aluminum nitride. *Analyst* **137**, 5260–5264 (2012).

73. Petroni, S. *et al.* Aluminum Nitride piezo-MEMS on polyimide flexible substrates. *Microelectron. Eng.* **88**, 2372–2375 (2011).

74. Akiyama, M. *et al.* Flexible piezoelectric pressure sensors using oriented aluminum nitride thin films prepared on polyethylene terephthalate films. *J. Appl. Phys.* **100**, 114318 (2006).

75. Jackson, N., Keeney, L. & Mathewson, A. Flexible-CMOS and biocompatible piezoelectric AlN material for MEMS applications. *Smart Mater. Struct.* **22**, 115033 (2013).

76. Li, Q. *et al.* Growth and Characterization of Polyimide-Supported AlN Films for Flexible Surface Acoustic Wave Devices. *Journal of Electronic Materials* vol. 45 2702–2709 (2016).

77. Bi, X., Wu, Y., Wu, J., Li, H. & Zhou, L. A model for longitudinal piezoelectric coefficient measurement of the aluminum nitride thin films. *J. Mater. Sci.: Mater. Electron.* **25**, 2435–2442 (2014).

78. Yang, J. *et al.* Growth of AlN films as a function of temperature on Mo films deposited by different techniques. *J. Electron. Mater.* **43**, 369–374 (2014).

79. Lu, Y. *et al.* Surface Morphology and Microstructure of Pulsed DC Magnetron Sputtered Piezoelectric AlN and AlScN Thin Films. *Phys. Status Solidi* **215**, 1700559 (2018).

80. Martin, F., Muralt, P., Dubois, M.-A. & Pezous, A. Thickness dependence of the properties of highly c-axis textured AlN thin films. *J. Vac. Sci. Technol. A* **22**, 361–365 (2004).

81. Miyanaga, M. *et al.* Evaluation of AlN single-crystal grown by sublimation method. *J. Cryst. Growth* **300**, 45–49 (2007).

82. Sanz-Hervás, A. *et al.* Comparative study of c-axis AlN films sputtered on metallic surfaces. *Diam. Relat. Mater.* **14**, 1198–1202 (2005).

83. Yarar, E. *et al.* Low temperature aluminum nitride thin films for sensory applications. *AIP Adv.* **6**, 075115 (2016).

84. Singh, A. V., Chandra, S. & Bose, G. Deposition and characterization of c-axis oriented aluminum nitride films by radio frequency magnetron sputtering without external substrate heating. *Thin Solid Films* **519**, 5846–5853 (2011).

85. Tay, K.-W., Huang, C.-L., Wu, L. & Lin, M.-S. Performance Characterization of Thin AlN Films deposited on Mo Electrode for Thin-Film Bulk Acoustic-Wave Resonators. *Jpn. J. Appl. Phys.* **43**, 5510 (2004).

86. Schnable, G. L. & Keen, R. S. Aluminum metallization—Advantages and limitations for integrated circuit applications. *Proc. IEEE* **57**, 1570–1580 (1969).

87. Obuh, I. E. *et al.* Low-Cost Microfabrication for MEMS Switches and Varactors. *IEEE Trans. Compon. Packaging Manuf. Technol.* **8**, 1702–1710 (2018).

88. Baeg, K.-J., Bae, G.-T. & Noh, Y.-Y. Efficient charge injection in p-type polymer field-effect transistors with low-cost molybdenum electrodes through V2O5 interlayer. *ACS Appl. Mater. Interfaces* **5**, 5804–5810 (2013).

89. Rogers, J. A., Someya, T. & Huang, Y. Materials and mechanics for stretchable electronics. *Science* **327**, 1603–1607 (2010).

90. Artieda, A., Barbieri, M., Sandu, C. S. & Muralt, P. Effect of substrate roughness on c-oriented AlN thin films. *J. Appl. Phys.* **105**, 024504 (2009).

91. Luboz, V., Promayon, E. & Payan, Y. Linear elastic properties of the facial soft tissues using an aspiration device: towards patient specific characterization. *Ann. Biomed. Eng.* **42**, 2369–2378 (2014).

92. Kim, Y.-S. *et al.* Regional thickness of facial skin and superficial fat: Application to the minimally invasive procedures. *Clin. Anat.* **32**, 1008–1018 (2019).

93. Leo, D. J. *Engineering Analysis of Smart Material Systems*. (John Wiley & Sons, 2007).

94. Goodno, B. J. & Gere, J. M. *Mechanics of Materials, SI Edition*. (Cengage Learning, 2017).

95. Popov, E. P. & Balan, T. A. *Engineering mechanics of solids, 2nd ed*. (Upper Saddle River, NJ: Prentice Hall. xvi, 1999).

96. Bauchau, O. A. & Craig, J. I. *Structural Analysis: With Applications to Aerospace Structures*. (Springer Science & Business Media, 2009).

97. Rao, S. S. *Vibration of Continuous Systems*. (John Wiley & Sons, Inc., 2019).

98. Lepi, S. *Practical Guide to Finite Elements: A Solid Mechanics Approach*. (CRC Press, 1998).

99. Inman, D. J. *Engineering Vibration*. (Prentice Hall, 2001).

100. Vibration of Circular Rings and Curved Beams. in *Vibration of Continuous Systems* (ed. Rao, S. S.) 393–419 (John Wiley & Sons, Inc., 2006).

101. Baker, S. & Matthews, I. Lucas-Kanade 20 Years On: A Unifying Framework. *Int. J. Comput. Vis.* **56**, 221–255 (2004).

102. Pan, B. Reliability-guided digital image correlation for image deformation measurement. *Appl. Opt.* **48**, 1535–1542 (2009).

103. Tsagkrasoulis, D., Hysi, P., Spector, T. & Montana, G. Heritability maps of human face morphology through large-scale automated three-dimensional phenotyping. *Sci. Rep.* **7**, 45885 (2017).

104. Du, S. *et al.* A new electrode design method in piezoelectric vibration energy harvesters to maximize output power. *Sens. Actuators A Phys.* **263**, 693–701 (2017).

105. Erturk, A. & Inman, D. J. Piezoelectric Energy Harvesting. (2011) doi:10.1002/9781119991151.

106. Nayfeh, A. H. & Balachandran, B. *Applied Nonlinear Dynamics: Analytical, Computational, and Experimental Methods*. (John Wiley & Sons, 2008).

107. Karami, M. A., Varoto, P. S. & Inman, D. J. Experimental Study of the Nonlinear Hybrid Energy Harvesting System. in *Modal Analysis Topics, Volume 3* 461–478 (Springer New York, 2011).

108. Strogatz, S. H. *Nonlinear dynamics and chaos: with applications to physics, biology, chemistry, and engineering*. (CRC Press, 2018).

109. Koydemir, H. C. & Ozcan, A. Wearable and Implantable Sensors for Biomedical Applications. *Annu. Rev. Anal. Chem.* **11**, 127–146 (2018).

110. Coletta, N. A., Mallette, M. M., Gabriel, D. A., Tyler, C. J. & Cheung, S. S. Core and skin temperature influences on the surface electromyographic responses to an isometric force and position task. *PLoS One* **13**, e0195219 (2018).